ACOUSTIC RESONANCE IN A HIGH-SPEED AXIAL COMPRESSOR

Der Fakultät für Maschinenbau
der Gottfried Wilhelm Leibniz Universität Hannover
zur Erlangung des akademischen Grades

Doktor-Ingenieur

genehmigte Dissertation
von

Dipl.-Phys. Bernd Hellmich

geboren am 23.11.1970 in Rahden/Westfalen, Deutschland

2008

Referent:	Prof. Dr.-Ing. Jörg Seume
Korreferent:	Prof. Dr.-Ing. Wolfgang Neise
Vorsitzender:	Prof. Dr.-Ing. Peter Nyhuis
Tag der Promotion:	12.11.2007

„Das Chaos ist aufgebraucht, es war die beste Zeit“
B. Brecht

Für Bettina

1. Abstract

Non-harmonic acoustic resonance was detected in the static pressure and sound signals in a four-stage high-speed axial compressor when the compressor was operating close to the surge limit. The amplitudes of the resonant acoustic mode are in a range comparable to the normally dominating blade passing frequency. This has led to blade cracks in the inlet guided vanes of the compressor where the normal mechanical and aerodynamic load is low.

The present measurements were obtained with a dynamic four-hole pneumatic probe and an array of dynamic pressure transducers in the compressor casing. For signal decomposition and analysis of signal components with high signal-to-noise ratio, estimator functions such as Auto Power Spectral Density and Cross Power Spectral Density were used.

Based on measurements of the resonance frequency and the axial and circumferential phase shift of the pressure signal during resonance, it is shown that the acoustic resonance is an axial standing wave of a spinning acoustic mode with three periods around the circumference of the compressor. This phenomenon occurs only if the aerodynamic load in the compressor is high, because the mode needs a relative low axial Mach number at a high rotor speed for resonance conditions. The low Mach number is needed to fit the axial wave length of the acoustic mode to the axial spacing of the rotors in the compressor. The high rotor speed is needed to satisfy the reflection conditions at the rotor blades needed for the acoustic resonance.

The present work provides suitable, physically based simplifications of the existing mathematical models which are applicable for modes with circumferential wavelengths of more than two blade pitches and resonance frequencies considerably higher than the rotor speed. The reflection and transmission of the acoustic waves at the blade rows is treated with a qualitative model. Reflection and transmission coefficients are calculated for certain angles of attack only, but qualitative results are shown for the modes of interest. Behind the rotor rows the transmission is high while in front of the rotor rows the reflection is dominating. Because the modes are trapped in each stage of the compressor by the rotor rows acoustic resonance like this could appear in multi stage axial machines only.

Different actions taken on the compressor to shift the stability limit to lower mass flow like dihedral blades and air injection at the rotor tips did not succeed. Hence, it is assumed that the acoustic resonance is dominating the inception of rotating stall at high rotor speeds. A modal wave as rotating stall pre cursor was detected with a frequency related to the acoustic resonance frequency. In addition the acoustic resonance is modulated in amplitude by this modal wave. The acoustic waves are propagating nearly perpendicular to the mean flow, so that they are causing temporally an extra incidence of the mean flow on the highly loaded blades, but it could not be proved if this triggers the stall. A positive effect of the acoustic resonance on the stability limit due to the stabilization of the boundary layers on the blades by the acoustic field is also not excluded.

Keywords: acoustic resonance, axial compressor, rotating stall

Kurzfassung

Nicht drehzahlharmonische akustische Resonanzen sind in den statischen Drucksignalen in einem vierstufigen Hochgeschwindigkeitsaxialverdichter gemessen worden, als dieser nahe der Pumpgrenze betrieben worden ist. Die Amplituden der resonanten Moden lagen in derselben Größenordnung wie die Schaufelpassierfrequenz. Das führte zu Rissen in den Schaufeln im Vorleitapparat des Kompressors, wo die normale mechanisch und aerodynamisch Belastung niedrig ist.
Die vorliegenden Messungen sind mit einer dynamischen Vierloch-Sonde und einem Feld von dynamischen Drucksensoren im Kompressorgehäuse durchgeführt worden. Zur Signalzerlegung und Analyse mit hohem Signal zu Rauschverhältnis sind Schätzfunktionen wie Autospektrale Leistungsdichte und Kreuzspektrale Leistungsdichte verwendet worden.
Aufgrund von Messungen der Resonanzfrequenz sowie des axialen und peripheren Phasenversatzes der Drucksignale unter resonanten Bedingungen ist gezeigt worden, dass die akustische Resonanz in axialer Richtung eine stehende Welle ist mit drei Perioden um den Umfang. Das Phänomen tritt nur auf, wenn die aerodynamische Belastung des Kompressors hoch ist, da die Resonanzbedingungen für die Mode eine niedrige axiale Machzahl bei hoher Rotordrehzahl erfordern. Die relativ niedrige axiale Machzahl ist nötig, damit die axiale Wellenlänge zum axialen Abstand der Rotoren passt. Die hohe Drehzahl ist notwendig, um die Reflektionsbedingungen an den Rotorschaufeln zu erfüllen.
Die vorliegende Arbeit verwendet physikalisch basierte Vereinfachungen von existierenden Modellen, die anwendbar sind auf Moden mit einer Wellenlänge in Umfangsrichtung, die größer als zwei Schaufelteilungen sind und eine Resonanzfrequenz haben, die über der Rotordrehzahl liegt. Die Reflektion und Transmission von akustischen Wellen ist mit einem qualitativen Modell behandelt worden. Die Reflektions- und Transmissionskoeffizienten sind nur für bestimmte Einfallswinkel berechnet worden, aber die Ergebnisse zeigen, dass für die relevanten Moden die Transmission hinter den Rotoren hoch ist während vor den Rotoren die Reflexion dominiert. Weil die Moden zwischen den Rotoren eingeschlossen sind, können akustische Resonanzen wie diese nur in mehrstufigen Axialmaschinen auftreten.
Verschiedene Maßnahmen, die an dem Kompressor durchgeführt worden sind, wie dreidimensionale Schaufelgeometrien oder Einblasung an den Rotorspitzen, haben zu keiner Verschiebung der Stabilitätsgrenze zu niedrigeren Massenströmen geführt. Deshalb wird angenommen, dass die akustische Resonanz die Entstehung einer rotierenden Ablösung (Rotating Stall) herbeiführt. Eine Modalwelle als Vorzeichen für den Rotating Stall ist gemessen worden, dessen Frequenz ein ganzzahliger Bruchteil der Frequenz der akustischen Resonanz ist. Außerdem ist die Amplitude der akustischen Resonanz von der Modalwelle moduliert. Die akustischen Wellen laufen nahezu senkrecht zur Strömungsrichtung, so dass sie kurzzeitig eine zusätzliche Fehlanströmung der hoch belasteten Schaufeln verursachen, aber es konnte nicht bewiesen werden, dass dies die Ablösung auslöst. Ein positiver Einfluss der akustischen Resonanz auf die Stabilität des Verdichters durch die Stabilisierung der Grenzschichten auf den Verdichterschaufeln ist ebenso nicht ausgeschlossen.

Schlagwörter: Akustische Resonanz, Axialverdichter, Rotierende Ablösung

2. Contents

1. Abstract V
2. Contents VII
3. Nomenclature IX
4. Introduction 1
4.1. Compressors 1
4.2. Flow distortions in compressors 3
5. Literature Review 5
6. Test facility 8
6.1. The test rig 8
6.2. Sensors, Signal Conditioning and Data Acquisition 10
7. Signal processing methods 12
7.1. Auto Power Spectral Density (APSD) 12
7.2. APSD estimation by periodogram averaging method 13
7.3. Cross power spectral density (CPSD), phase, and coherence 15
7.4. Coherent transfer functions 17
7.5. Statistical Errors of coherence, power and phase spectra 18
7.6. Spectral leakage 20
8. The Phenomenon 24
8.1. Acoustic resonance versus multi-cell rotating stall 27
8.2. Helmholtz resonance at outlet throttle 28
8.3. Vibration induced blade cracks 30
9. Theoretical Prediction of resonant modes 33
9.1. Effect of blade rows 33
9.2. Effect of non-uniform flow and geometry 37
9.3. Summary of theoretical prediction methods 38
9.4. Simplified model 38

10. Application to Measurements 45
10.1. Measured pressure magnitude and phase shifts 48
10.2. Measured radial pressure distribution of AR 48
10.3. Application of model to flow measurements 52
10.4. Reflection and transmission of acoustic waves through blade rows 58
10.5. Transient flow measurements at constant rotor speed 62
10.5.1. Frequency shift and mean flow parameters 63
10.5.2. Axial phase shift and mean flow parameters 64
10.6. Acoustic resonance and rotor speed 67
10.7. Summary and conclusions of data analysis 71
11. Rotating Stall inception 72
11.1. Compressor stability 72
11.2. Fundamentals of rotating stall 73
11.3. Stall inception in the TFD compressor 77
11.3.1. Diffusion coefficient 77
11.3.2. Axial detection of the rotating stall origin 78
11.3.3. Radial detection of the rotating stall origin 82
11.3.4. Circumferential detection of the rotating stall origin 83
11.3.5. Stall inception at different rotor speeds 84
11.4. Frequency analysis of rotating stall measurements 85
11.4.1. Magnitudes at different rotor speeds 85
11.4.2. Phase and Coherence at different rotor speeds 86
11.5. Summary of rotating stall inception 91
11.6. Interaction of acoustic resonance and rotating stall 91
11.6.1. Time series analysis of measurements 93
11.6.2. Modulation of acoustic resonance 94
11.6.3. Magnitude and incidence angle of acoustic waves prior stall 95
11.7. Conclusions of acoustic resonance and rotating stall interaction 97
12. Summary and Conclusions 98
13. Outlook 100
14. Acknowledgement 103
15. References 104

3. Nomenclature

Symbol	Units	Meaning	Defined in
Latin			
a	m/s	speed of sound	
c	m/s	mean flow velocity	
c_u / c_a	m/s	swirl / axial velocity of mean flow	
d	m	diameter of the compressor annulus	
D	m	tip clearance, damping factor	Eq. (54) Section 10.3
DC		diffusion coefficient	Eq. (64) Section 11.3.1
f	Hz	absolute frequency	
f_{shaft}	Hz	shaft speed	
k	1/m	wave number	Eq. (41) Section 9.4
l	m	chord length	
Ma		Mach number of the mean flow	
Ma_φ /Ma_z		circumferential / axial Mach number of the mean flow	
$\dot{m}_{corr}$	kg/s	normalized mass flow	
m		circumferential mode number	
n	Hz	physical rotor speed, radial mode number	
n_{norm}	Hz	normalized rotor speed	
p	Pa	pressure	
r	m	radius	
s	m	blade pitch	
t	s	time	
z	m	axial co-ordinate	
h		Index of the harmonic order	
Greek			
α	°	flow angle	Eq. (48) Section 9.4
α_s	°	stagger angle of the blade row	
α_m	°	blade inlet/exit angle	
$\beta_\pm$	°	incidence angle of wave in present model, slope angle of helical wave fronts	Eq. (45) Section 9.4
λ	m	wave length	
θ_I	°	incidence angle of wave in Koch's model	Fig. 17
θ_R	°	reflection angle of wave in Koch's model	Fig. 17
θ_T	°	transmission angle of wave in Koch's model	Fig. 17
π		total pressure ratio	
σ		hub ratio (r_i/ r_o)	
φ	°	azimuthal coordinate	
ω	2π/s	angular frequency	
δ	°	circumferential distance of sensor x and y	
θ_{xy}	°	value of the phase function	Eq. (16) and (22) Section 7.3
γ^2		value of the coherence function	Eq. (15) Section 7.3

4. Introduction

4.1. Compressors

> *"My invention consists in a compressor or pump of the turbine type operating by the motion of sets of movable blades or vanes between sets of fixed blades, the movable blades being more widely spaced than in my steam turbine, and constructed with curved surfaces on the delivery side, and set at a suitable angle to the axis of rotation. The fixed blades may have a similar configuration and be similarly arranged on the containing casing at any suitable angle. "*Parsons 1901, taken from Horlock (1958)

In 1853 the basic fundamentals of the operations of a multistage axial compressor were first presented to the French Academy of Sciences. Parsons built and patented the first axial flow compressor in 1901 (Horlock (1958)). Since then, compressors have significantly evolved. For example, continuous improvements have enabled increases in efficiency, the pressure ratio per stage, and a decrease in weight. Compressors have a wide variety of applications. They are a primary component in turbojet engines used in aerospace propulsion, in industrial gas turbines that generate power, and in processors in the chemical industry to pressurize gas or fluids. The size ranges from a few centimetres in turbochargers to several meters in diameter in heavy-duty industrial gas turbines. In turbomachinery applications, safe and efficient operation of the compression system is imperative. To ensure this and to prevent damage, flow instabilities must be avoided or dealt with soon after their inception. Considerable interest exists in the jet propulsion community in understanding and controlling flow instabilities. Especially turbojet engines in military aircraft and gas turbines in power plants during instabilities of the electric grid must be able to handle abrupt changes in operating conditions. Hence, the treatment of flow instabilities in axial flow compressors is of special interest in military applications and power generation.

1.1 AN OVERVIEW OF COMPRESSOR OPERATIONS

The basic purpose of a compressor is to increase the total pressure of the working fluid using shaft work. Depending on their type, compressors increase the pressure in different ways. They can be divided into four general groups: rotary, reciprocating, centrifugal and axial. In reciprocating compressors, shaft work is used to reduce the volume of gas and increase the gas pressure. In rotary compressors gas is drawn in through an inlet port in the casing, captured in a cavity and then discharged through another port in the casing on a higher pressure level. The gas is compressed mainly during the discharge process. Both, reciprocating and rotary compressors are positive displacement machines. In axial and centrifugal compressors, also known as turbo-compressors, the fluid is first accelerated through moving blades. In the next step, the

high kinetic energy of the fluid is converted into pressure by decelerating the gas in stator blade passages or in a diffuser. In centrifugal compressors, the flow leaves the compressor in a direction perpendicular to the rotation axis. In axial compressors, flow enters and leaves the compressor in the axial direction. Because an axial compressor does not benefit from the increase in radius that occurs in a centrifugal compressor, the pressure rise obtained from a single axial stage is lower. However, compared to centrifugal compressors, axial compressors can handle a higher mass flow rate for the same frontal area. This is one of the reasons why axial compressors have been used more in aircraft jet engines, where the frontal area plays an important role. Another advantage of axial compressors is that multistaging is much easier and does not need the complex return channels required in multiple centrifugal stages. A variety of turbo-machines and positive displacement machines as well as their ranges of utilization in terms of basic non-dimensional parameters are shown in Fig. 2. The horizontal axis represents the flow coefficient, which is a non-dimensional volume flow rate. The vertical axis shows the head coefficient, which is a dimensionless measure of the total enthalpy change through the stage, and roughly equals the work input per unit mass flow.

The compressor considered in this study is an axial compressor. As shown in Fig. 1, it consists of a row of rotor blades followed by a row of stator blades. The working fluid passes through these blades without any significant change in radius. Energy is transferred to the fluid by changing its swirl, or tangential velocity, through the stage. A schematic diagram of the changes in velocity and fluid properties through an axial compressor stage is shown in the lower diagram of Fig. 1 taken from references Gravdahl (1999) and Japikse and Baines (1994). It shows how pressure rises through the rotor and stator passages.

Early axial compressors had entirely subsonic flow. Since modern applications require compression systems with higher pressure ratios and mass flow rates, designers have permitted supersonic flow, particularly near the leading edge tip where the highest total velocity occurs. Today, most high performance

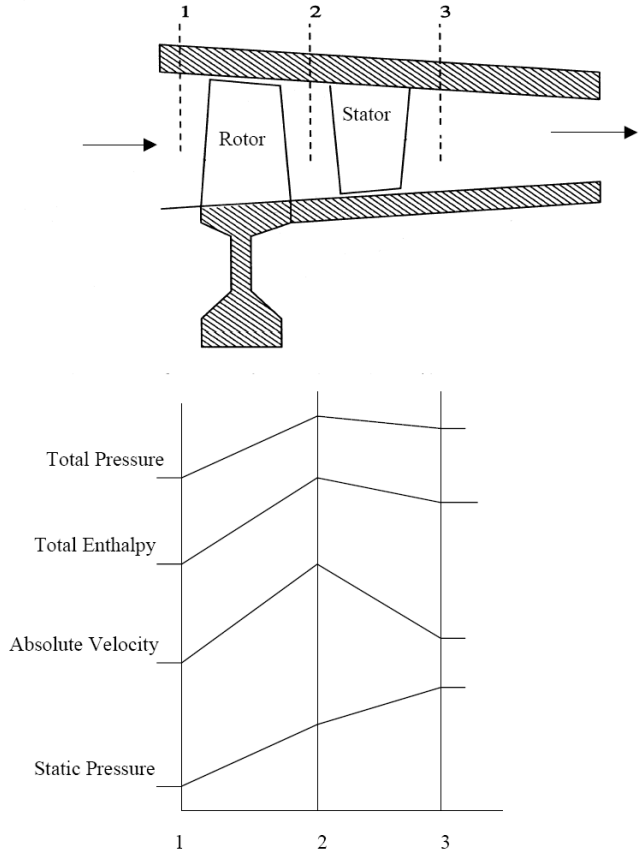

FIG. 1 SCHEMATIC DIAGRAM OF CHANGES IN FLUID PROPERTIES AND VELOCITY THROUGH AN AXIAL COMPRESSOR STAGE

compression stages are transonic, where regions of subsonic and supersonic flow both exist in the blade passages. The steady state performance of a compressor is usually described by a plot of the mass flow rate versus the total pressure ratio. This plot is called the characteristic or performance map of the compressor. The performance map of the four stage compressor used for this work is shown in Section 6.1.

4.2. Flow distortions in compressors

Beside the well known phenomenon of rotating stall and surge, the most recent literature reports other phenomena of flow distortion or even flow instability in compressors, called rotating instabilities (März et al. (2002), Weidenfeller and Lawerenz (2002), Mailach et al. (2001), Kameier and Neise (1997), Baumgartner et al. (1995)), tip clearance noise (Kameier and Neise (1997)), and acoustic resonance (AR).

As will be described more in detail in Chapter 11, rotating stall is a rotating blockage propagating by flow separation in neighbouring channels due to an incidence caused by the blocked channel. Rotating instabilities are interpreted as periodic flow separations on the rotor without blockage. They appear as wide flat peaks in the frequency spectra of pressure signals of pneumatic probes or wall-mounted pressure transducers at a frequency higher than the rotor speed. Wide flat peaks are caused by pressure fluctuations with high damping. The damping is caused by the wash out of the flow separations in the down stream regions of the rotor. The tip-clearance noise looks similar, but it is caused by reversed flow at the rotor tips and is strongly dependent on the tip clearance gap. Compared to these effects, acoustic resonances cause a high and narrow peak in the pressure signal spectrum at a certain resonance frequency. This means compared to a rotating instability the damping is low. Because rotating instability and acoustic resonance may occur in the same frequency range, it is not excluded that a rotating instability works as a driving force for an acoustic resonance.

Unlike the effects mentioned above, acoustic resonances themselves must be explained by an acoustic approach. A simple example of an acoustic resonator is an organ whistle where the tube is a resonator driven by broadband noise caused by shear layers in the flow. The driving forces of a resonance could be aerodynamic effects, like vortex shedding, rotor-stator interaction or shear layers in the flow for example. In turbomachinery, the resonance conditions are typically satisfied only at specific flow conditions.

As will be shown in the next chapter, the relevance of these effects in modern turbomachinery is still under discussion.

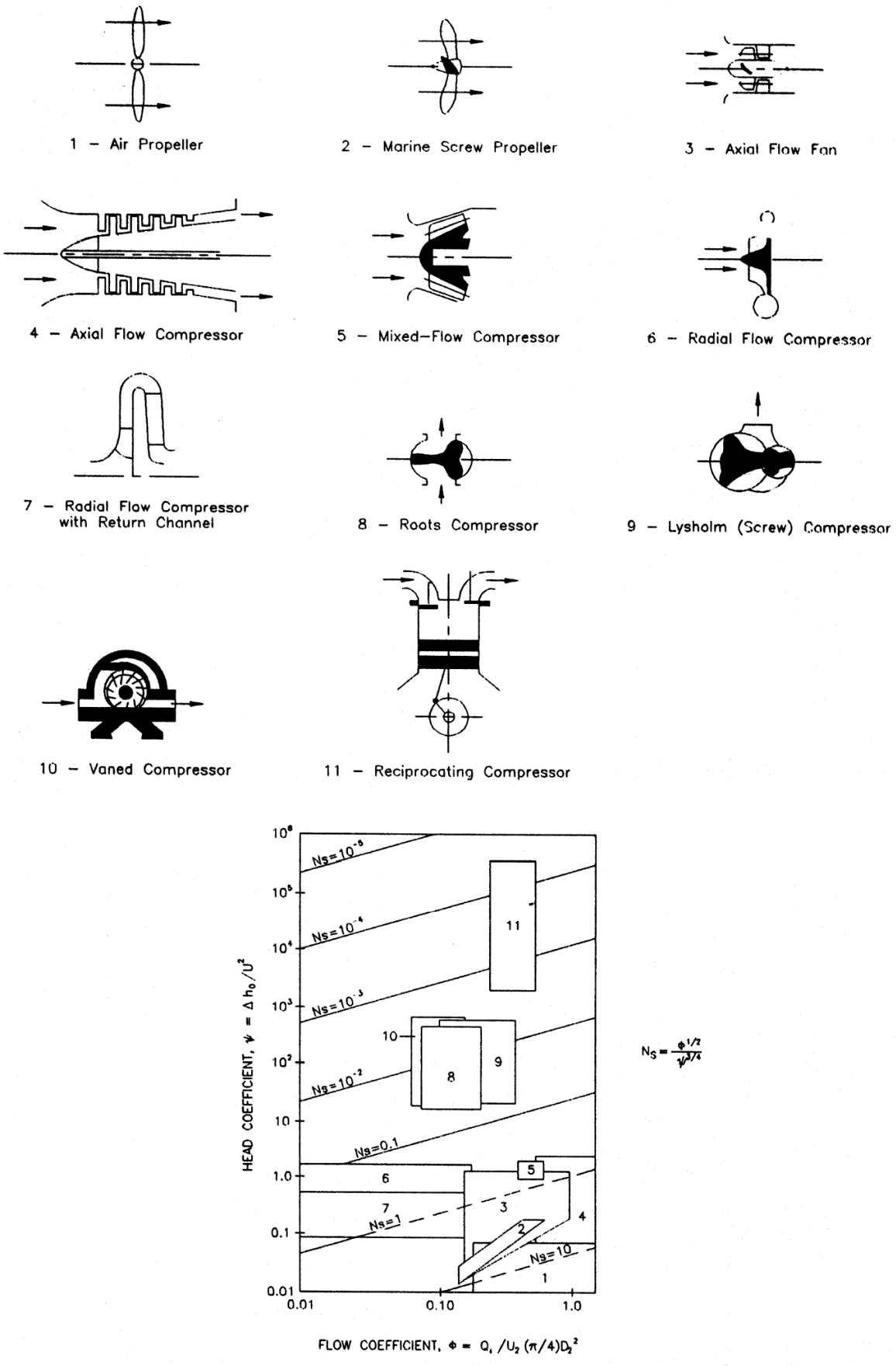

FIG. 2 WORK INPUT MACHINERY CLASSIFICATION (JAPIKSE AND BAINES (1994))

5. Literature Review

In the beginning the main purpose of aero-acoustics was the noise reduction of turbomachinery. Due to the wide use of jet engines in civil aircraft, noise reduction became necessary to avoid high noise emission in the airport areas and inside the planes. After the noise emissions of the trust had been reduced through higher bypass ratios, compressor and fan noise emissions became more relevant. Blade passing frequencies and rotor-stator interaction have been found to be the major noise source of fans and compressor stages. Tyler and Sofrin (1962) and Lighthill (1997) did pioneering work in this field.

Their papers dealt with jet noise and rotor-stator interaction which always occurs at blade-passage frequency or an integer multiple of it with a phase velocity that is a multiple of the rotor speed. By contrast, acoustic resonances are characterised by discrete frequencies which are in general not an integer multiple of rotor speed. Here pioneering work has been done by Parker and co-workers (Parker (1966), Parker (1967), Parker (1984), Parker and Stoneman (1987), Parker and Stoneman (1989), and Legerton et al. (1991)). For instance, in an experiment with plates in a wind tunnel Parker could show that the resonance occurs slightly above the air-speed for which the natural shedding frequency equals the resonance frequency. This frequency was also predicted by solving the acoustic wave equations for the wind tunnel and the plate. The resonances Parker found are standing waves within the blade pitch or between blades and the tunnel wall.

In a similar experiment, Cumpsty and Whitehead (1971) found that the presence of an acoustic field was correlated with the eddy shedding by the plate over the whole span of the plate, while it was correlated over short length scales at off-resonance conditions only.

Compared to the wind tunnel, the conditions in a turbomachine are far more complicated. With regard to this, the transfer of Parker's results to a real machine is fraught with two major problems: Firstly, as will be shown below, the acoustic modes of an annular duct with non-uniform swirl flow, varying cross section, and blade rows are rather complicated. Secondly, the blades in turbomachines are heavily loaded at off-design conditions and the flow speed is high compared to those in Parker's experiments. In view of this, both the acoustics and aerodynamics are more complicated than in the case of Parkers wind tunnel experiments. This does not mean that acoustic resonances could not exist in turbomachinery, but it makes it hard to predict them in advance. Nevertheless, if a machine exhibits resonant behaviour under certain flow conditions, it is sometimes possible to simplify the problem and to show that the anomalous behaviour fits an acoustic resonance.

Before different mathematical approaches for sound propagation through ducts and blade rows will be discussed, some literature on the existence of acoustic resonances in real machines and test rigs will be reviewed.

In one of his early papers, Parker refers to the findings of Rizk and Seymour (1964) who reported an acoustic resonance driven by vortex shedding in a gas circulator at Hinkley Point Nuclear Power Station in the UK.
After the above-mentioned study by Parker, some experimental and theoretical papers on acoustic resonances in turbomachines followed in the 1970s and 1980s. The next acoustic resonance from a real machine reported in the literature to the knowledge of the author is mentioned by Von Heesen (1997). He was facing the problem that the same type of blowers was noisy in some street tunnels, while in others they where not. He found that the noisy ones were running at a different operating point and with a different axial velocity of the flow. As a cause, he found that the frequency of a helical acoustic mode in the duct fitted the vortex shedding frequency of the blades. He suppressed this mode by extending a few stator vanes in axial direction, so that the propagation of helical modes in circumferential direction was suppressed.

Later Ulbricht (2001) found an acoustic mode in a ring cascade. The circumferential phase velocity of the acoustic field she measured was above the speed of sound. This is typical for helical modes as explained in Section 9.4.

In a similar ring cascade, Weidenfeller and Lawerenz (2002) found a helical acoustic mode at a Mach number of 0.482. They showed that the acoustic field was present at the hub and tip of the blades and measured significant mechanical blade stresses at the frequency of the acoustic mode. In a similar way, Kameier (2001) found some unexpected unsteady pressure fluctuations when he tested the aircraft engine of the Rolls Royce BR 710 and BR 715.

Camp (1999) carried out some experiments on the C106 low-speed high-pressure axial compressor and found a resonance quite similar to the acoustic resonance that is the subject of to this work and previous papers of the present author (Hellmich and Seume (2004) and (2006)), i.e. he found a helical acoustic mode. Camp further assumed vortex shedding of the blades as the excitation mechanism. He found Strouhal numbers around 0.8 based on the blade thickness at the trailing edge. He argued that this is far above the usual value of 0.21 for vortex shedding of a cylinder and suggested that this was due to the high loading of the blades. As a consequence, the effective aerodynamic thickness of the blades was higher than the geometric thickness.

Ziada et al. (2002) reported an acoustic resonance in the inlet of a 35 MW Sulzer multistage radial compressor in a natural gas storage station in Canada. The resonance had lead to mechanical vibration levels of the whole compressor resulting in a vibration at the compressor casing above the specified limit of vibration for this class of machines. The resonance was driven by vortex shedding struts and could be eliminated by a modification of the struts' trailing edges. This effect is also well known for tube bundles in heat exchangers.

In a study supported by General Electric, Kielb (2003) found non-synchronous vibrations in a high-speed multi-stage axial-compressor. The size of the compressor was not specified in the paper, but the resonance frequency he found was in the same range as those measured at the rig in this work.

Vignau-Tuquet and Girardeau (2005) analyzed non-engine order pressure fluctuations with discrete frequencies between rotor speed and blade passing frequency (BPF) in a three-stage high-speed compressor test rig. As they measured in the fixed and rotating frame, they were able to make a clear estimation of the circumferential modes of the pressure fluctuation. The mode numbers and rotating speed of the modes fitted an acoustic resonance.

A recent paper by Cyrus et al. (2005) deals with a phenomenon that might be an acoustic resonance. They faced the problem of stator vane damage in the rear stages of an Alstom gas turbine compressor. With pneumatic pressure probes they found that a non-synchronous pressure oscillation with a frequency close to a natural frequency of the damaged blades existed in the rear stages of the compressor. From the measurements and numerical calculations it turned out, that “stalled flow on vane surfaces with vortex flow shedding” (Cyrus et al. (2005)) was responsible for the flow pulsations.

All these cases can be summarized by the following features:

- Acoustic resonances occur in real machines and cascades inside an annulus.
- They occur as non-synchronous pressure fluctuations at discrete frequencies.
- The acoustic field in most cases has a helical structure.
- In most cases vortex shedding was assumed to be the excitation of the resonance.

6. Test facility

The acoustic resonance of the Hannover four-stage high-speed axial compressor has already been discussed in previous papers by Hellmich and Seume (2004) and (2006). However, for a better understanding the results will be summarized in the following section.

6.1. The test rig

A detailed description of the test rig with performance map is given by Fischer et al. (2003), Walkenhorst and Riess (2000), and Braun and Seume (2006). The measurements provided here are measured with the configuration they refer to as the “reference” configuration in their work.

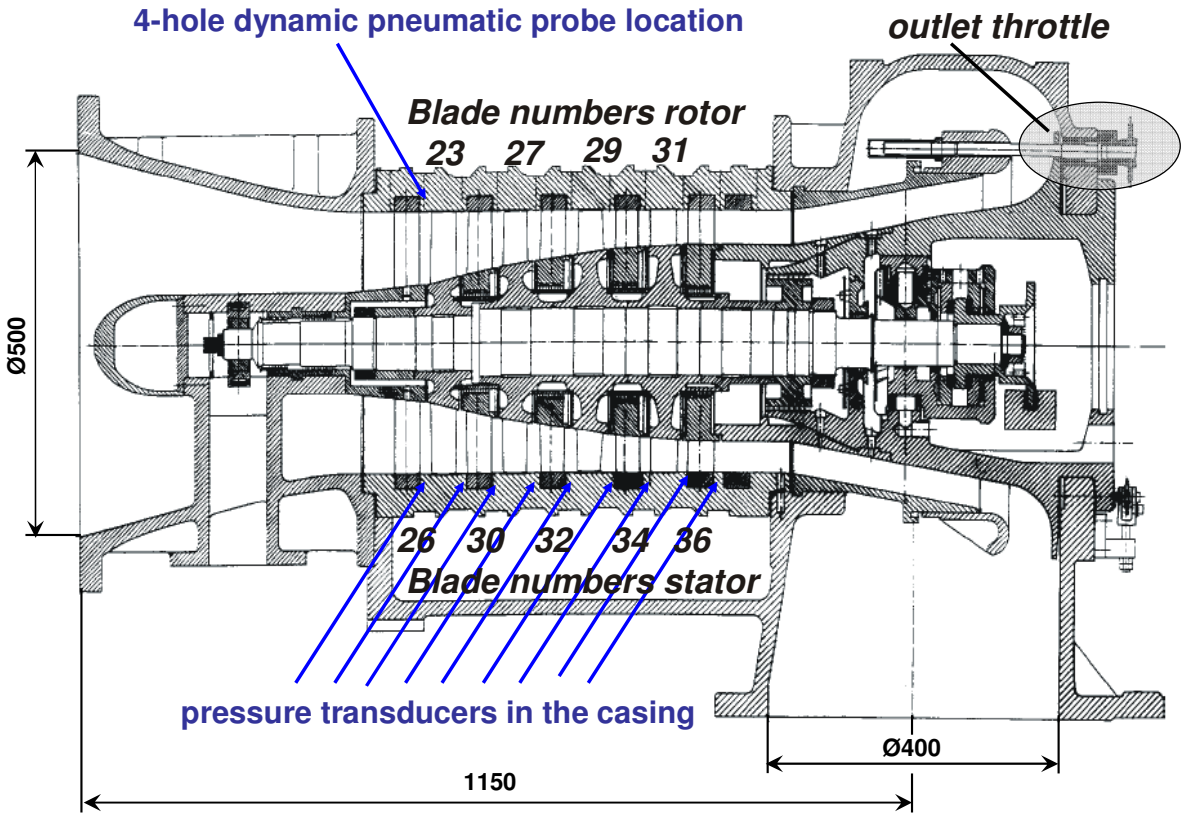

FIG. 3 TURBOMACHINERY LABORATORY FOUR STAGE HIGH SPEED AXIAL COMPRESSOR

max. rotor speed	n_{max}	300 Hz
corrected mass flow with $p_{reference}$ = 60000 Pa	$\dot{m}_{corr}$	8.3 kg/s
inlet total pressure	p_e^0	0.6×10^5 Pa
total isentropic efficiency	η_{is}	88,6 %
total pressure ratio	π	2.98
number of stages	z	4
stage pressure ratio	π_{St}	1.3
outer radius	r_o	170 mm
blade height	h	90 – 45 mm
axial velocity	c_z	190 – 150 m/s
circumferential velocity	c_c	max. 320 m/s
tip clearance gap (cold)	s	0.4 mm
number of rotor blades	N_R	23, 27, 29, 31
number of stator vanes	N_S	26(IGV), 30, 32, 34, 36

TABLE 1 COMPRESSOR DESIGN DATA

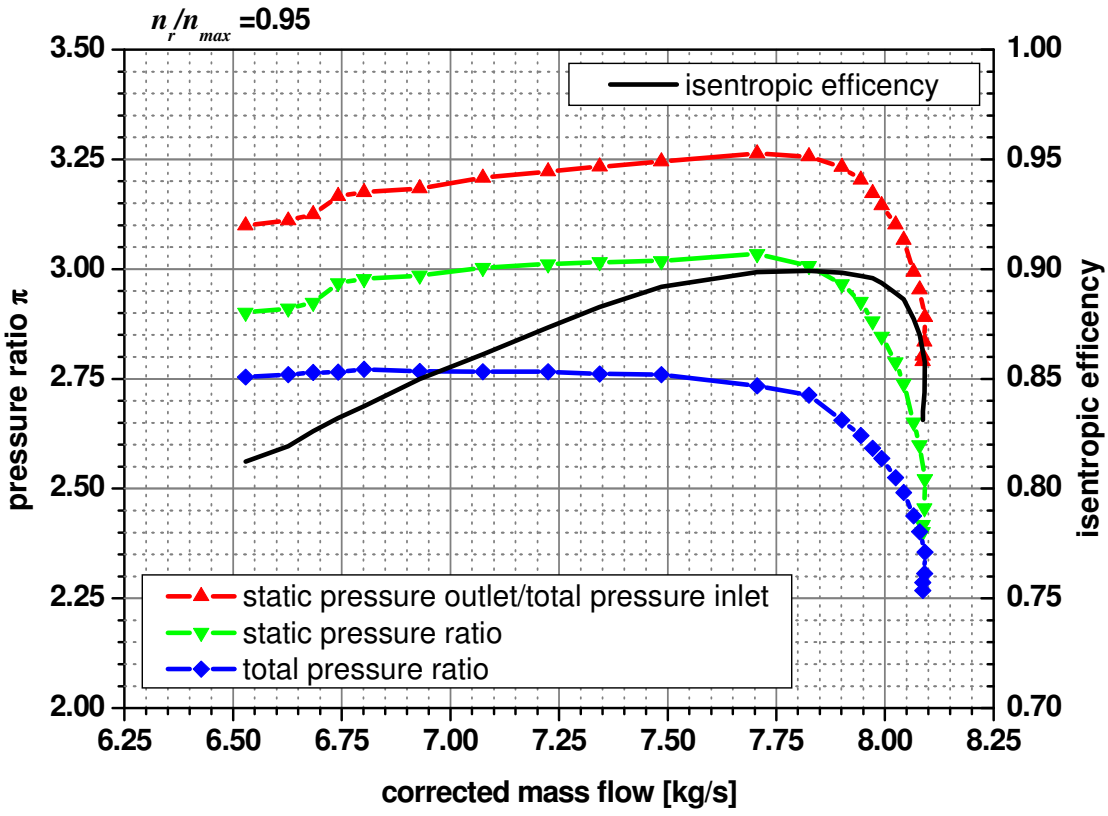

FIG. 4 OPERATING MAP FOR n_r/n_{max} =0.95 (285 Hz)

6.2. Sensors, Signal Conditioning and Data Acquisition

The rotor speed, the position of the throttle and the ten pressure signals (c.f. Table 2 for names and positions) were recorded synchronously with a high-speed data acquisition system. The reduced mass flow and pressure ratio were computed by the compressor operating software and the compressor standard measuring system. The rotor speed was provided by one TTL pulse per revolution. The throttle position was measured by a potentiometer that was connected to a mechanical position indicator of the throttle. The unsteady pressure signal was provided by Kulite XCQ-062 piezo-resistive pressure transducers with a resonance frequency of 300 kHz and a pressure range from –100 to 170 kPa. The transducers had been calibrated against static reference pressure before the measurements were performed. The transducer signal was a voltage difference which was amplified and transformed to single-ended signals.

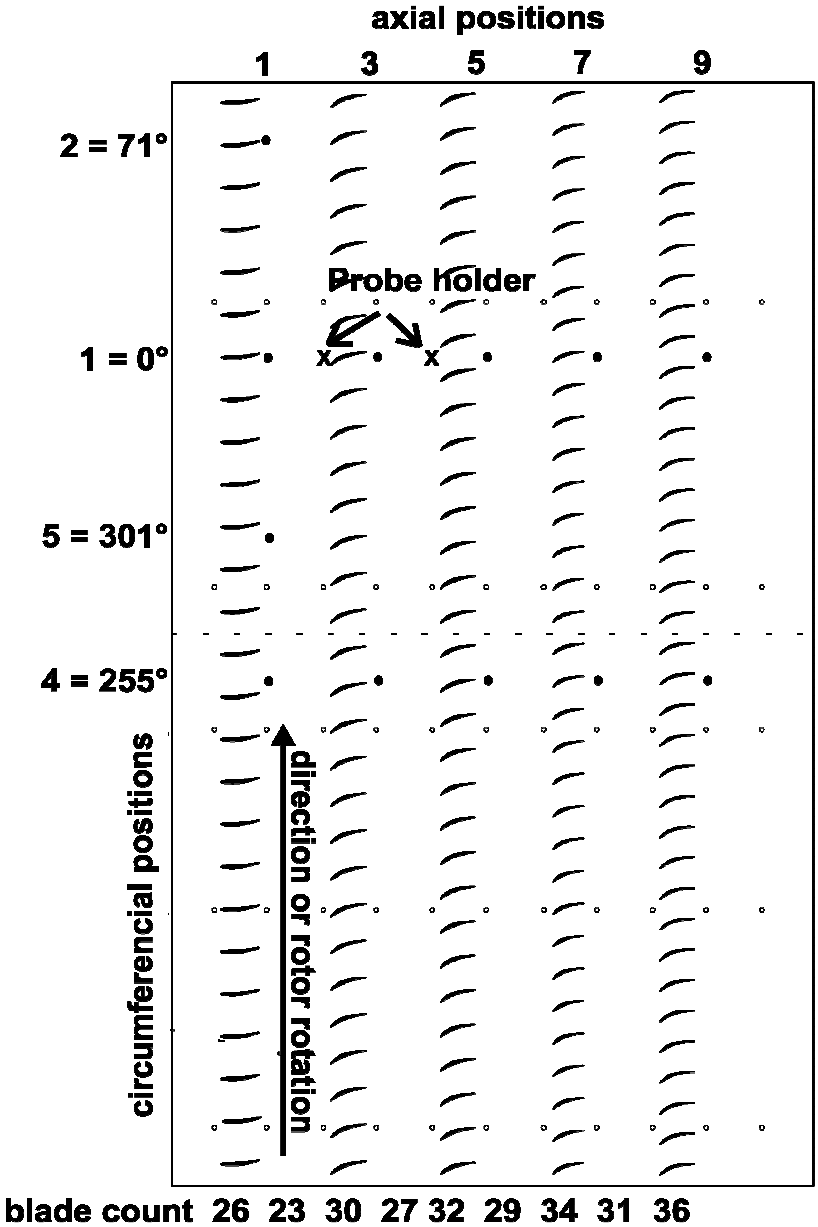

FIG. 5 ROLL UP OF STATOR BLADES WITH SENSOR POSITIONS

Pneumatic Probe (Kulite XCQ-062)					
Total pressure	dto				
Axial Position	Radial Postion [% of channel height]				
	2	5	8	11	14
Behind Rotor 1	95.2 %	86.8 %	50.8 %	15.7 %	5.0 %
Behind Rotor 2	87.8 %	66.2 %	45.9 %	25.7 %	6.8 %
Pressure transducers in the casing (Kulite XCQ-062)					
Circumferencial position	Axial Position in front of				
	Rotor 1	Rotor 2	Rotor 3	Rotor 4	Outlet
0°	d11	d13	d15	d17	d19
71°	d21				
255°	d41	d43	d45	d47	d49
301°	d51				

TABLE 2 SENSOR POSITIONS AND NOMENCLATURE

All unsteady signals were measured by sigma-delta analog-to-digital converters (ADCs) with an input voltage range of ±10 V and 16 Bit resolution. This provided a pressure resolution better than 5 Pa. The ADCs were mounted on a Chico+™ PCI Baseboard produced by Innovative DSP Inc ™. As data logger, an Intel Pentium based server was used. The ADCs had integrated anti-aliasing low-pass filter with a frequency bandwidth of 50% of the sampling rate. The maximum sampling rate was 200 kHz for each channel. For the present experiments, 16 Channels with a sampling rate between 20 kHz and 60 kHz were used.

7. Signal processing methods

7.1. Auto Power Spectral Density (APSD)

Unsteady pressure signals of probes and transducers mounted in turbomachinery usually are a mixture of stochastic and ergodic signal components. The stochastic parts of the signal are background noise of the measuring line and pressure fluctuation due to shear layers in the flow. The ergodic signal components arise from the pressure patterns that are rotating with the rotor of the machine. As to this, they occur as periodic pressure fluctuations in the fixed frame of the flow. The common example therefore is the blade passing frequency (BPF). Beside this, in some cases periodic pressure fluctuations occur which have non engine-order frequencies. Common examples are rotating stall, surge, modal waves, and acoustic modes. Usually, the blade passing frequency and its higher orders are dominating the signal. Other periodic components are often hidden in the background noise since their magnitude is in the same range or even lower than the stochastic background noise.
If a signal contains more than one periodic component, it can be decomposed by a transformation of the time series signal in the frequency domain.
A rather powerful method to find hidden periodic signal components in the background noise of the raw signal in the frequency domain are stochastic estimator functions like the Auto Power Spectral Density (APSD) function. This is the Auto Correlation Function (ACF) in the frequency domain. The ACF of a data set of real values $x(t)$ of length T is defined as

$$ACF_{xx}(\tau) = \frac{1}{T}\int_0^T x(t)x(t-\tau)dt \tag{1}$$

A straight forward method to estimate the APSD is the Fourier transformation of the ACF.

$$APSD_{XX}(f) = \int_0^T ACF_{xx}(\tau)\exp(-2\pi i f\tau)d\tau \tag{2}$$

However, in practice where time series data are given by discrete values, this method produces a high variance in the estimation of periodograms. This could be improved by averaging in the frequency domain. The common method to estimate the APSD with a low variance is described in the next subsection.

7.2. APSD estimation by periodogram averaging method

The periodogram averaging method provides an estimation of the APSD where the variance is reduced by a factor equal to the number of periodograms considered in the averaging (see Bendat and Piersol (2000) for details). Therefore the original sequence is partitioned into smaller non-overlapping segments (or 50% overlapping in some methods), and the periodograms of the individual segments are computed and averaged. Unfortunately, by reducing the number of samples in each sub-sequence through segmentation, the frequency resolution of the estimate is simultaneously reduced by the same factor. This means that for a sequence of a given length there is a trade off between frequency resolution and variance reduction. High frequency resolution and low variance is possible to achieve by using a long data sequence measured under stationary conditions only.

The procedure for generating a periodogram average is as follows:

Partition the original sequence $x[m]$ into multiple segments of equal/shorter length by applying a window function

$$x_k[n] = x[n + kM] \cdot w[n] \tag{3}$$

where the window length is M and $w[n]$ a window function that forces the function $x_k[n]$ to be periodic.

With a Fourier transformation, periodograms of each segment are calculated:

$$S_{XX}^k[f_j] = \left|X^k[f_j]\right|^2 = \frac{1}{M}\left|\sum_{m=0}^{M-1} x_k[m]\exp\left(-i\frac{2\pi jm}{M}\right)\right|^2 \quad \text{and} \quad f_j = jf_s/M \tag{4}$$

with $j=0,1,2,\ldots,M-1$ and f_s as sampling rate of the data acquisition. The assumptions of wide sense stationarity and ergodicity allow us to apply the statistics of the segment to the greater random sequence and random process respectively.

Averaging the segmented periodograms estimates together the APSD:

$$APSD_{XX}[f_j] = \bar{S}_{XX}[f_j] = \frac{1}{K}\sum_{k=0}^{K-1} S_{XX}^k[f_j] \tag{5}$$

where $K = N/M$ is the number of segments.

It should be noted that in some cases other procedures for PSD estimation are more efficient like Auto Regressive Modeling or Multi Taper Method.

The unit of the APSD is $[x]^2$/Hz if $[x]$ is the unit of $x(t)$ and the time is measured in seconds. For practical issues this unit is not always useful. Because of this, in many cases the magnitude function Mag is used. It is given by:

$$Mag[f_k] = \frac{2}{M}\sqrt{APSD_{XX}[f_k]} \tag{6}$$

Its unit is the same as $x(t)$.
Due to Parsevals theorem, the integral of a function f(t) over all times equals the integral over its Fourier transformed function $F(f)$ over all frequencies. This makes it possible to normalize the APSD to the variance of a time signal used for the APSD estimation. The variance is given by:

$$Var(x(t),T) = \frac{1}{T}\int_0^T (x(t)-\bar{x})^2\,dt \tag{7}$$

In this work all APSDs are normalized so that the following equation is fulfilled:

$$Var(x[n],N) = \frac{1}{N}\sum_{n=0}^{N-1}(x[n]-\bar{x})^2 = \sum_{m=0}^{(M/2)-1} APSD_{XX}[f_m] \tag{8}$$

Because the APSD is an even function it must be summed up only for the positive frequencies. For the negative frequencies the sum is the same so that the sum over all frequencies is two times the sum over the positive or the negative frequencies. The common normalization is given by:

$$Var(x[n],N) = \frac{1}{N}\sum_{n=0}^{N-1}(x[n]-\bar{x})^2 = \Delta f \sum_{m=0}^{(M/2)-1} APSD_{XX}[f_m] \text{ with } \Delta f = \frac{f_s}{M} \tag{9}$$

The normalization used here is uncommon and already includes the normalization to the frequency resolution Δf. So the APSD used here is in reality not a density anymore. In correct words it should be called Auto Power Spectrum (APS), but this is not done here. The signal processing tools used for the processing of the data in the next chapters are using this uncommon normalization and hence it is used here, too. In this convention the standard deviation of a signal is given by:

$$s.d.(x[n],N) = \sqrt{Var(x[n],N)} = \sqrt{\sum_{m=0}^{(M/2)-1} APSD_{XX}[f_m]} \tag{10}$$

If we assume a time signal $x_f[n]$ filtered with a narrow band pass filter of band width $\Delta f = f_s/M$ around the center frequency of f_m, the standard deviation of this signal would be

$$s.d.\left(x_f[n], N\right) = \sqrt{APSD_{XX}[f_m]} \tag{11}$$

In other words, the normalization makes it possible to use the effective oscillation amplitude given by the standard deviation, which in turn could be derived directly from the APSD. However, this only applies to cases where the peak caused by the oscillation in the spectra spreads over only one frequency slot. In reality, this is usually not the case. With regard to this, a correct estimation would require the summation of the APSD over the width of the peak, which varies from peak to peak. So, as a compromise we introduce a magnitude function using a moving window for summing up the amplitude at the center frequency together with the amplitudes of the neighboring frequency slots.

$$Mag_{XX}[f_m] = \sqrt{\sum_{i=m-1}^{m+1} APSD_{XX}[f_i]} \tag{12}$$

So the peak value of a wide peak in a magnitude spectra is an over prediction of the effective oscillation amplitude of the associated oscillation, because the root of a sum of values is always less than the sum of the roots of the single values.

A special case is the harmonic analysis. Here, the averaging is done in the time domain and the FFT is performed from the averaged data. In this case the magnitude is estimated directly from the FFT with

$$Mag_{XX}[f_m, N] = \frac{2}{N}\sqrt{\mathrm{Re}(X[f_m])^2 + \mathrm{Im}(X[f_m])^2} \tag{13}$$

where X is the Fourier transformation of x and N is the length of the window used for the discrete Fourier transformation.

7.3. Cross power spectral density (CPSD), phase, and coherence

Analog to the calculation of the power spectral density of a signal with it self, the power spectral density of two different time series $x[n]$ and $y[n]$ can be calculated with same procedure. The resulting function

$$CPSD_{XY}[f_j] = \overline{S}_{XY}[f_j] = \frac{1}{K}\sum_{k=0}^{K-1} S_{XY}^k[f_j] \text{ with } S_{XY}^k[f_j] = X^k[f_j]^* \cdot Y^k[f_j] \tag{14}$$

is a complex function and is called cross power spectral density (CPSD). It is the analogue to the cross correlation function in the frequency domain.

The ratio

$$\gamma_{XY}^2\left[f_j\right]=\frac{\left|CPSD_{XY}\left[f_j\right]\right|^2}{APSD_{XX}\left[f_j\right]APSD_{XY}\left[f_j\right]} \tag{15}$$

is called coherence function. The co-domain are real numbers between zero and one. If the value is zero there is no common component with this frequency in the input signals. If the value is one, the whole signal at this frequency has a common source. Common component/source means that both input signals have components with a common frequency and phase shift at this frequency, which do not change within the sequence used for the PSD calculation.

The phase function is the phase shift θ_{xy} as a function of frequency between coherent components of two different signals.

$$\theta_{XY}\left[f_j\right]=\arctan\frac{\mathrm{Im}\left(CPSD_{XY}\left[f_j\right]\right)}{\mathrm{Re}\left(CPSD_{XY}\left[f_j\right]\right)} \tag{16}$$

In many cases the use of estimators based on two sensor signals like the coherence and phase function improves the performance of the signal analysis by minimizing the influence of uncorrelated noise on the analysis.

Again, a special case is the harmonic analysis because of the special properties mentioned above. Also, the data are synchronized to a reference signal, so that the phase of the signal itself has a physical meaning and not only the phase shift relative to a second signal. Thus, in this case the phase function is estimated directly from the FFT with

$$\theta_{XX}\left[f_j\right]=\arctan\frac{\mathrm{Im}\left(X\left[f_j\right]\right)}{\mathrm{Re}\left(X\left[f_j\right]\right)} \text{ with } 0<j<N \tag{17}$$

where X is the Fourier transformation of x and N is the length of the window used for the discrete Fourier transformation.

7.4. Coherent transfer functions

For constant-parameter linear systems the deformation of a signal $y[t_n]$ by physical processes could be expressed by a convolution of the input signal $x[t_n]$ with a transfer function $h[t_n]$. A system has constant parameters if all fundamental properties of the system are invariant with respect to time. A system is linear if the response characteristics are additive and homogeneous.

In the frequency domain a convolution is a multiplication and so the transfer function $H[f_n]$ is the ratio of the output function $Y[f_n]$ to the input function $X[f_n]$.

$$H[f_n] = \frac{Y[f_n]}{X[f_n]} = \frac{|Y[f_n]|}{|X[f_n]|} e^{i(\varphi_Y[f_n] - \varphi_X[f_n])} \tag{18}$$

Even so, in reality the output signal is contaminated with noise $N[f_n]$ that is independent from the input signal.

$$Y[f_n] = H[f_n] \cdot X[f_n] + N[f_n] \tag{19}$$

An Estimator that minimizes the noise is called optimal estimator. In Bendat and Piersol (2000), the authors showed that the optimal estimator for the transfer function $\hat{H}[f_n]$ is

$$\hat{H}[f_n] = \frac{CPSD_{XY}[f_n]}{APSD_{XX}[f_n]} \tag{20}$$

and that its auto power spectral density is given by

$$APSD_{\hat{H}\hat{H}}[f_n] = \frac{|CPSD_{XY}[f_n]|^2}{APSD_{XX}^2[f_n]} = \gamma^2[f_n] \cdot \frac{APSD_{YY}[f_n]}{APSD_{XX}[f_n]} \tag{21}$$

The APSD of the transfer function shows at which frequency the signal is damped and where it is amplified. An estimator for the phase shift $\varphi_Y[f_n] - \varphi_X[f_n]$ in formula (20) is the phase function $\theta_{XY}[f_j]$ as defined in formula (17) because

$$\theta_{XY}[f_j] = \frac{\mathrm{Im}(CPSD_{XY}[f_n])}{\mathrm{Re}(CPSD_{XY}[f_n])} = \frac{\mathrm{Im}(\hat{H}[f_n] / APSD_{XX}[f_n])}{\mathrm{Re}(\hat{H}[f_n] / APSD_{XX}[f_n])} = \frac{\mathrm{Im}(\hat{H}[f_n])}{\mathrm{Re}(\hat{H}[f_n])} \tag{22}$$

7.5. Statistical Errors of coherence, power and phase spectra

Following Bendat and Piersol (2000) with formula 9.73 in their book the normalized random error of an estimator function is given by

$$\varepsilon\left[\hat{G}_{vv}(f)\right]=\frac{\sigma\left(\hat{G}_{vv}(f)\right)}{G_{vv}(f)}=\sqrt{\frac{2-\gamma_{XY}^2(f)}{\gamma_{XY}^2(f)\cdot n_d}} \tag{23}$$

with $\hat{G}_{vv}$ as estimator function of G_{vv}, the standard deviation $\sigma\left(\hat{G}_{vv}\right)$ and n_d as number of averages used for the calculation of the coherence function. Yet, the authors recommend that the coherence function as it is introduced in (15) itself is an estimator of a real coherence involving bias errors from a number of sources, just like the transfer function estimators. They summarize these errors as follows :

1.) Inherent bias in the estimation procedure
2.) Bias due to propagation time delays
3.) Nonlinear and/or time varying system parameters
4.) Bias in auto-spectral and cross-spectral density estimates
5.) Measurement noise at the input point
6.) Other inputs that are correlated with the measured input

There is no general way to avoid all these errors or to make a correction of the estimated values. Still, in most cases 1.) may be neglected if the random error from (23) is small. 2.) can be avoided if the window length used for the FFT is long compared to the traveling time of the observed phenomena. For example, the time of a pressure pattern traveling with the flow from one sensor to another should be small compared to the window length. If this is not the case the bias error might be corrected by

$$\hat{G}_{xy}\approx\left(1-\frac{\tau}{T}\right)\hat{G}_{xy} \tag{24}$$

with T as window length and τ as traveling time. For 3.) such kind of treatment does not exist. Here the problem has to be solved from the physics. This means that the bias error is smaller if the system fulfills the conditions of a constant parameter linear system. Point 4.) causes serious errors if two peaks are in one frequency slot. This could be avoided by an improved frequency resolution. Point 5.) and 6.) must be treated in the experiment by minimizing unwanted sources at the input point. If this is not possible but the sources are known, corrections might take place (see for example Bendat and Piersol (2000) for details).

For the coherence itself, the relative random error is approximately given by

$$\varepsilon\left[\hat{\gamma}_{xy}^2(f)\right] \approx \sqrt{\frac{2}{\gamma_{XY}^2(f)\cdot n_d}}\left(1-\gamma_{XY}^2(f)\right) \tag{25}$$

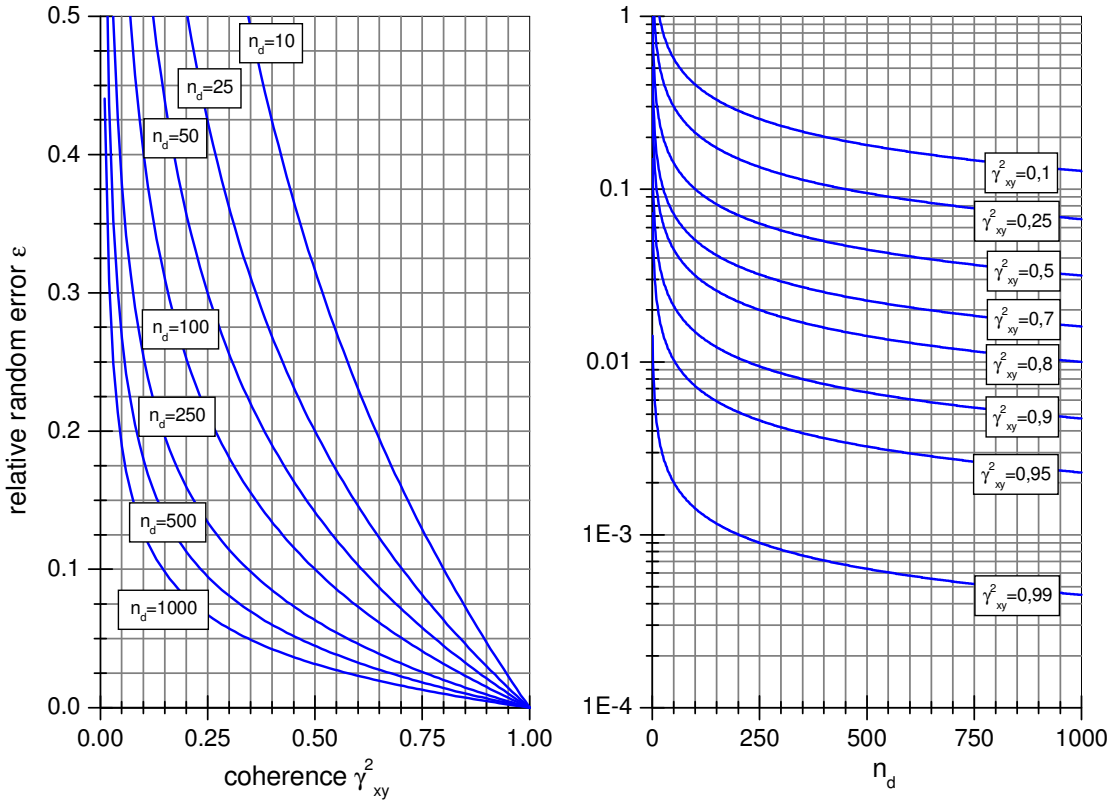

FIG. 6 RELATIVE RANDOM ERROR OVER COHERENCE AND NUMBER OF AVERAGED WINDOWS

In Tab. 9.6 in reference Bendat and Piersol (2000) the normalized random error of common estimator functions are summarized. For power spectral density function and coherence the formulas are given by (23) and (25). For the transfer function it is given by :

$$\varepsilon\left(\left|\hat{H}_{xy}(f)\right|\right) = \sqrt{\frac{1-\gamma_{XY}^2(f)}{2\cdot\gamma_{XY}^2(f)\cdot n_d}} \tag{26}$$

For the phase, the normalized random error can not be used, but the standard deviation in degrees is approximately given by:

$$\sigma\left(\hat{\theta}_{xy}(f)\right)[°] \approx \frac{180°}{\pi}\sqrt{\frac{1-\gamma_{XY}^2(f)}{2\cdot\gamma_{XY}^2(f)\cdot n_d}} \tag{27}$$

7.6. Spectral leakage

The variance of the PSD is:

$$\lim_{N\to\infty}\left(\mathrm{var}\left[\hat{S}_{xy}(\omega)\right]\right)=\frac{M(N)}{N}\mathrm{var}\left[\hat{S}_{xy}(\omega)\right]\approx\frac{M(N)}{N}S_{xy}^{2}(\omega),\ N\to\infty \tag{28}$$

While increasing the number of windows the variance of the estimation decreases. However, the shorter segments within each window also result in a loss of frequency resolution as well as some distortion in the estimate due to increased “spectral leakage”.
A pure sinusoidal infinite signal would result in an infinite peak at the frequency of the signal (Dirac pulse). Real time series are finite but they can be treated as infinite signals multiplied with a rectangular window of finite length. The windowing of the signal in the time domain is a convolution in the frequency domain. Beside a peak at the signal frequency, also side peaks with lower amplitude occur due to the finite measuring time. Owing to this, the energy of the signal is distributed to one main peak and small side peaks. This effect is called spectral leakage.

This problem can be addressed by varying the window function w[n]. Common window functions are:

- Rectangular $w[n]=1$
- Triangular $w[n]=\frac{N}{2}-\left|n-\frac{N-1}{2}\right|$
- Gaussian $w[n]=\exp\left(-\frac{1}{2}\left(\frac{2n-(N-1)}{0.4\cdot(N-1)}\right)^{2}\right)$
- Hanning $w[n]=\frac{1}{2}\left(1-\cos\left(\frac{2\pi n}{N-1}\right)\right)$
- Hamming $w[n]=0.53836-0.46164\cdot\cos\left(\frac{2\pi n}{N-1}\right)$
- Blackman $w[n]=0.42-0.5\cdot\cos\left(\frac{2\pi n}{N-1}\right)+0.08\cdot\cos\left(\frac{4\pi n}{N-1}\right)$

(29)

In Fig. 8 the effect of spectral leakage is shown for different types of window functions by the APSD of a pure sinus function. In the diagrams on the left, the window length is a multiple of the period of the input function. This means that the periodic boundary condition is satisfied without the use of any window function as with the application of a rectangular window function. In this case the other window functions reduce the frequency resolution and amplitude resolution at the same time and have no positive effect. In general, though, the frequencies of all signal components do not fit with the window length. If the signal is dominated by a fundamental frequency with higher harmonics, as for instance with pressure signals of an undisturbed flow in

turbomachines or the shaft vibration in a bush bearing, the window length could be fitted to the fundamental frequency by a resampling of the signal in the time domain. On the other hand, for signals that include non engine-order components, this method does not work anymore. As shown by the diagrams on the left of Fig. 8, in this case, the application of window functions has a positive effect on the signal analysis. Again, the frequency resolution decreases by the widening of the peak, but the amplitude resolution increases. The amplitude at the peak maximum is decreasing since the window functions are damping the signal at the edges of the window. This effect could be compensated by window-function depended correction factors (see table 3).

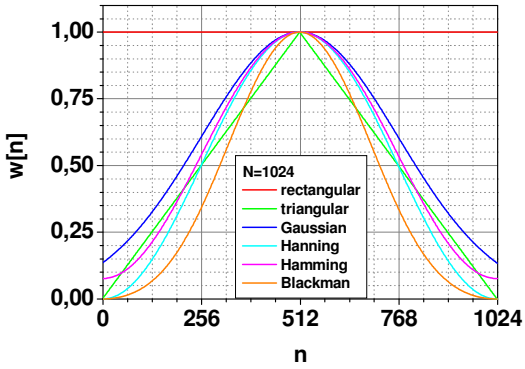

FIG. 7 WINDOW FUNCTIONS

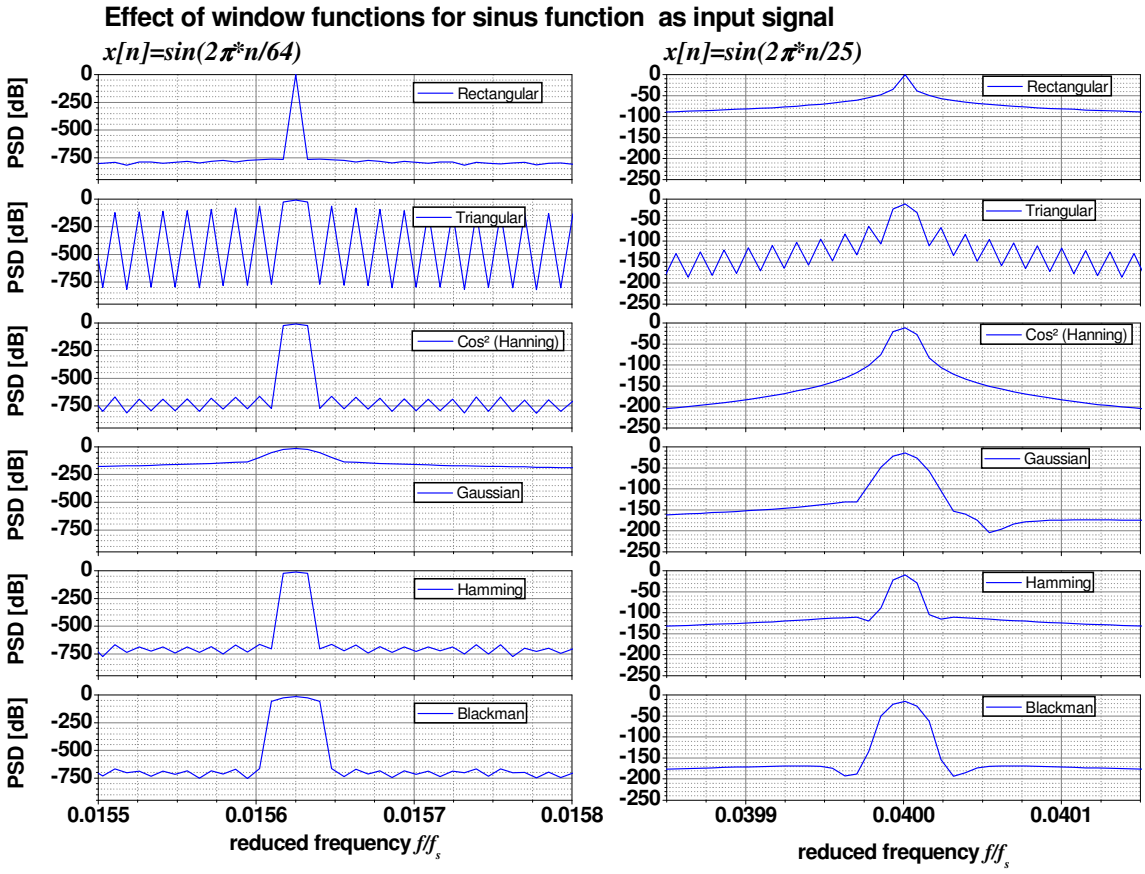

FIG. 8 SPECTRAL LEACKAGE EFFECT FOR DIFFERENT WINDOW FUNCTIONS

The effect of averaging is another important factor if a high amplitude resolution is necessary. The top diagram in Fig. 9 shows a segment of a synthetic time signal composed of a white noise signal and a sinus signal. The amplitude of the noise signal varies from plus to minus ten and those of the sinus signal from plus to minus one. The ratio of the RMS-Values of both signal components is 8.16. The diagrams below the time series show the power spectral density of the composed signal taken from a 131072 samples long sequence. While in the raw time series the sinus signal is hidden by the white noise, the signal in the frequency domain is decomposed and consequently the sinus function gets noticeable as peak in the spectra. With an increasing number of averages, the variance of the white noise background band is decreasing. Furthermore, the amplitude of the peak decreases. However, the peak also gets wider because the shorter windows taken for a FFT resulting in a decreasing frequency resolution. The energy of the sinus function is distributed over more frequency slots and so the density within those slots is decreasing. A compromise is necessary where the frequency resolution remains acceptable and the amplitude resolution is increased. In our example this would be something between four and sixteen averages.

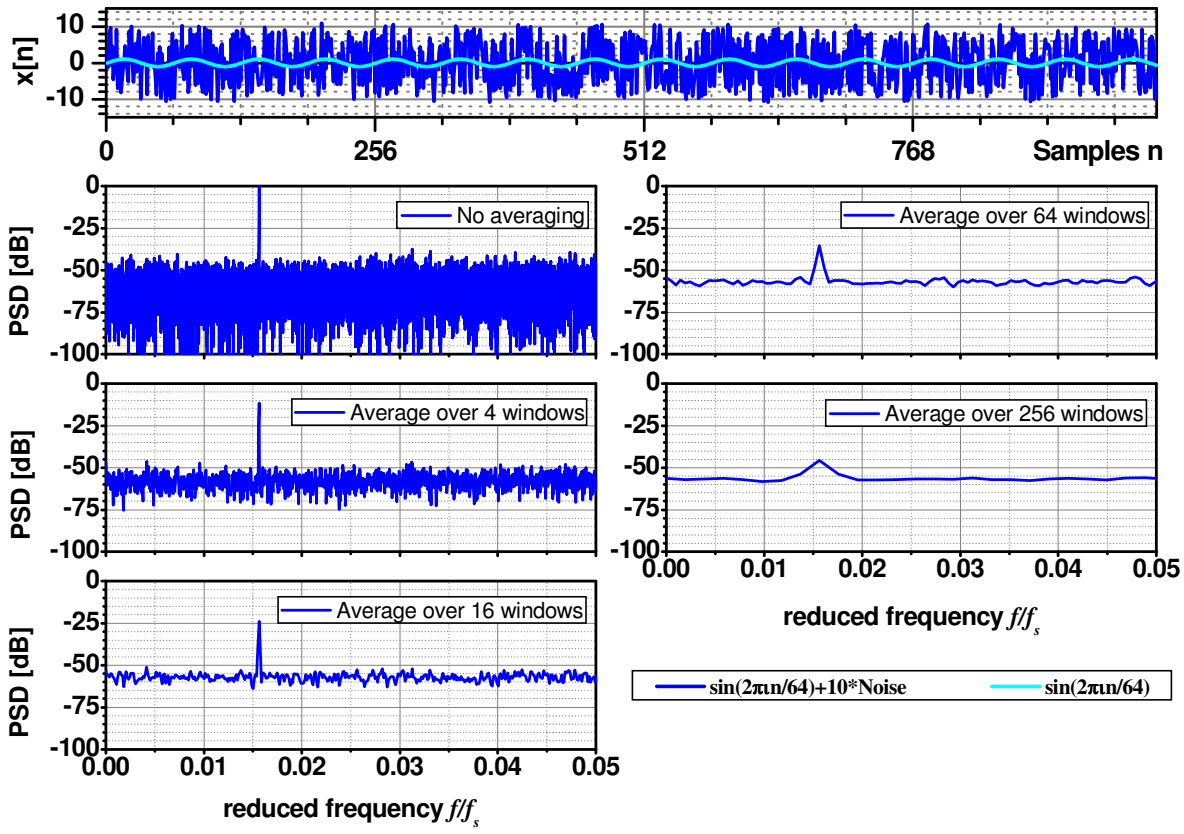

FIG. 9 EFFECT OF AVERAGING ON PSD

The multiplication of the time series data with a windowing functions is affecting the estimation of the magnitude function. Depending on the window function that has been used, the magnitude function must be divided by a constant factor. These factors are shown in Table 3.

window function	**correction factor**
rectangular	1.495
triangular	0.913
Gaussian	0.849
Hanning	0.969
Hamming	1.0
Blackman	0.867

TABLE 3 MAGNITUDE CORRECTION FACTORS

8. The Phenomenon

The non-harmonic acoustic resonances were detected in static pressure signals of transducers in the compressor casing and in the signals of an unsteady pneumatic flow probe when the compressor was operating close to the stall limit. The static pressure transducers were placed behind the stator and rotor rows in three lines with each line at a different circumferential position (see the test rig in Fig. 3). Originally the experiments where carried out by a research team for an examination of rotating stall inception in the compressor. Because of this, the setup was optimized for stall detection. It turned out, however, that the results were still useful for an acoustic analysis because the measured sound level at resonance was comparatively high. Already at that time, the phenomenon had been noticed, but had been interpreted as structural vibrations (Methling and Stoff (2002)) or mild multi-cell rotating stall (Levy and Pismenny (2005)).

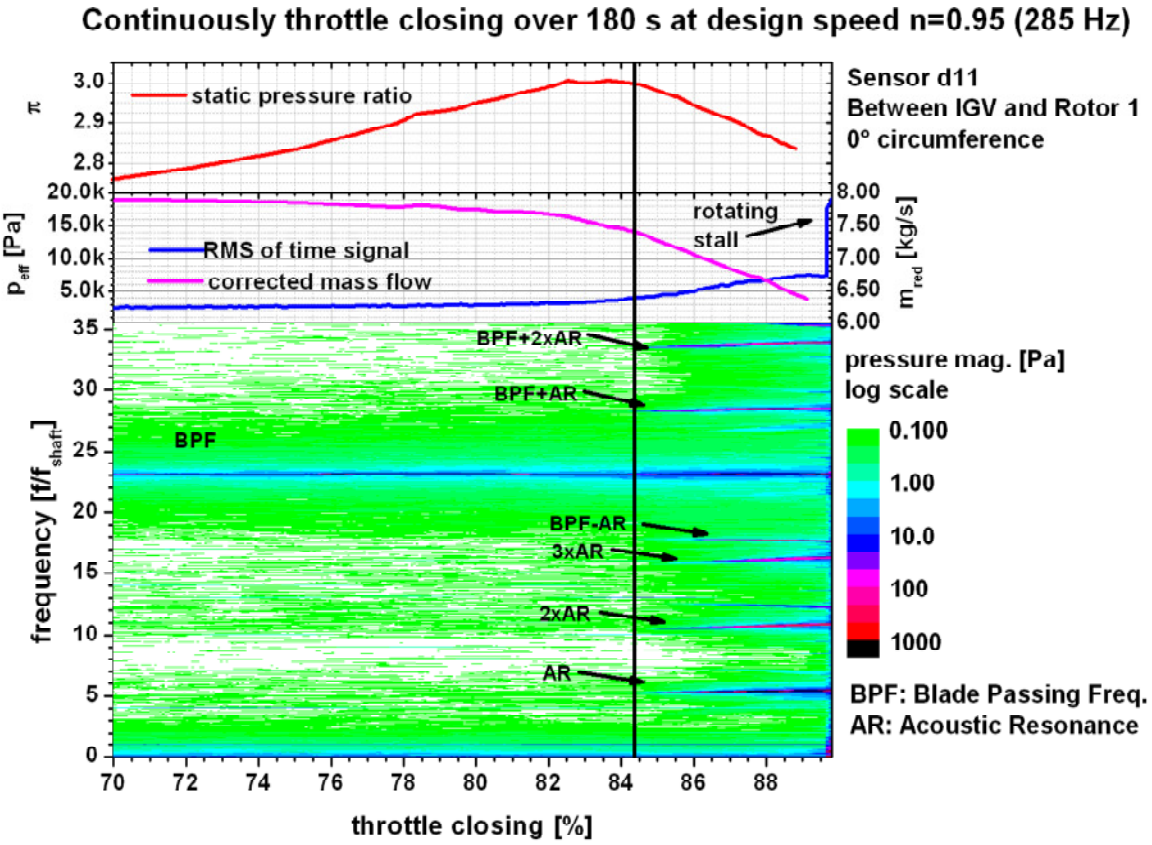

FIG. 10 CONTOUR PLOT OF STATIC WALL PRESSURE IN STAGE 1

By throttling the compressor with a ring throttle at its outlet and keeping the rotor speed constant, the operating point of the compressor is shifted to lower mass flows on the speed line in Fig. 4. The pressure amplitude of a dynamic pressure transducer in the casing between IGV and first rotor in front of the compressor is plotted against frequency and throttle position in the contour plot in Fig. 10. Red colour indicates high

pressure and green colour low pressure. The pressure signal is dominated by the BPF of the first rotor (23 Blades) until the static pressure ratio reaches its maximum at about 84.2% of throttle closing. After reaching this maximum in the frequency range above five times the rotor speed, a new frequency component occurs with higher harmonics and beat frequencies with the BPF. (The spectrum of a harmonic oscillation (carrier) modulated with another harmonic oscillation shows in the frequency domain peaks at the carrier frequency plus and minus the modulation frequency. They are called beat frequencies.) The new frequency is the acoustic resonance and is marked with AR in Fig. 10.

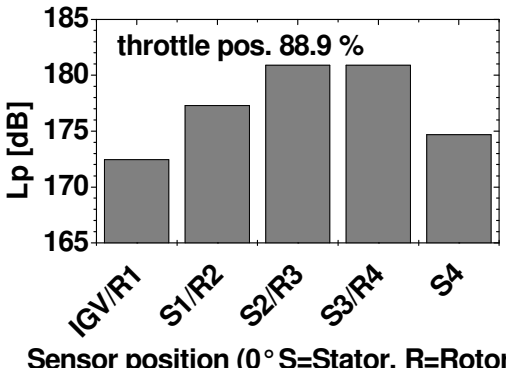

FIG. 11 ACOUSTIC PRESSURE LEVEL CLOSE TO STABILITY LIMIT AT N=0.95 (285 HZ)

The colours in the contour plot and the spectra in Fig. 12 show that the pressure level of the acoustic resonance exceeds the level of the usually dominant blade passing frequency when the machine is running close to the stability limit. Additionally, Fig. 12 shows the resonance at a fundamental frequency that is the same in each stage of the compressor. At a throttle position of 89.9% the pressure level at the resonance frequency in the middle of the compressor is over 180 dB (see Fig. 11).

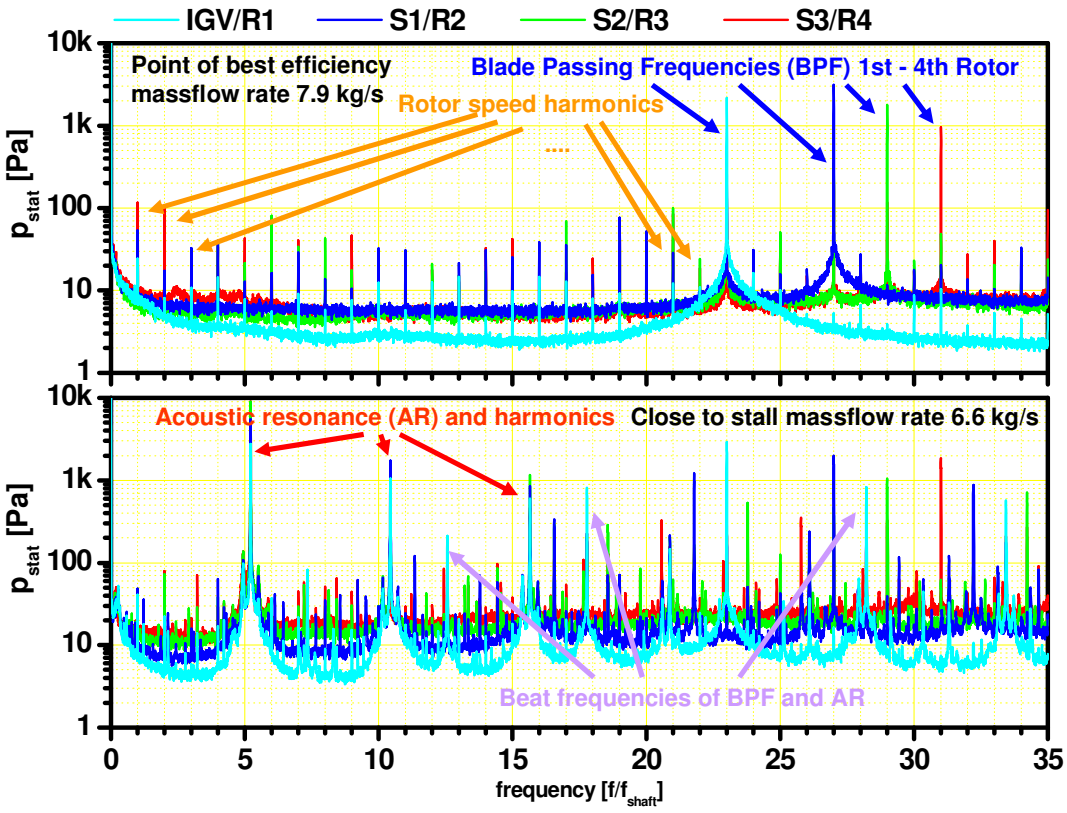

FIG. 12 POWER SPECTRA OF WALL PRESSURE SIGNALS

During the last five years different CDA Blades have been tested in the compressor. The assumption was that those blades with bow (Fischer et al (2003) and Fischer (2005)) and forward sweep (Braun and Seume (2006)) will shift the stall margin to lower mass flows compared to a reference configuration with non-dihedral blades. In the experiment, the different blade configurations showed that the bow and sweep blades increase the performance of the compressor and lead to higher pressure ratios, like it has been calculated with a three dimensional CFD Model. However, neither bow vanes in the rear stages nor sweep blades and sweep vanes shifted the stall margin at design speed to lower mass flows as they did in other compressors. Being so, the measurements showed that the dihedral blades reduced the corner stall in the compressor, but this has not led to an extension of the operating map. At lower rotor speeds like 0.8 and 0.55 times the maximum rotor speed, the stall margin was shifted to lower mass flows by the dihedral blades. However, at this low rotor speeds no acoustic resonance was excited. So the dihedral blades shifted the stall margin only in those regions of the operating map where no acoustic resonance was excited.
Another experiment aimed at enhancing the compressor stability by injecting discrete air with bleeds in the compressor casing in front of the first stage (Reissner and Seume (2004)). With this tip injection, the flow at the blade tips should be stabilized at low mass flow rates in the compressor resulting in a shift of the stall margin to lower mass flow. In similar experiments (Leinhos and Scheidler (2002) and Sunder et al. (2001)) this was successfully achieved while in the case of the TFD compressor, the stall margin never shifted significantly.
To sum up, the suppression of tip and corner stall by dihedral blades and vanes in the last three stages of compressor did not extend the stall margin. Nor could this be attained by the air injection at the rotor tips of the first stage. This leads to the assumption that the stall in the compressor is triggered by an effect that is not affected by the blade design or the tip flow of the first stage.
On the other hand, none of the mentioned modifications of the compressor had a significant influence on the excitation of the acoustic resonance. The resonance occurs more or less in the same manner irrespective of the kind of blades that had been used. Even a reduction of blades in the stator vanes did not result in a significant change in the behaviour of the acoustic resonance.
Unsteady measurements in the last milliseconds before the compressor stalls show that the decreasing Mach number of the mean flow is shifting the frequency and phase velocity of the acoustic resonance to a quasi rotor harmonic frequency. Modal waves detected as pre-cursor of the rotating stall are modulating the pressure amplitudes of the acoustic resonance. So a link between the acoustic resonance and rotating stall inception is assumed. This will be discussed more in detail in section 11.3.

8.1. Acoustic resonance versus multi-cell rotating stall

Because the compressor is operating close to the stability limit when the AR occurs, the first assumption was that the observed phenomenon is a mild multi-cell rotating stall. However, a rotating stall always has a propagation speed below rotor speed (Cumpsty (1989)). The frequency of a rotating stall f_{stall} measured in a static pressure signal at the compressor casing is given by the number of stall cells *n*, the propagation speed v_{stall} and the outer diameter *d* of the compressor.

$$f_{stall} = n\frac{v_{stall}}{2\pi d} \tag{30}$$

Therefore the present stall must have at least six cells, since the observed frequency is above five times the rotor speed. The number of stall cells can be calculated form the phase shift $\alpha(f_{stall})$ between two sensors at the same axial position and different circumferential positions. Due to the fact that the phase shift is ambiguous in an interval of 360°, one needs at least two pairs of sensors with a circumferential distance to each other such that one is not an integer fraction of the other. In the test rig, this condition is fulfilled by sensors d11, d41, and d51 (see nomenclature and Fig. 5 for sensor positions).

The circumferential velocity of a rotating stall cell is a special case of the phase velocity v_{Ph} of a rotating wave, because the pressure distribution of the stall cell can be treated as a non-acoustic wave. With formula (31), the phase velocity may be calculated for n periods around the circumference or in the special case of a rotating stall as n stall cells. β is the circumferential separation of the sensors in the casing and α the measured phase shift at frequency f for two sensors with a distance β.

$$v_{Ph} = f \cdot 2\pi d \cdot \frac{\beta}{360°} \cdot \left((n-1) + \frac{\alpha(f,\beta)}{360°} \right) \tag{31}$$

The relative deviation Δv_{ph} is given by formula (32) for all n between 1 and 15 has been calculated.

$$\Delta v_{Ph}(n)[\%] = 200\frac{v_{Ph}(n,\alpha(f,\beta_1)) - v_{Ph}(n,\alpha(f,\beta_2))}{v_{Ph}(n,\alpha(f,\beta_1)) + v_{Ph}(n,\alpha(f,\beta_2))} \tag{32}$$

In Fig. 13 $\Delta v_{ph}(n)$ is calculated for phase shifts measured at a throttle position of 87.5%. The curve shows a clear minimum for n = 3. The phase velocity of the AR is about 540m/s depending on the operating condition. This means, that the AR cannot be a multi-cell rotating stall (Hellmich et al. (2003)).

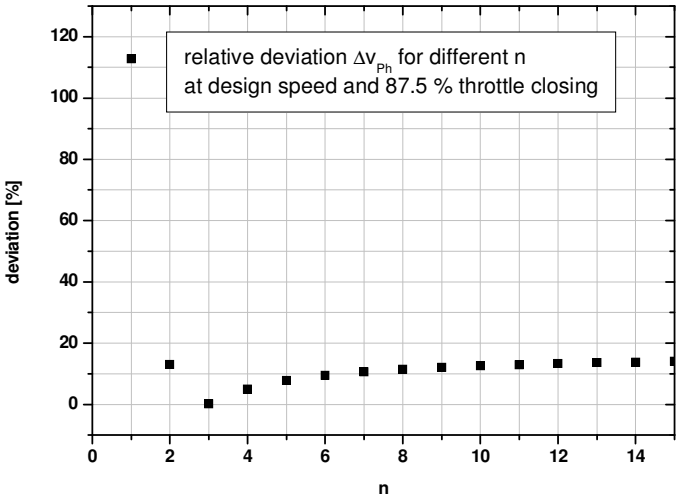

FIG. 13 ESTIMATE OF PHASE VELOCITY BY MINIMIZING ΔV_{PH}

8.2. Helmholtz resonance at outlet throttle

It is shown in Fig. 11 that the peak amplitudes of the acoustic resonance were measured in the middle of the compressor and not at its outlet. Hence, it is unlikely that the origin for the pressure fluctuation inside the compressor comes from outside. Nevertheless, a Helmholtz resonance in the plenum between the compressor outlet and the throttle (marked as green area in Fig. 14) as reason for the acoustic resonance is examined here.

The plenum in the present compressor is sufficiently small to avoid a surge during rotating stall tests. When the throttle is nearly closed, the expansion of fluid is a strong source of excitation and as we will see later, the frequency of the acoustic resonance increases with the throttle position. An approximation for the resonance frequency of a Helmholtz resonator is given by

$$f_H = \frac{a}{2\pi}\sqrt{\frac{A}{VL}} \tag{33}$$

where a is the speed of sound, A is the outlet area of the throttle, L is the length of the throttle duct, and V is the volume of the plenum between the throttle and the compressor outlet. Because the plenum and the throttle do not look like a classic bottle neck there are some uncertainties in the estimation of these values. The volume V is about 0.02m³ consisting of V_1 (compressor outlet), V_2 (diffusor), and V_3 (throttle) as marked in Fig. 14. The outlet area of the throttle is A=0.00092·(100-x) m^2 where x is the throttle position in %. Most uncertainties are in the estimation of the duct length of the throttle. As the fixed and moving side of the throttle has a circular shape (see Fig. 14), it is assumed that the duct length is a part of the circumference of the outlet shape of the throttle as shown in Fig. 14. For the open throttle this is probably an over prediction but for the nearly closed throttle (88%), where the resonance occurs, it is a good assumption. So we use a value of L=36 mm for our calculation. The speed of sound at the compressor outlet at maximum outlet pressure is about a=400m/s. This leads to a Helmholtz resonance frequency f_H for the compressor outlet and throttle of 248 Hz. This is far below the measured frequencies above 1200 Hz. So even with the uncertainties of this approximation a Helmholtz resonance at the compressor outlet could be excluded as reason for the acoustic resonance.

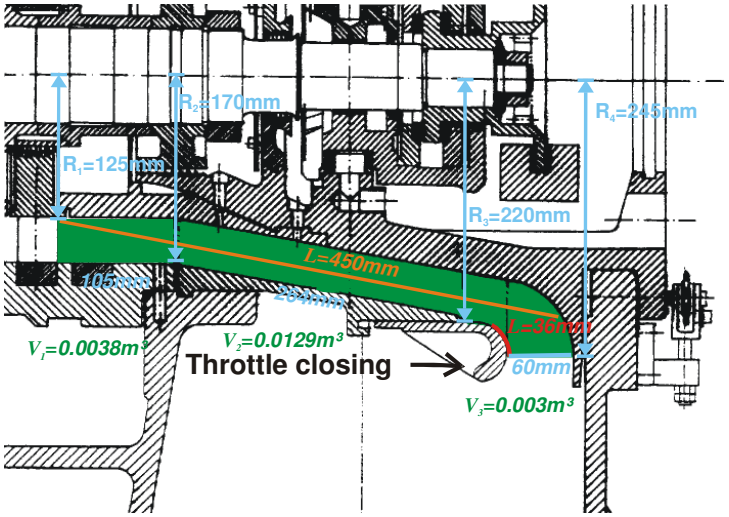

FIG. 14 DETAIL OF COMPRESSOR SKETCH

For the estimation of longitudinal modes of the plenum the acoustic impedance of the throttle and stator rows at the compressor outlet have to be known but a rough estimation with the assumption that the axial length of the plenum l≈450 mm equals half a wave length of the longitudinal mode λ the resonance frequency f_{Res} is given by:

$$f_{Res} = \frac{a}{\lambda} = \frac{a}{2l} \tag{34}$$

For an axial length l≈450 mm and a speed of sound a≈400 m/s the resonance frequency is about 445 Hz. This is also far below the measured resonance frequency of approximately 1550 Hz. Azimuthal modes of the annulus (compressor and plenum) will be treated in the following chapters.

8.3. Vibration induced blade cracks

During maintenance work in 2007, cracked blades were found in the inlet guided vanes (IGV) of the compressor (see Fig. 15 for an example of a cracked blade). This was an unexpected finding, because the compressor ran at most a couple of weeks a year and the age of the blades was about 10 years. Under normal operation conditions, the aerodynamic and mechanical loading of the IGV is low due to the low deflection of the flow in the IGV. The main source of vibration is the interaction with the downstream rotor as long as no acoustic resonance or rotating stall creates additional sources of excitation. To find the cause for the cracks, a numerical and experimental Eigen frequency analysis was done by the IDS (Institut für Dynamik und Schwingungen) at the Leibnitz University of Hannover. It turned out that the vibration modes with high stress levels in the region of the crack had natural frequencies close to the first and second harmonic of the acoustic resonance (Siewert (2007)).
In short, the normally rather modestly stressed blade row in the compressor showed cracked blades and the natural frequency of the blades fits to the fundamental frequency of the acoustic resonance. This made it more likely than not that the pressure fluctuations of the acoustic resonance were causing the blade cracks.

With accelerometers the vibration of the compressor casing above the front bearing were measured simultaneously to the pressure fluctuations. A comparison of vibration and pressure fluctuation measured behind the IGV is shown in Fig. 16. The vibration was measured in axial direction. The acoustic resonance excites vibrations of the compressor structure. The pressure fluctuations and the impact sound are highly correlated at the frequency of the acoustic resonance. However, there are also correlated vibrations beside this frequency in the frequency range from 1100 Hz to 1700 Hz. At 1370 Hz there is a peak in the impact sound signal which is not correlated with the pressure signal. As its level is increasing with the load, it must be excited by the flow. This might be the vibration of an already cracked blade at a natural frequency that is reduced due to the crack.

mode	**set 1**		**set 2**	
	aluminium	**steel**	**aluminium**	**steel**
1	1604.2 Hz	1605.9 Hz	1641.2 Hz	1642.7 Hz
2	3509.2 Hz	3512.5 Hz	3540.6 Hz	3543.9 Hz
3	4162.0 Hz	4165.9 Hz	4211.0 Hz	4214.9 Hz
4	7136.2 Hz	7142.8 Hz	7188.2 Hz	7194.9 Hz
5	7798.2 Hz	7805.5 Hz	7893.5 Hz	7900.8 Hz
6	8502.1 Hz	8510.0 Hz	10754.5 Hz	10764.5 Hz

TABLE 4 CALCULATED NATURAL FREQ. OF THE IGV BLADES (SIEWERT (2007))

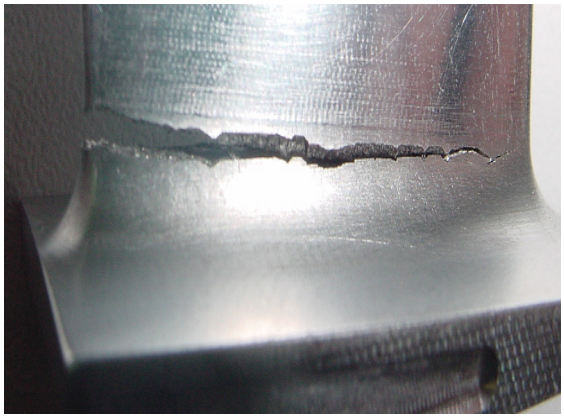

Left : Cracked blade

Middle: FE Model result of strain in z-direction at 1604 Hz

Bottom: measured impulse response with frequency spectrum

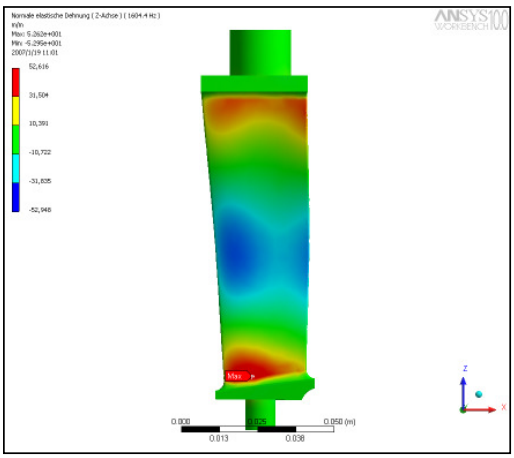

- **FE model → model properties**
- Material properties aluminum:
  - Elastic modulus E = 0.7E11 N/m^2
  - Poisson's number ν = 0.3
  - density ρ = 2.7E3 kg/m^3
- ANSYS WB tetrahedron mesh
  - 13922 SOLID187-elements
  - 25339 knots
- Modal analysis (Block-Lanczos)

Christian Siewert

Institut für Dynamik und Schwingungen
Leibniz Universität Hannover

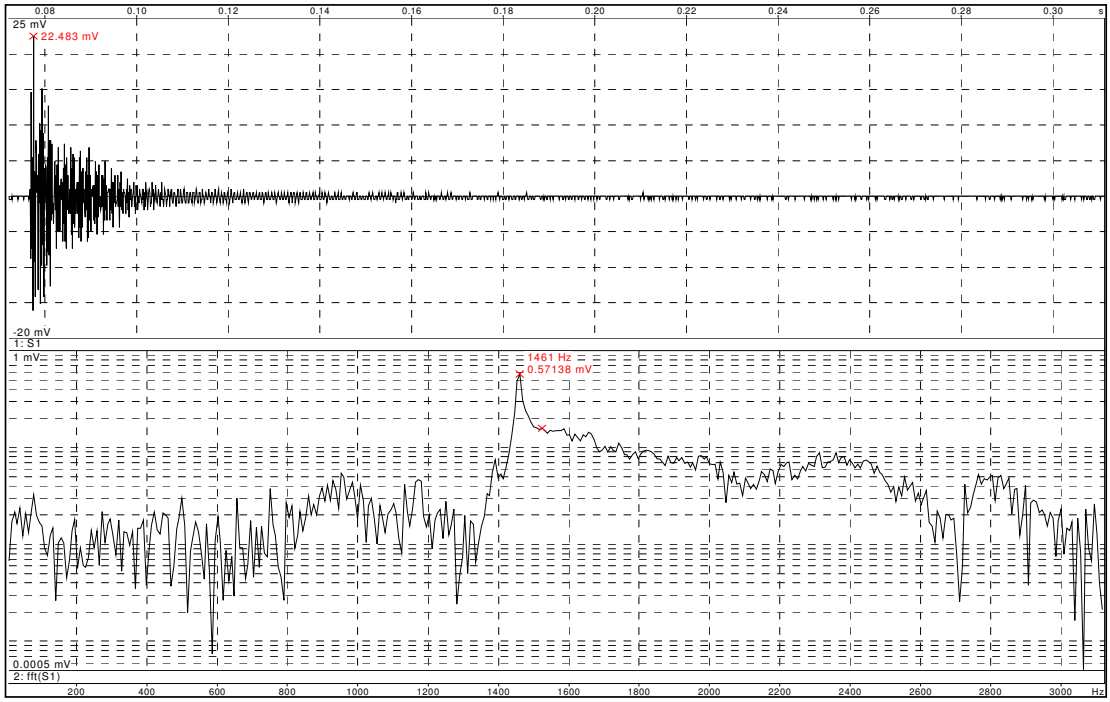

FIG. 15 RESULTS OF NUMERICAL AND EXPERIMENTAL MODAL ANALSYSIS OF CRACKED BLADE

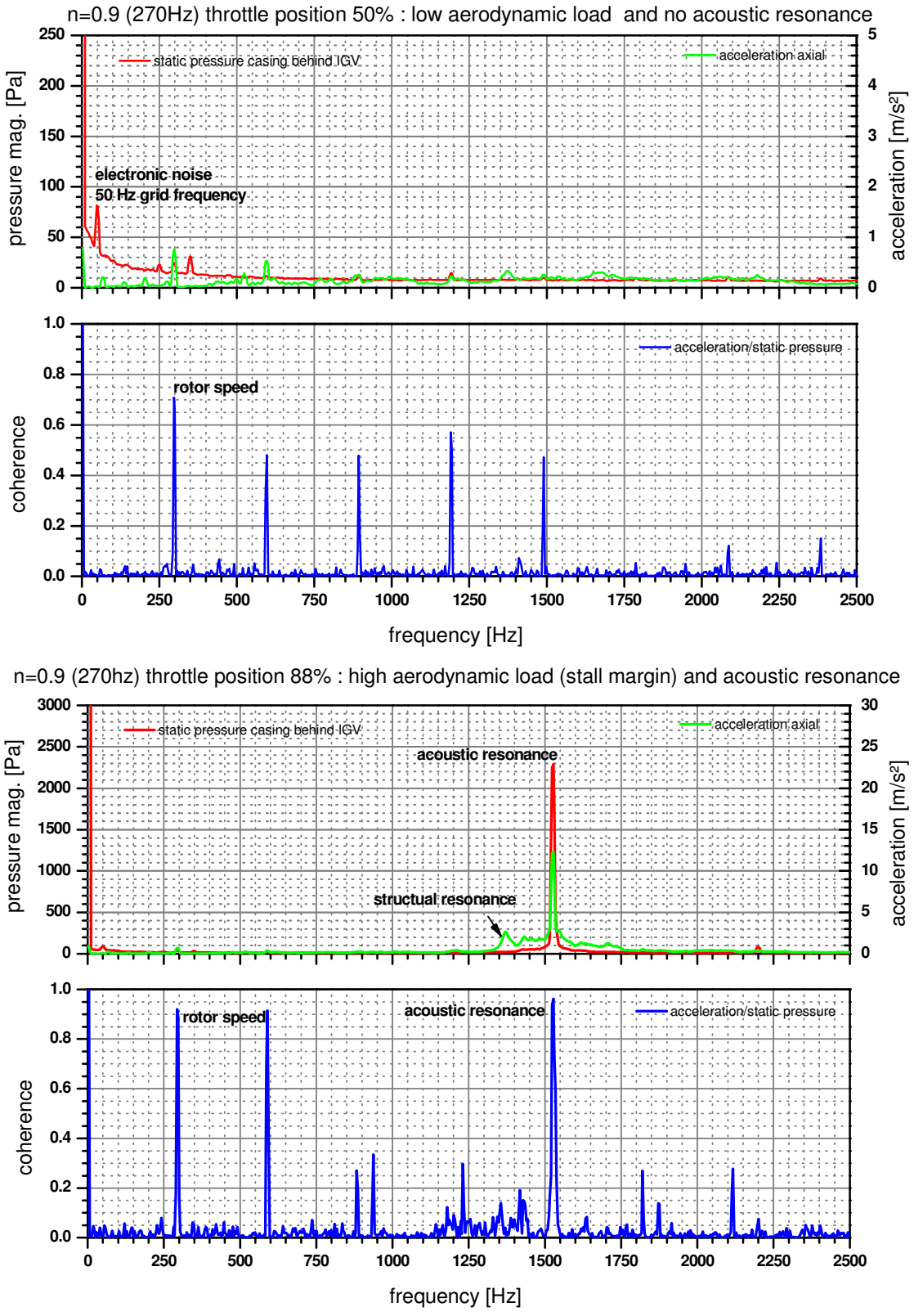

FIG. 16 IMPACT SOUND INDUCED BY PRESSURE FLUCTUATIONS

9. Theoretical Prediction of resonant modes

To support the thesis that the measured pressure fluctuations are an acoustic resonance, it needs to be shown how the compressor annulus with the embedded cascades operates as a resonator. In general this is a difficult task, since there is more than one mechanism working in a turbo compressor that can lead to acoustic resonances. In the present case, this task is less complicated, because it is sufficient that the conditions for one of all the possible mechanisms that lead to acoustic resonances are satisfied in the compressor when the resonance occurs.
Up to now, unsteady CFD calculations of two or more complete stages in the required time resolution are pushing even state of the art computer systems to their limits. So, in most cases the fact is used that the influence of the flow on the acoustic field is stronger than vice versa and the problem is broken down into two tasks. The mean flow is measured or calculated with steady CFD and the results are used as a boundary condition for an acoustic analysis.
If the mean flow is known, the major problems for the prediction of resonant modes of a compressor are: Firstly, that they must take into account the reflection and transmission of the acoustic waves at the blade rows, and secondly the non-uniform flow, especially the swirl. Moreover, also if it is possible to find a solution for those problems, the prediction of the noise sources is still unsolved and the interaction of the resonant field with the source remains as an unsolved problem.

9.1. Effect of blade rows

For acoustic waves with wavelengths of the same order as the dimension of the compressor, resonances can occur and the transmission and reflection of acoustic waves is strongly dependent on frequency.

Since the 1960's several researchers have attempted to solve these problems theoretically. The following short review is not aiming at elaborating the subject further, but rather at focussing on those results useful for the explanation of the acoustic resonance in the Hannover compressor.
After Tyler and Sofrin (1962) showed that acoustic modes can propagate in a compressor due to rotor-stator interaction, the question how these modes propagate through a blade row became important. Mani and Horvay (1970) used the Wiener-Hopf technique with simplified unloaded blades for the solution of this problem. Kaji and Okazaki (1970) used an even simpler actuator disc approach to determine the transmission and reflection coefficients of helical modes. Because this method delivers no information about the effect of different blade spacing, they provide a sophisticated theory in the second part of their paper. They showed that under certain conditions when the ratio of blade spacing to wave length of acoustic wave increases over the critical values, the sound field becomes "super resonant", because the waves are trapped between the blades. This is similar to a "Parker resonance".
According to Kajis and Okazakis (1970) calculations, super resonances can occur when the product of wave number and blade spacing is lower than 2π. This is roughly

the case when the circumferential mode number m is close to the number of blades or higher.

The authors show further that under a certain incidence angle and blade spacing, the incident and reflected acoustic field form a new resonant acoustic mode. It is one important finding that this mode in most cases has a different number of lobes around the circumference than the incident wave (mode scattering). However, this takes place only when the number of lobes comes close to the number of blades in a row.

Because the circumferential mode of the acoustic resonance observed in the present compressor is far less than the number blades in each row, no super resonance or mode scattering has to be taken in account. This means for our purposes that the result of the simple actuator disc approach may be used. Here the frequency of the acoustic wave only exerts influence on the phase shift between transmitted and reflected wave, not on the transmission or reflection coefficient.

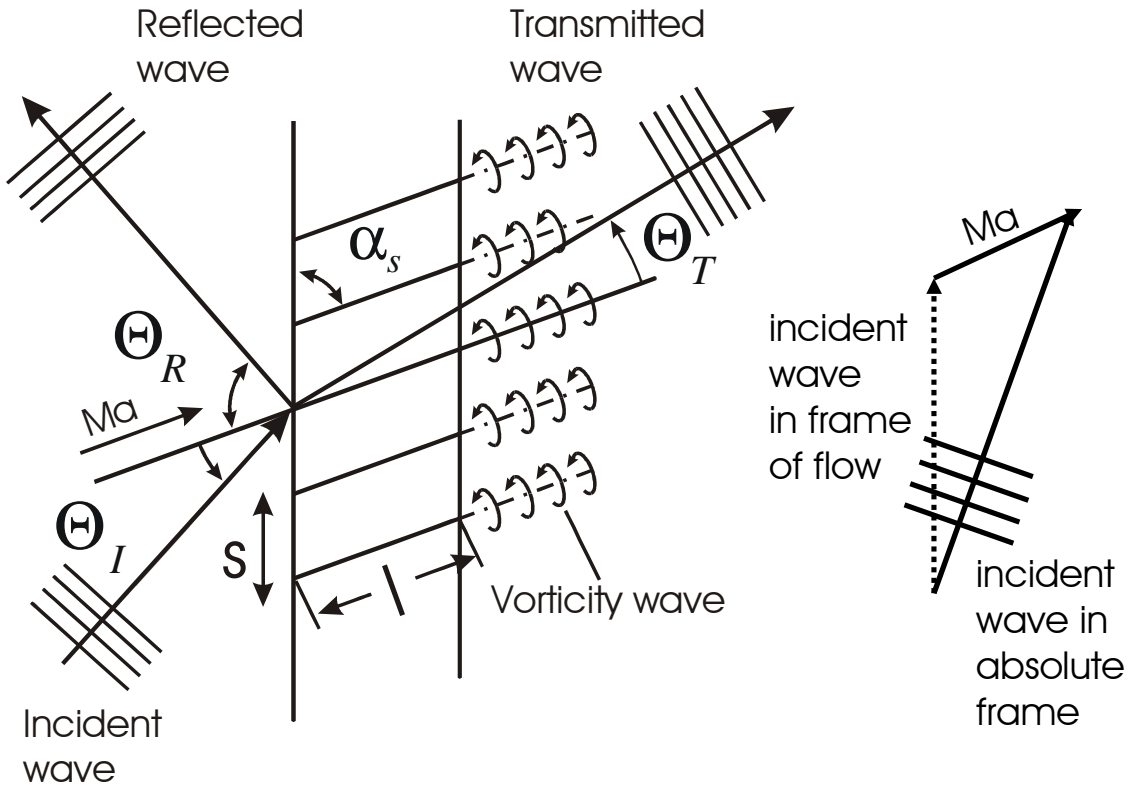

FIG. 17 SCHEMA OF WAVE SCATTERING AT A BLADE ROW WITH NON ZERO MEAN FLOW (KOCH (1971))

For the calculation of those coefficients, all authors used a model comparable to Fig. 17. This means they used plane plates as model for the blades and a mean flow in direction of the blades. So, blade loading remains unaccounted for, but Kaji and Okazaki (1970) have shown that the effect of blade loading for most incidence angles has little significance. The incidence angle they used in their model is given in the frame of the flow. To compare them with measured angles in a fixed frame, the measured incidence angles must be corrected by the effect of the mean flow. This can be done by a vector addition of the flow and sound field.

Apart from the incidence angle, the transmission and reflection coefficient depend on the stagger angle α_s of the blade row, the blade length l, the circumferential spacing s, and the Mach number of the mean flow Ma. Koch (1971) calculated the transmission and reflection coefficients in Fig. 18 for different Mach numbers, a stagger angle of α_s=30°, a ratio s/l=1, and s=1. For a wide range of incidence angles θ_I, an acoustic wave impinging on a blade row is partly reflected, partly transmitted, and partly dissipated. This is marked as zone 2 in Fig. 18. At the right border of zone 2, the incidence angle is zero or 180° and the acoustic wave fronts are normal to the blades, so they can penetrate the cascade without any resistance. This means the reflection coefficient is zero. This is marked by a T between the diagrams in Fig. 18. An angle of 180° means that the wave is penetrating the cascade from the backside. Because the propagation of the wave fronts is parallel to the mean flow, the point T is independent from the Mach number of the mean flow.

If there is no mean flow (Ma=0) and the incidence angle of the acoustic wave equals the stagger angle, the wave fronts are propagating parallel to the cascade and the cascade is not penetrated by the waves. Hence, no transmission takes place and the reflection coefficient is one even if no reflection takes place as well. For the case of a non-zero mean flow (Ma≠0), there is also an incidence angle in the frame of the flow where the waves do not penetrate the cascade. This is because the wave fronts are propagating parallel to the cascade in the frame of the blade row. This incidence angle is given by:

$$Ma_z = -\sin(\theta - \alpha_s) \text{ for upstream traveling waves with swirl and}$$
$$Ma_z = \sin(\theta + \alpha_s) \text{ for upstream traveling waves against swirl} \qquad (35)$$

Again, for this incidence angle the reflection coefficient is one and the transmission coefficient is zero. The incidence angles are marked with an R in Fig. 18. It should be noted that for this incidence angle the wave fronts are parallel to the machine axis in the fixed frame, while at cut off condition which will be discussed later in subsection 9.4, the wave fronts are parallel to the machine axis in the frame of the flow.

Another outstanding case with no reflection is given at a particular angle of incidence, when the sound waves reflected by each blade of the cascade cancel out each other to result in zero intensity as a whole. These angles of destructive superposition are marked with a D between the diagrams in Fig. 18. Due to this superposition, energy is dissipating and so the transmission coefficient delivered by the model is not one. Kaji and Okazaki (1970) formulated the following condition for the estimation of this particular angle of incidence if the stagger angle α_s is between 0° and 90°:

$$\sin(\theta - \alpha_s) - \sin(\alpha_s) - Ma \cdot \sin(\alpha_s) \cdot (1 + \cos(\theta)) = 0$$
for upstream traveling waves and
$$\sin(\theta - \alpha_s) + \sin(\alpha_s) - Ma \cdot \sin(\alpha_s) \cdot (1 - \cos(\theta)) = 0 \qquad (36)$$
for downstream traveling waves

If the stagger angle is more than 90°, as it is for the rotor blades, the sketch in Fig. 17 must be mirrored at a horizontal line and the definition of the angles must be taken from the mirrored sketch.

Consequently, the diagram in Fig. 18 was separated in four zones. The borders are defined by those incidence angles where the reflection is zero. In zone 2 the acoustic wave is travelling upstream and entering the blade row from the backside. In zone 4 the acoustic wave is travelling downstream and entering the blade row from the front. Zone 1 and 3 are around those angles where the acoustic waves travelling parallel to the blade row with (zone 1) or against the swirl (zone 3).

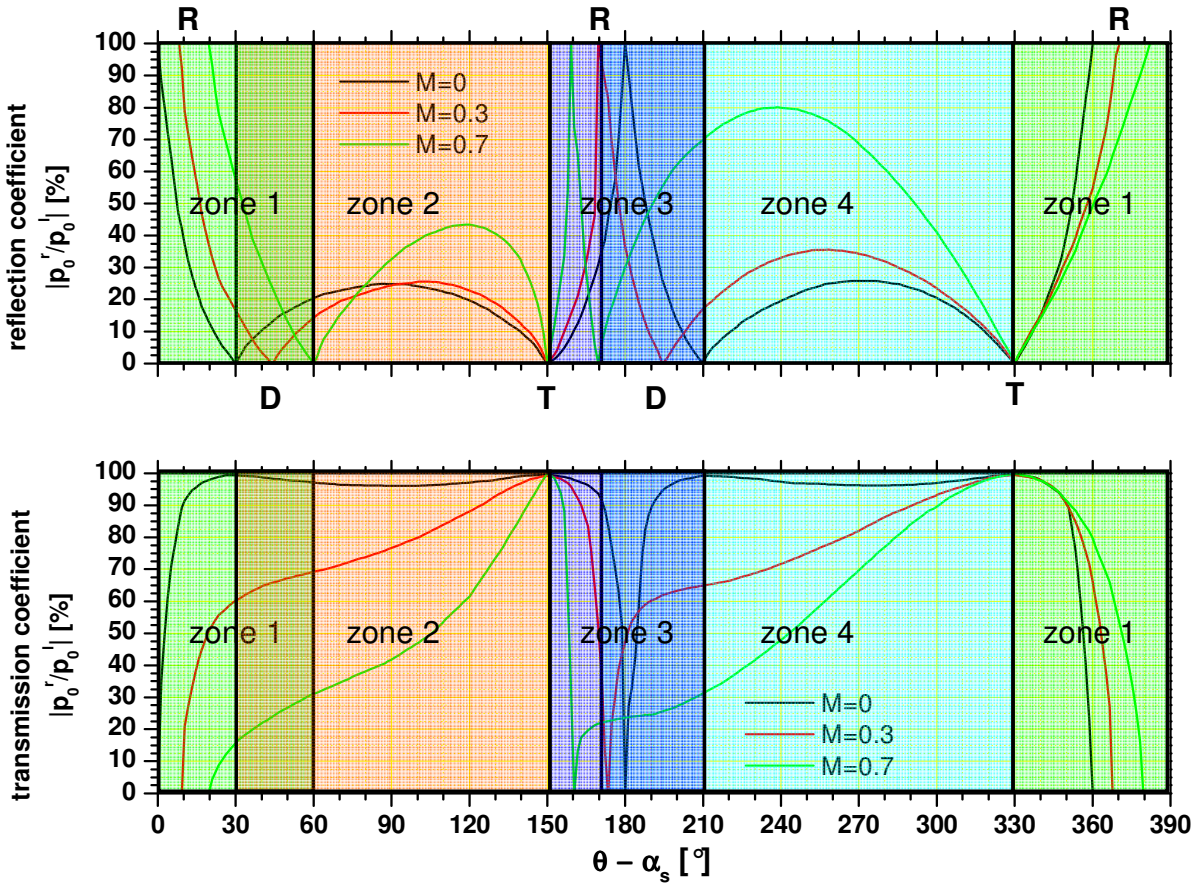

FIG. 18 EXAMPLE OF TRANSMISSION AND REFLECTION COEFFICIENT FOR SUB-RESONANT CASE AND α_s = 30° (SEE REF. KOCH (1971) FIG. 2)

9.2. Effect of non-uniform flow and geometry

From simple three-dimensional acoustics of ducts, it is known that the mode shape of an acoustic field depends on the hub ratio. This will be explained later more in detail. In addition to this effect, Tam (1971) found in an early paper that helical acoustic modes are significantly scattered back in a throat behind a cylindrical duct, if the flow Mach number exceeds 0.4.

While the above researchers have limited their work to non-swirling flow, Kerrebrock (1977) has shown that for swirling flow, where vortices, pressure, and entropy fields are not independent anymore, that the influence of the swirling base flow on high frequency pressure oscillations is weak. This means that for modes with frequencies far above the rotor speed, only the general condition of acoustic cut-off needs to be considered.

The first approach for the calculation of sound transmission through a duct with swirling flow and blade rows was suggested by Heinig (1983) in conjunction with a calculation method for the reflection and transmission of the blades provided by Koch (1971). Koch's model was an enhancement of Mani's and Horway's (1970) model. Heinig divided the annulus in small discs in axial direction and assumed a constant flow and constant hub-to-tip ratio in each disc. Mathematically, each disc is presented by a simple four-pole matrix. Then the propagation of sound in the whole machine is estimated by a simple matrix multiplication. A limitation of this model is that mode scattering is unaccounted for. However, Heinig showed that mode scattering mainly occurs for waves with circumferential wavelengths of two blade pitches or less. For larger wavelengths, his model is valid. Vortex waves are ignored by the model, too.

Evans et al. show in Evans et al. (1994) that trapped modes exist in a 2D waveguide that contains asymmetric obstruction about the centreline. Other more recent models for acoustic resonances in turbomachinery were presented by Peake and co-workers in a set of papers (see Cooper and Peake (2000) for example), by Duan and McIver (2004) and by Atassi et al. (2004). In Cooper and Peake (2000), Cooper and Peake showed for an aero-engine intake that "turning points" of acoustic modes (points of high or total reflection in axial direction) can be caused by the varying duct cross-section as well as by the blade rows. They found that a third cause for turning points of a mode is the change from cut-on to cut-off condition due to the swirl. This has also been shown by Rienstra (1999) and Ovenden et al. (2004). The latter also found that the phase of the reflected mode is shifted by $\pi/2$. The cut-off effect is explained in the Section 9.4.

9.3. Summary of theoretical prediction methods

With a focus on the explanation of the acoustic resonance in the Hannover test rig, this literature review can be summarized as follows:

- Blade rows work as reflectors for acoustic waves when the incident wave hits the blade under a high positive or negative incidence angle.
- Modes with wavelengths of the magnitude of the blade pitch could be trapped if the wave fronts are parallel to the blades (super resonance).
- Blade rows are shifting the phase between reflected and transmitted wave.
- For high frequencies, the swirl must be considered only for cut-off conditions.
- Mode scattering takes place mainly for wavelengths of the magnitude of the blade pitch.
- Change from cut-on to cut-off turns the waves with a phase shift of $\pi/2$.
- Variation in the duct cross-section can also lead to turning points.

9.4. Simplified model

Based on the results of the last section, a simple mathematical model will explain the acoustic resonance of the compressor. This is possible because the number of lobes of the pressure field is much lower than the number of blades. Therefore mode scattering will not occur. Mode trapping between the blades (Parker resonances) can be neglected from our model for the same reason. Because the frequency is five times higher than the rotor speed, the swirl will be considered only for the estimation of cut-on/off conditions. The variation of the cross section will be considered in the model only for the estimation of the cut-on/off condition. The flow is assumed to be uniform in radial direction.

For a hard-walled annulus with constant inner and outer diameter along the z-axis, the pressure field is given by Eq. (37) which is taken from Ghiladi (1981). The equation is stated in cylindrical co-ordinates with radius r, circumferential angle φ, and z as axial co-ordinate. The constants B are the amplitudes of the sub modes ω is the angular frequency and k is the wave number. As long as there is no flow in the annulus, k_z is independent from the direction of propagation. In contrast, in the presence of a swirling mean flow k_z is different for the propagation with and against the flow in axial and circumferential direction.

$$p_{m,n}(r,\varphi,z,t) = f(k_{r,m,n}r) \cdot \left(B_{++}\exp(im\varphi + ik_{+\varphi,+z}z) + B_{-+}\exp(-im\varphi - ik_{-\varphi,+z}z) + B_{+-}\exp(im\varphi + ik_{+\varphi,-z}z) + B_{--}\exp(-im\varphi - ik_{-\varphi,-z}z)\right) \cdot \exp(-i\omega t) \quad (37)$$

The function $f(k_{r,m,n}r)$ contains the pressure distribution in the r-φ-plane. Even without knowing $f(k_{r,m,n}r)$ in Eq. (37), the harmonic function indicates that the sound field has a helical structure which spins in the annulus. Each azimuthal mode has four sub-modes depending on the propagation direction of the mode relative to the mean flow.

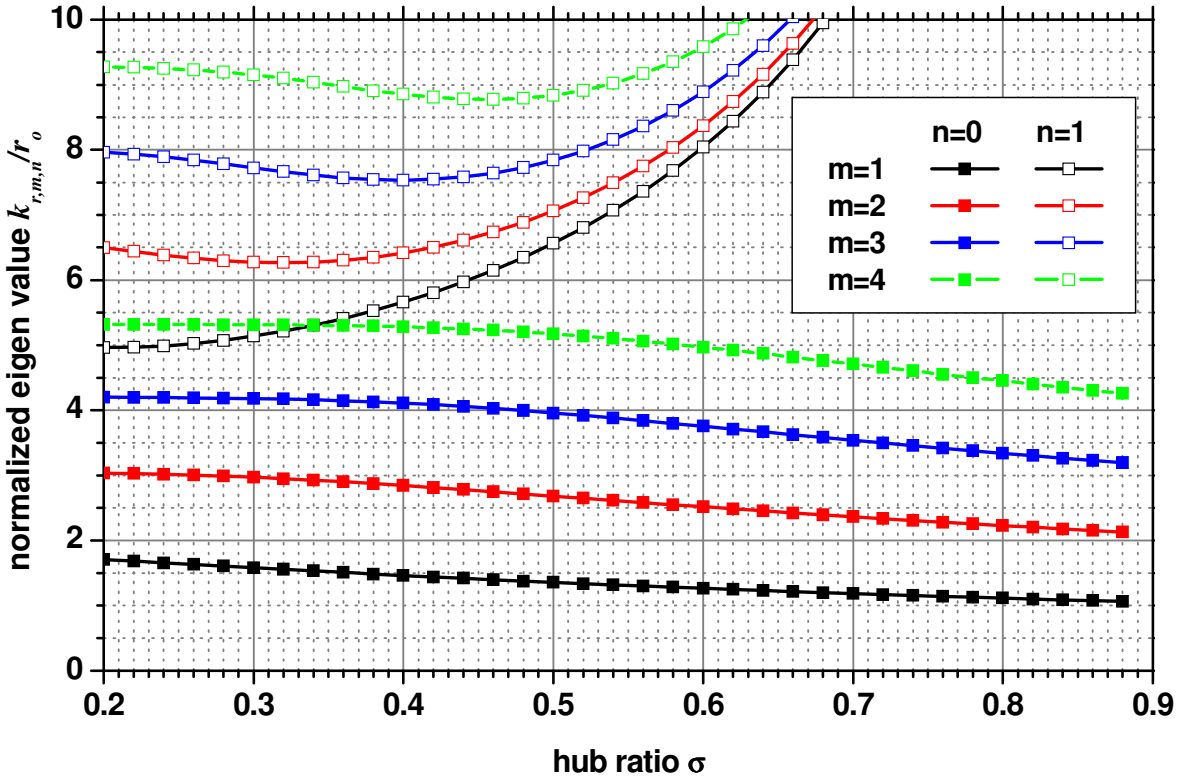

FIG. 19 CALCULATED EIGENVALUES $K_{R,M,N}$ NORMALIZED TO OUTER RADIUS OVER HUB RATIO

The Eigenvalues $k_{r,m,n}$ depend on the hub ratio $\sigma = r_i / r_a$ of inner to outer radius of the annulus and the number of periods of the mode along the circumference (m) and radius (n). $k_{r,m,n}$ is the nth zero of equation (38) (Ghiladi (1981)).

$$\begin{aligned}&\left(J_{m-1}\left(k_r r_a r_i\right)-J_{m+1}\left(k_r r_a r_i\right)\right)\cdot\\&\left(Y_{m-1}\left(k_r r_a\right)-Y_{m+1}\left(k_r r_a\right)\right)-\\&\left(J_{m-1}\left(k_r r_a\right)-J_{m+1}\left(k_r r_a\right)\right)\cdot\\&\left(Y_{m-1}\left(k_r r_a r_i\right)-Y_{m+1}\left(k_r r_a r_i\right)\right)=0\end{aligned} \tag{38}$$

J_i and Y_i are ith order Bessel functions of first and second kind. In Fig. 19 there are the Eigen values of some modes plotted against the hub ratio for typical hub ratios of turbomachinery.

The radial pressure distribution $f(k_{r,m,n}r)$ is given by

$$f\left(k_{r,m,n}r\right)=J_m\left(k_{r,m,n}r\right)-Q_{m,n}Y_m\left(k_{r,m,n}r\right) \text{ with}$$

$$Q_{m,n}=\frac{J_{m+1}\left(k_{r,m,n}r_a\right)-J_{m-1}\left(k_{r,m,n}r_a\right)}{Y_{m-1}\left(k_{r,m,n}r_a\right)-Y_{m+1}\left(k_{r,m,n}r_a\right)} \tag{39}$$

The axial wave number k_z depends on the flow in the annulus and the Eigenvalue $k_{r,m,n}$. For the assumption that the mean flow could be treated as a rigid body, k_z is given by Lohmann (1978):

$$k_{\pm\varphi,\pm z}=\frac{\mp Ma_z\left(k\pm Ma_\varphi k_{r,m.n}\right)}{1-Ma_z^2}+\frac{\sqrt{\left(k\pm Ma_\varphi k_{r,m.n}\right)^2-\left(1-Ma_z^2\right)k_{r,m,n}^2}}{1-Ma_z^2} \tag{40}$$

Ma_z and Ma_φ are the axial and circumferential Mach number of the flow and

$$k=2\pi/\lambda=2\pi f/a \tag{41}$$

is the wave number of a free acoustic wave. The sign in front of the circumferential Mach number Ma_φ depends on the direction of the spin. A positive sign indicates that the mode spins with the flow and a negative sign that it spins against it. It corresponds to the sign in front of φ in the index of $k_{\varphi,z}$. The sign in front of the z in the index of $k_{\varphi,z}$ is always opposite to the sign in front of Ma_z. A positive sign in the index of $k_{\varphi,z}$ means propagation in direction of the flow and a negative against it. Because $k_{r,m,n}$ depends on the hub ratio, the axial wave number changes with the annulus cross-sectional area as shown in Fig. 19. If the hub ratio of an annulus is increasing along its axis, like it is in a compressor, a mode with a given frequency can change from cut-on to cut-off and vice versa at a certain point in the compressor.

The frequency where the root in equation (40) becomes zero is called cut-off frequency and is given by equation (42).

$$f_{m,n}^{cut}=\frac{ak_{r,m.n}}{2\pi}\left(\sqrt{1-Ma_z^2}\mp Ma_\varphi\right) \tag{42}$$

For a duct without any flow, the cut-off condition is given by $k=k_{r,m,n}$. In this case, k_z is

$$k_z = \sqrt{k^2 - k_{r,m.n}^2} \ , \ k_z^{cut} = 0 \tag{43}$$

and the acoustic field becomes uniform in z-direction. The wave fronts of the field are spinning parallel to the duct axis and no acoustic energy is transported in z-direction. This is the physical meaning of cut off. The same applies to a mode in a duct with flow. However, in this case the acoustic field in the fixed frame of reference is not uniform in z-direction anymore. The cut-off frequencies for modes spinning against swirl are higher than for those spinning with the flow. This means, by increasing the swirl in a duct, modes with a fixed frequency like the blade passing frequency could be cut off if they spin against the flow and could be cut on if they spin with the flow. At cut-off frequency, the wave fronts again are running parallel to the machine axis in the frame of the flow, so in difference to the case of no mean flow, the axial wave number at cut-off conditions in the fixed frame is not zero.

If the frequency matches the cut-off frequency $k_{-z} = -k_{+z}$, the modes that are cut off have a pressure field given by:

$$\begin{aligned} p_{m,n}^{cutoff}(r,\varphi,z,t) = & f\left(k_{r,m,n} r\right) \\ & \cdot \left(B_{\pm+} + B_{\pm-}\right) \exp\left(\pm i m \varphi\right) \\ & \cdot \exp\left(-i k_{z,\pm\varphi} z\right) \\ & \cdot \exp\left(-i \omega t\right) \end{aligned} \tag{44}$$

In Fig. 20, the acoustic field of a (3,1) mode with three lobes around the circumference and one in radial direction is shown. The sketches of time series in Fig. 20 show the signal of virtual pressure transducers in the acoustic field. The field has high (red) and low (green) pressure areas that form wave fronts with a helix structure. These wave fronts are moving perpendicular to the helix as shown by the black arrow in Fig. 20. The incidence angle $\beta_\pm$ of the wave fronts to the blade rows is measured from the machine axis and in Koch's definition in Fig. 17 it is given by Eq. (45). The velocity triangles and wave incidence will be explained in detail in Section 10.4. See also Fig. 28 on page 59 for more details.

$$\begin{aligned} \beta_\pm &= \arctan\left(\frac{\lambda_\varphi}{\lambda_{\pm z}}\right) = \arctan\left(\frac{r k_{\pm z}}{m}\right) \text{ or} \\ \theta_I - \alpha_s &= \arctan\left(\frac{m}{r k_{\pm z}}\right) \end{aligned} \tag{45}$$

In general the amplitudes $B_{\pm\pm}$ in equation (37) have different values. For the special case when the amplitudes of different modes are the same we can take advantage of the formula

$$\exp(ix)+\exp(iy)=\cos\left(\frac{x-y}{2}\right)\exp\left(i\frac{x+y}{2}\right) \tag{46}$$

Then equation (37) is simplified to

$$\begin{aligned}
&p_{m,n}(r,\varphi,z,t)=f(k_{r,m,n}r)\\
&\cdot\left(B_{-z}\cos\left(m\varphi+\frac{\Delta\varphi_-}{2}+\frac{k_{-\varphi,-z}-k_{+\varphi,-z}}{2}z\right)\exp\left(-i\frac{\Delta\varphi_-}{2}-i\frac{k_{+\varphi,-z}+k_{-\varphi,-z}}{2}z\right)\right.\\
&\left.+B_{+z}\cos\left(m\varphi+\frac{\Delta\varphi_+}{2}+\frac{k_{+\varphi,+z}-k_{-\varphi,+z}}{2}z\right)\exp\left(-i\frac{\Delta\varphi_+}{2}+i\frac{k_{+\varphi,+z}+k_{-\varphi,+z}}{2}z\right)\right)\\
&\cdot\exp(-i\omega t)
\end{aligned}$$

with $B_{-z}=B_{+-}=B_{--}e^{i\Delta\varphi_-}$ and $B_{+z}=B_{++}=B_{-+}e^{i\Delta\varphi_+}$

or (47)

$$\begin{aligned}
&p_{m,n}(r,\varphi,z,t)=f(k_{r,m,n}r)\\
&\cdot\left(B_{-\varphi}\cos\left(\frac{k_{-\varphi,+z}+k_{-\varphi,-z}}{2}z+\frac{\zeta_-}{2}\right)\exp\left(i\frac{k_{-\varphi,+z}-k_{-\varphi,-z}}{2}z-i\frac{\zeta_-}{2}-im\varphi\right)\right)\\
&+B_{+\varphi}\cos\left(\frac{k_{+\varphi,+z}+k_{+\varphi,-z}}{2}z+\frac{\zeta_+}{2}\right)\exp\left(i\frac{k_{+\varphi,+z}-k_{+\varphi,-z}}{2}z-i\frac{\zeta_+}{2}+im\varphi\right)\Bigg)\\
&\cdot\exp(-i\omega t)
\end{aligned}$$

with $B_{+\varphi}=B_{++}=B_{+-}e^{i\zeta_+}$ and $B_{-\varphi}=B_{-+}=B_{--}e^{i\zeta_-}$

The important issue on equation (47) is that for the case of modes interfering with other modes at the same frequency, the axial and circumferential wavelength of the interference wave is different than those of the single interfering waves. In the case where the amount of the wave numbers of the modes is the same and just the polarity is opposite, the resulting interference wave is a standing wave. This is the case for the circumferential wave number m in (47). The pressure field is only a function of φ in its amplitude and not in its phase anymore. This means that as long as we measure a circumferential phase shift different than zero or 180°, one of the modes spinning with or against the flow has a higher amplitude than the other and/or one mode has a different circumferential wave number than the other.

If the measured phase shift in the first case is positive in the direction of the flow, the mode spinning with the flow is stronger than those spinning against it (and the other way around if the phase shift is negative). Unlike the phase shift in circumferential

direction, the phase shift in axial direction between two signals from different axial positions and the same circumferential position does not have to be zero or 180°, even if the axially interfering waves have the same amplitude.

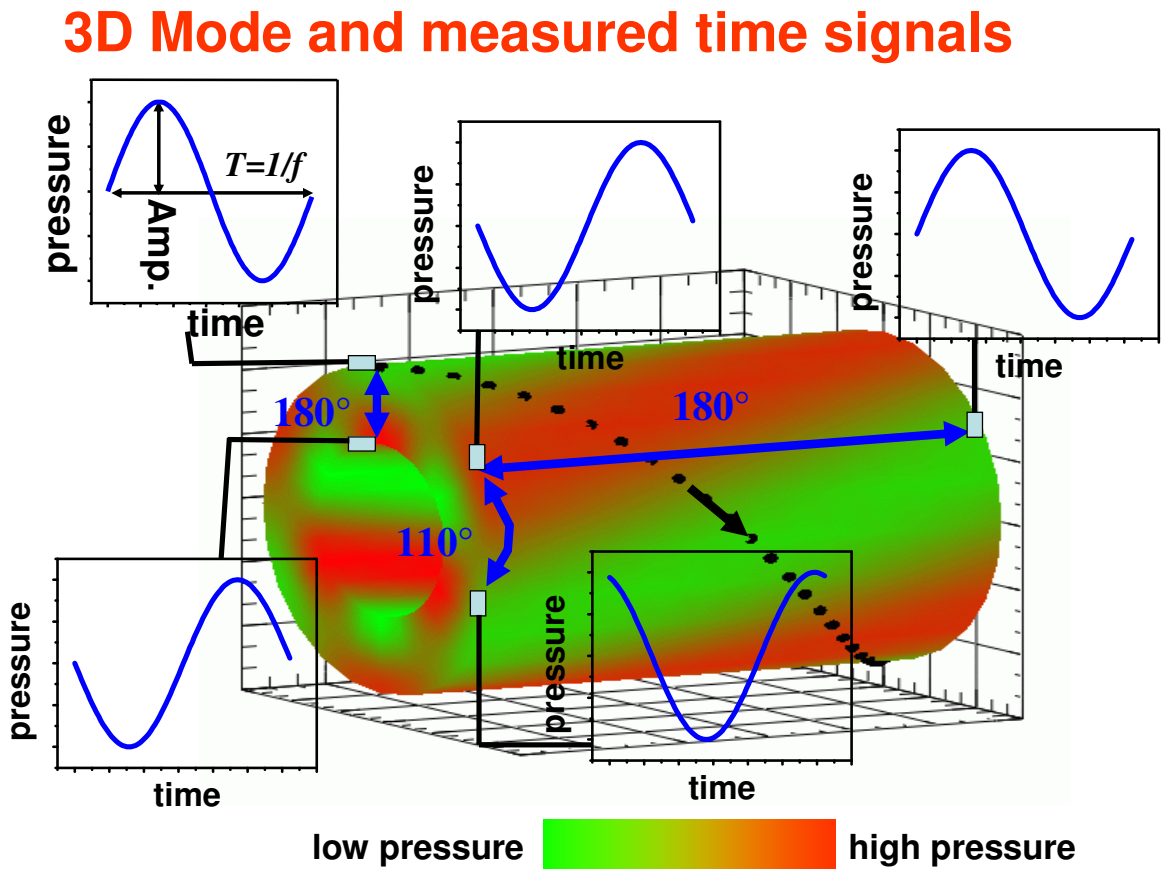

FIG. 20 EXAMPLE OF A (3,1) HELICAL ACOUSTIC MODE WITH TIME SERIES OF PRESSURE SIGNALS

If there are only modes travelling with the swirl ($B_{-\varphi}=0$) or there are only modes travelling against the swirl ($B_{+\varphi}=0$) the phase shift $\Delta\alpha$ of signals from sensors with an axial distance Δz and no circumferential distance is given by:

$$\Delta\alpha = \frac{\Delta z \cdot \left(k_{+z} - k_{-z}\right)}{2} \tag{48}$$

With (40) this becomes

$$\Delta\alpha = -\Delta z \frac{Ma_z\left(k \pm Ma_\varphi k_{r,m.n}\right)}{1 - Ma_z^2} \tag{49}$$

Another important outcome of equation (47) is the amplitude modulation in space. This is, because the amplitude includes a cosine function with an argument that depends on the wave numbers and the independent variable φ and z. This means that there are areas where the interference wave vanishes. This is the case when

$$\varphi_j = \frac{(j+1)\pi + \Delta\varphi}{m} \text{ or}$$

$$z_j = \frac{(j+1)\pi + \zeta}{(k_{+z} + k_{-z})} \text{ with } k_{+z} \neq -k_{-z} \tag{50}$$

$$j = \ldots -2, -1, 0, 1, 2, \ldots$$

The difference between the circumferential standing wave and the axial "standing wave" is the fact, that in axial direction as long as $k_{+z} \neq k_{-z}$, the wave runs between the nodal points. With (40) the fraction $(k_{+z} + k_{-z})/2$ equals

$$\frac{k_{+z} + k_{-z}}{2} = \frac{\sqrt{(k \pm Ma_\varphi k_{r,m.n})^2 - (1 - Ma_z^2) k_{r,m,n}^2}}{1 - Ma_z^2} \tag{51}$$

Such a modulated running wave is illustrated with an example in Fig. 21. The lines in different colors show the amplitude of the interference wave from equation (47) at different times. In the lower diagram, there is a real standing wave not propagating in any direction. In the upper diagram the waves propagate under the envelope shown by the dashed black line. The wave is travelling slowly against the flow marked with the black arrows.

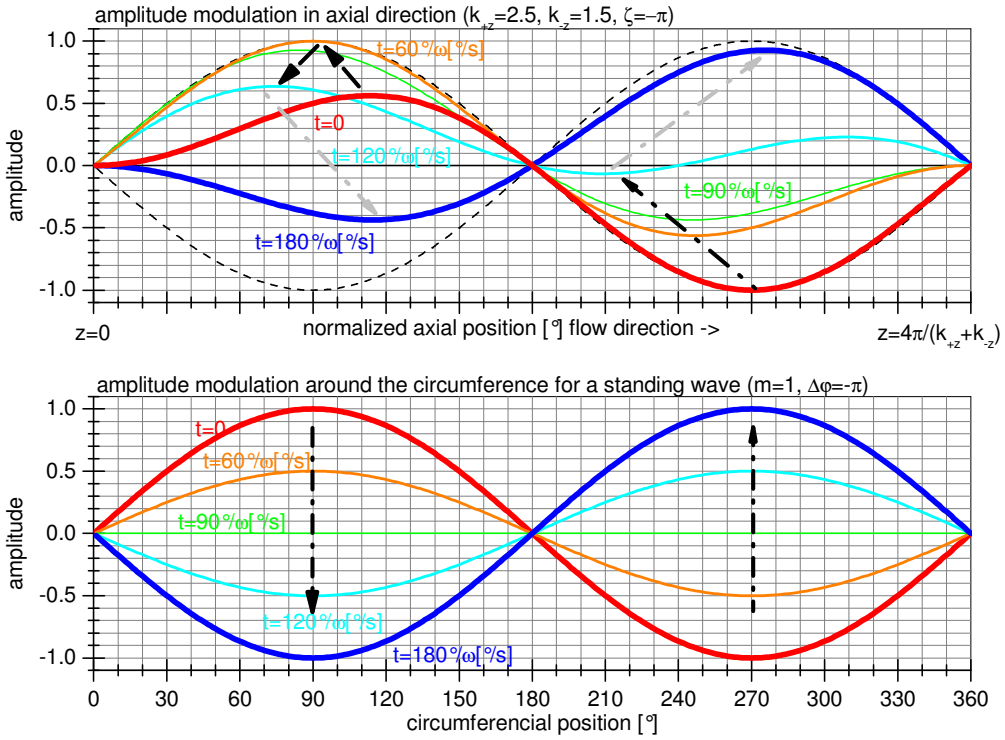

FIG. 21 SCHEMA OF AXIAL AND CIRCUMFERENTIAL INTERFERENCE WAVES

10. Application to Measurements

The contour plot in Fig. 10 in section 8.1 shows the pressure signal of one sensor mounted in the first stage over frequency and time. Simultaneously to this signal, static pressure signals from the other stages were measured together with the pressure signals of a four-hole pneumatic probe. The pressure transducers in the compressor casing were mounted in two axial rows with a circumferential distance of 105°. In each row there was one sensor per stage in front of the rotor and in one row an extra sensor at the compressor outlet behind the last stator. The axial distance of the sensors was 100 mm. A four-hole flow probe with high-frequency pressure sensors was inserted behind the first rotor at mid-span. From these pressure signals, the amplitudes, the frequency, and the axial and circumferential phase shift of the fundamental mode of the acoustic resonance were estimated with a floating FFT analysis. The sampling frequency was 60 kHz and the FFT window length 16384 points. Five windows with an overlap of 50% were used for the analysis. The phase shift was taken at the peak frequency of the acoustic resonance. The results for a measurement at a rotor speed of 0.95 and continuously throttle closing are shown in Fig. 22. As described in Section 8.1, the amplitude of the acoustic resonance have the highest level in the middle stages of the compressor and a decreasing level towards the in- and outlet. The amplitude is growing in all stages when we come closer to the stall margin with the exception of the compressor outlet where the level remains more or less constant after a throttle position exceeds 86.7 %. This amplitude distribution shows that the resonance arises inside the compressor and not outside, because the amplitudes are decreasing at the edges of the compressor.

The circumferential phase shift shows that the measured values are close to 315° (3·105°), which is the theoretical value for a (3,n) mode and a sensor distance of 105°. Because the phase shift is 315° and not -315°, the dominant mode is a mode spinning with the direction of rotation and so with the direction of the flow. It is also seen that the deviation from this theoretical value in the second and third stage is comparatively small while it is higher in the first stage, especially at throttle positions where the resonance starts.

One explanation could be a high statistical error of the phase shifts. However, as it is estimated to be less than 1°, this possibility can be excluded. Further possible reasons could be other circumferential modes with the same or nearly the same frequency or a circumferentially non uniform flow. Non uniform flow could be caused locally by wakes from a stator close to the sensor. Other modes could be caused by mode scattering in reflection processes at the blade rows. Due to the comparable small deviation from the theoretical value the amplitudes of the scattered modes have to be small in our case.

Especially the interference with modes spinning against the swirl is a possible reason for the deviation. We know that the dominating modes are those spinning with the swirl. But there might be modes spinning against the swirl with lower amplitudes, too. In our model, at a fixed axial position z_0 and time t_0, this means that those modes spinning against the flow are forming a standing wave with parts of the modes spinning with the flow as shown by equation (52) which is derived from equation (37).

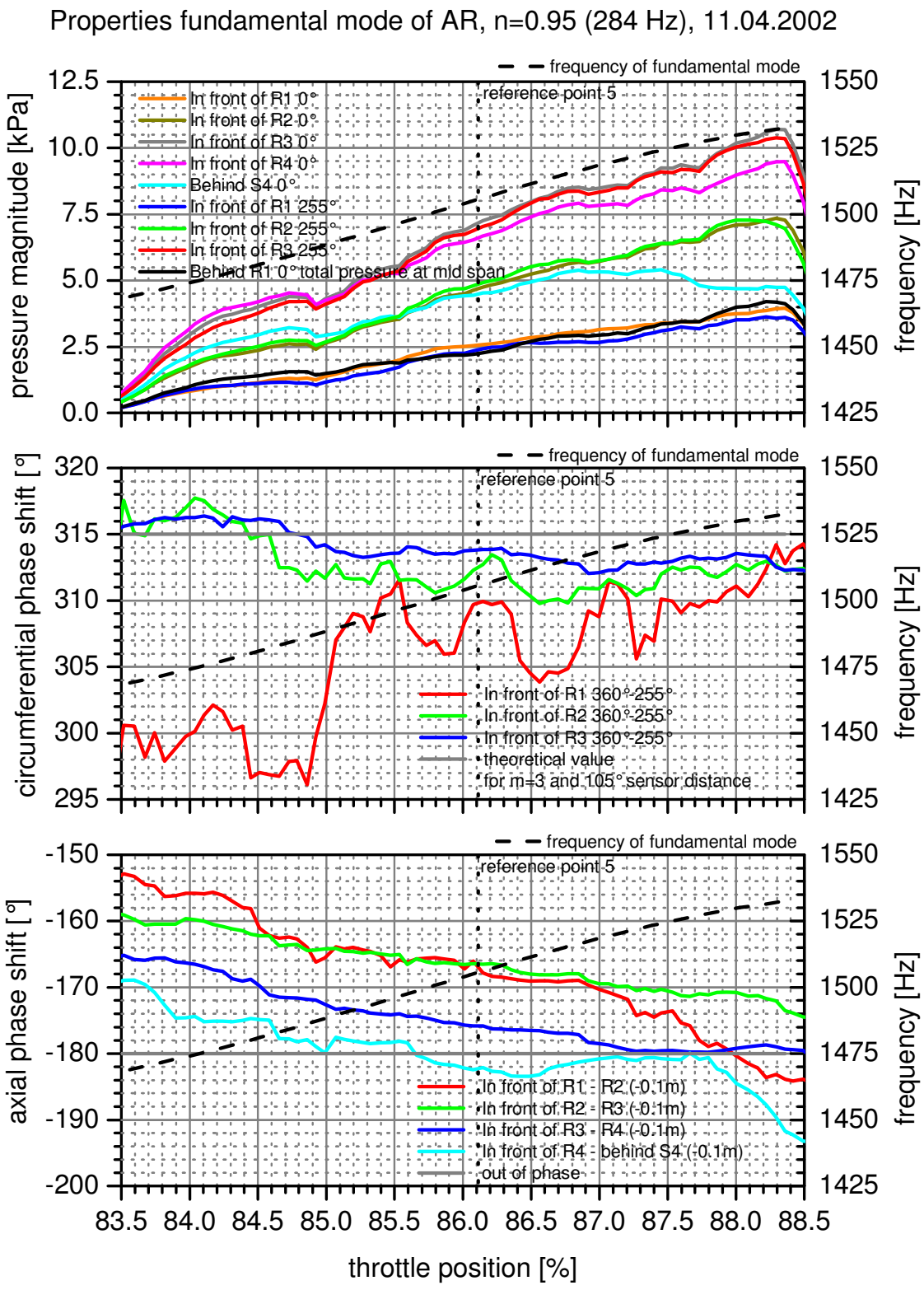

FIG. 22 PRESSURE MAGNITUDE, CIRCUMFERENTIAL AND AXIAL PHASE SHIFT OF ACOUSTIC RESONANCE OVER THROTTLE POSITION

$$p_{m,n}(\varphi,t) = \underbrace{B_{-}\cos\left(m\varphi + \frac{\Delta\varphi(k_z,z_0,t_0)}{2}\right)\exp\left(-i\frac{\Delta\varphi(k_z,z_0,t_0)}{2}\right)}_{\text{standing wave}} + \underbrace{(B_{+}-B_{-})\exp(im\varphi)}_{\text{propagating wave}} \tag{52}$$

The phase shift for two different circumferential positions is given by:

$$\Delta\alpha(\varphi_1,\varphi_2) = \arctan\left(\frac{\mathrm{Im}(p_{m,n}(\varphi_2,t))}{\mathrm{Re}(p_{m,n}(\varphi_2,t))}\right) - \arctan\left(\frac{\mathrm{Im}(p_{m,n}(\varphi_1,t))}{\mathrm{Re}(p_{m,n}(\varphi_1,t))}\right) \tag{53}$$

So, the measured phase shift $\Delta\alpha$ is $m(\varphi_2-\varphi_2)$ if $B_{-}=0$. If this is not the case, the phase shift will be different. The closer the measured phase shift comes to a value of $m(\varphi_2-\varphi_2)$, the lower is the factor B_{-} and so are the amplitudes of the modes spinning against the swirl. It should be noted that in this case the deviation also depends on the circumferential position of the sensors used for the measurement. If the sensors are close to the nodal points of the standing wave, the effect is less pronounced than if they are in between these points. Due to the cosine function in equation (52) these points are in a distance of $360°/(2m)$ which is 60° in our case. So, if two sensors have a distance of 105°, each could be close to a nodal point or close to a point with maximum amplitude. And the position of the nodal points could change if the phase shift $\Delta\varphi$ between those waves travelling with the swirl and those travelling against the swirl changes. For example this happens when the axial wave length is changing. As a result, the positions of the nodal points could be different from stage to stage, too.

In another measurement at the same rotor speed and a throttle position of 84.4%, the phase shift between the sensors d41 (255°) and d51 (301°, 46° distance) was 128° instead of 138°. The phase shift between the sensors d51 and d21 (71°, 130° distance) was 390° like it should be. While the sensors with 46° cannot be close to nodal points at the same time, those with 130° could.

It is shown in the following chapters that the reflection of the acoustic waves at the blade rows is an important resonance condition. The waves are reflected in front of the rotor rows. This means that the first stage is an incomplete resonator, because on the inlet side of the compressor the resonator is open. This explains the lower magnitudes measured in the first stage. If the magnitude of the dominant mode is low, the deviation in the circumferential phase shift caused by other modes rises. This explains why the deviation is decreasing with an increasing magnitude of the acoustic resonance.

Accordingly, the deviation in the measured phase shift in stage 1 from the theoretical value might have several reasons, but the most probable are modes spinning against the swirl.

10.1. Measured pressure magnitude and phase shifts

The axial phase shift shown in the lower diagram in Fig. 22 is changing with the throttle position, too. This is not surprising as the axial wave numbers depend on the axial and circumferential velocity of the mean flow. By throttling the compressor, the axial flow rate decreases and the circumferential flow rate increases. The more important point is that the phase shift increases from values around 160° at the onset of the resonance to 180° at the stall margin of the compressor. At 180° the resonance has exactly opposite phase from stage to stage. Because the axial distance of the sensors is -0.1m and the phase shifts have positive values the waves must travel against the mean flow in axial direction. Again, this is not surprising since the axial wave number of waves travelling against the mean flow is higher than the wave number of waves travelling with the mean flow. So, in the case of a superposition of two sub modes with equivalent amplitudes it follows from equation (47) that the resulting interference wave is travelling against the mean flow. Even so, at this point we can already neglect a single mode travelling with the flow as reason for the acoustic resonance, because in this case the phase shift would have been negative.
This has to be discussed more in detail, comparing the measured phase shift with computed values from the model. Such a computation however, demands the knowledge of the mean flow. For the reference point 5 marked with a black dotted line in Fig. 22, the mean flow was measured in all stages at different axial, circumferential, and radial positions (Braun and Seume (2005)). Additionally with the pneumatic probe in stage one, the flow rate behind the rotor at mid span was measured during the continuous throttling of the compressor.

10.2. Measured radial pressure distribution of AR

In the radial direction, data are not available at all throttle positions since the pneumatic probe is fixed in one position during a measurement. Nevertheless, for three throttle positions (86.1 %, 88.3 %, 88.9 %) at a rotor speed of 0.95 and 1.0, static pressure signals from different radial positions are available for stage one and two behind the rotors. The static pressure signals have been derived from the pressure signals of the four-hole pneumatic probe. The cylindrical probe has four miniature pressure transducers inside its shaft (m, l, r, and y). The head of the probe is shown in fig. 23. One is a tip of hole for measuring the yaw angle (y). Three of them are connected with short channels to holes placed around the circumference at the same axial position at the tip of the probe. One is in the middle (m), one is 60° to the left (l) of m, and one is 60° to the right (r) of m. The hole in the middle (m) should point approximately in the direction of the mean flow and delivers the total pressure signal. The holes left (l) and right (r) are used for the estimation of the static pressure which is basically the mean value of these two pressure signals ($(p_l + p_r)/2$). If the probe does not point directly in the direction of the flow, the direction can be estimated using the difference of the pressure signals from the left and right hole ($(p_l - p_r)/2$). Due to the dynamic pressure transducers also unsteady pressure fluctuations travelling cross to the mean flow could

be found with this probe. With a correction technique based on calibration data from a wind tunnel, the real total and static pressure values are calculated for measurements where the probe does not point directly in the direction of the mean flow (see Rieß and Braun (2003)).

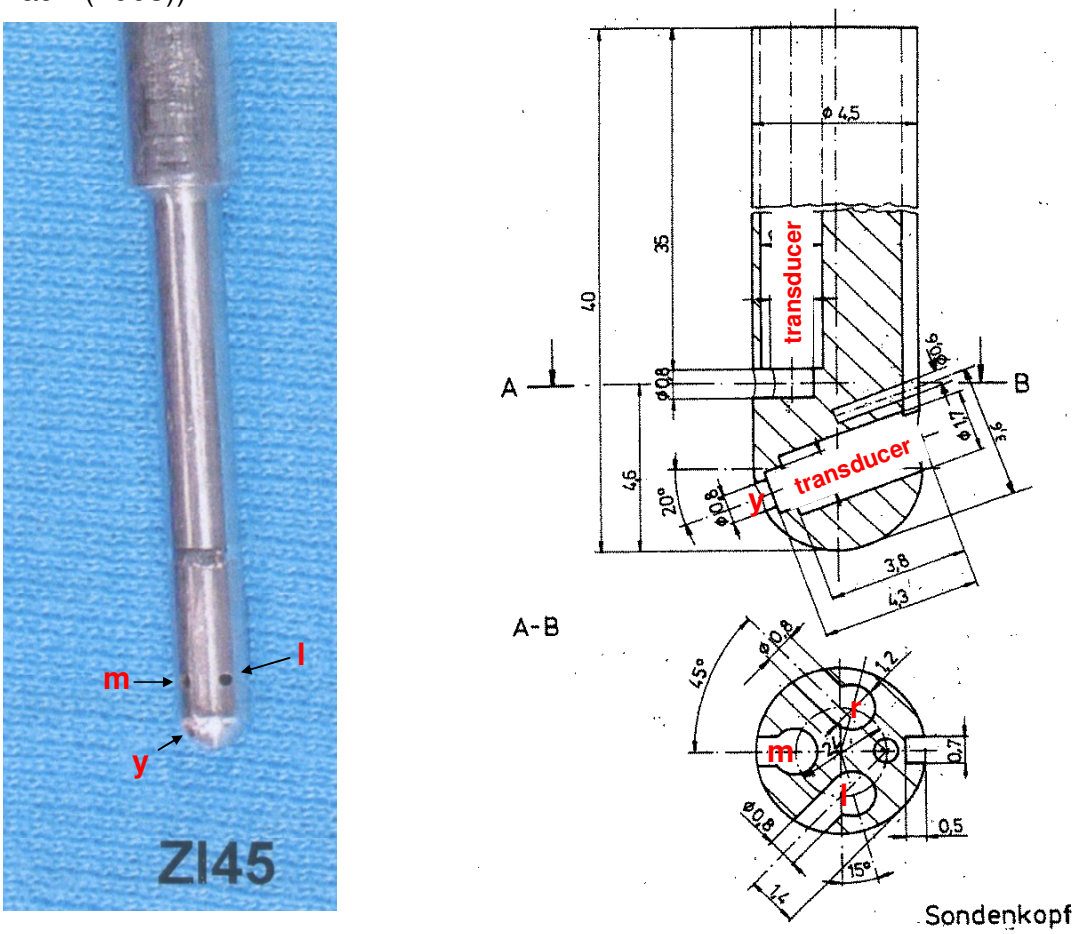

FIG. 23 PHOTO AND DRAWING OF PNEUMATIC PROBE HEAD

The results of measurements are shown in Fig. 24. The static pressure signals are calculated with the correction technique mentioned before. The phase shifts shown in the lower diagrams Fig. 24 are the phase shifts of the calculated static pressure from the pneumatic probe relative to the static pressure signal of the next pressure sensor in the compressor casing. The circumferential position of the pressure sensor in the casing is the same as that of the pneumatic probe.

From equation (39) a radial pressure distribution was computed for the annulus at the position of the probe. To fit the computation results to the diagrams in Fig. 24, the normalized data were multiplied with an arbitrary factor of 3000 that has no further physical meaning. Beside the magnitudes at a radial position of 95% in the first stage, the data fit to the theoretical values of the model. Even if the slope in reality is steeper than in the model, the magnitudes are increasing with the radial position.

So far, we just assumed that the acoustic resonance is caused by a (3,0) mode. However, with this magnitude distribution we can support the assumption. If we would have a (3,1) mode for example, the amplitude would have a minimum in the middle of the channel and increase towards the tip and to the bottom of the channel.

The same result could be derived from the phase shifts in the lower diagrams in Fig. 24. Further a (3,1) mode would implicate a phase change of 180° from the hub to the

tip region, because the function $f(k_{r,m,n}r)$ in equation (39) is changing its polarity from the hub to the tip region for a radial mode number n=1. This means that the radial mode number n of the acoustic resonance in our case is zero.

Another important result is the value of the phase shift itself. In the first stage, the phase shift is close to 90° while in the second stage it is between 100° and 120°. This fits the results of the axial phase shift between the stages of approximately 180° in Fig. 22, because the axial distance in Fig. 24 (52mm) is a little bit more than half of the distance in Fig. 22 (100mm). From the theory of our model, the phase shift is supposed to be constant for a (3,0) mode at the same axial and radial position. Yet, the model assumes a rigid body flow which is not true in reality. The influence of the varying axial and circumferential flow velocity with the radius is observable in the phase shifts because the axial wave numbers at the hub are different than those at the tip. In the first stage where the variation of the circumferential Mach number of the flow with the radius is low (see upper diagrams in Fig. 25), the variation of the phase shifts is low, too.

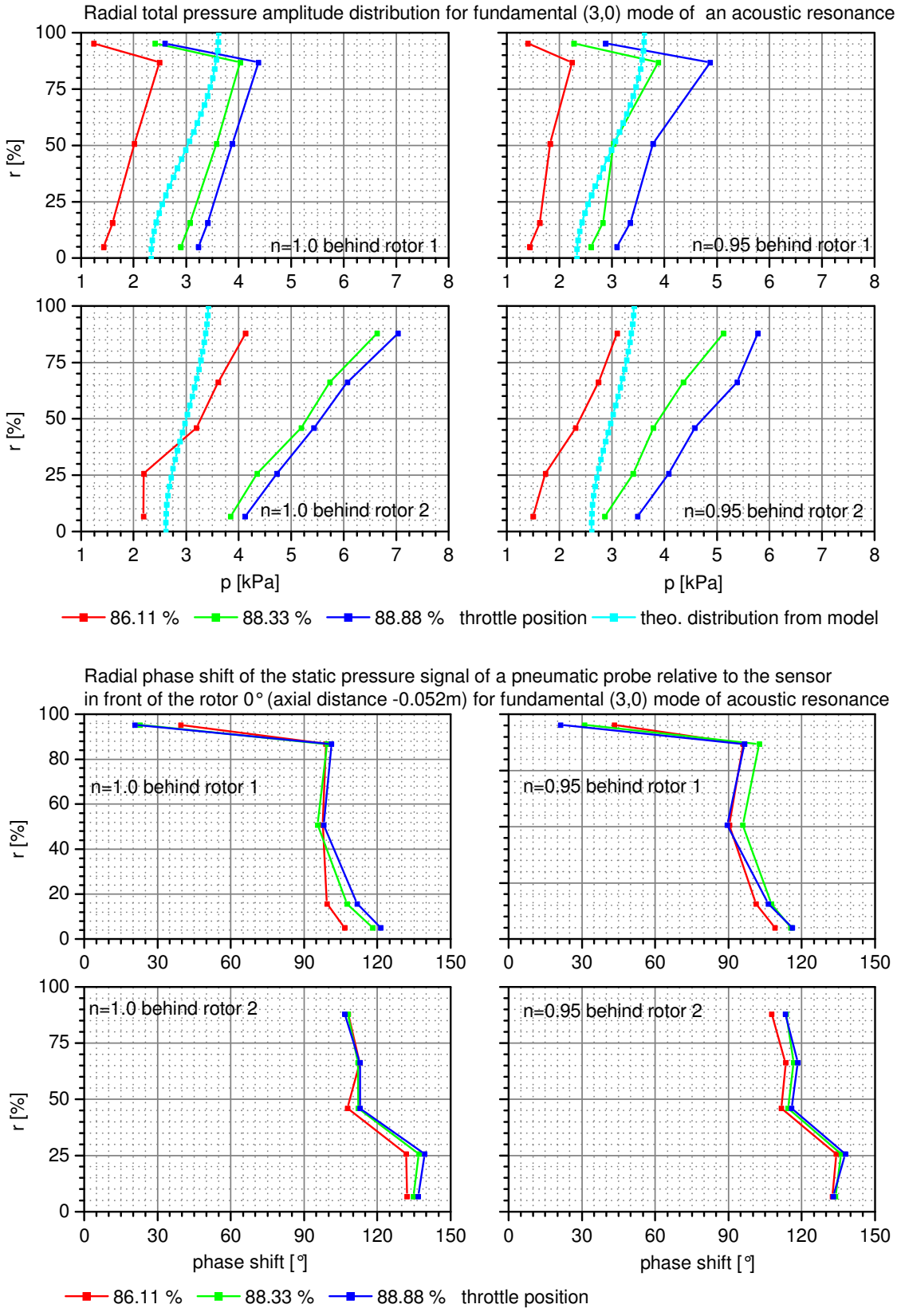

FIG. 24 RADIAL PHASE AND AMPLITUDE OF ACOUSTIC RESONANCE IN STAGE 1 AND 2

10.3. Application of model to flow measurements

For the reference point 5 marked with a black dotted line in Fig. 22, the mean flow and fluid temperature was measured in all stages at different axial, circumferential, and radial positions with a steady pneumatic probe (see Braun and Seume (2005)). The resulting axial and circumferential Mach numbers are shown in the upper diagram in Fig. 25. From these values and the Eigenvalue $k_{r,m,n}$ behind each blade row, the cut-off frequency of the (3,0) mode has been calculated with equation (42). As already discussed, the presence of flow in the duct leads to four different sub modes with different wave numbers k_z for each duct mode, depending on the direction of propagation (with or against the flow in circumferential and axial direction). The cut-off frequency depends only on the sense of rotation of the mode, not on the axial direction of propagation (see equation (42)). Waves travelling against the flow in circumferential direction are cut-off at higher frequencies than those travelling with the flow. This means that behind the rotors, where the deflection of the flow is high, the cut-off frequency is higher than behind the stators where the deflection is lower. This is illustrated in the lower diagram in Fig. 25.

Due to the varying cross section, this Eigenvalue $k_{r,m,n}$ is different for each stage of the compressor and accordingly also the cut-off frequency. Further, the fluid temperature increases during compression and so does the speed of sound a. Moreover, the axial and circumferential Mach number is different for each stage. The results show that even though the flow field and duct cross section vary from stage to stage, the resulting cut-off frequency of each stage is nearly identical behind the stator rows. Only at the compressor outlet behind stator 4 the cut-off frequency is different. Behind the rotor rows the deviation is higher, but except the first rotor the cut-off frequency for the modes spinning against the swirl is similar in stage two, three and four. This is, because the effects of rising temperature and increasing hub ratio partly cancel each other.

The measured frequency of the acoustic resonance in reference point 5 is about 1510 Hz. This means that the mode against the swirl is cut off behind the rotor rows where the deflection is high. Behind the stator, all sub modes of the (3,0) mode can propagate regularly at a frequency f of 1510 Hz.

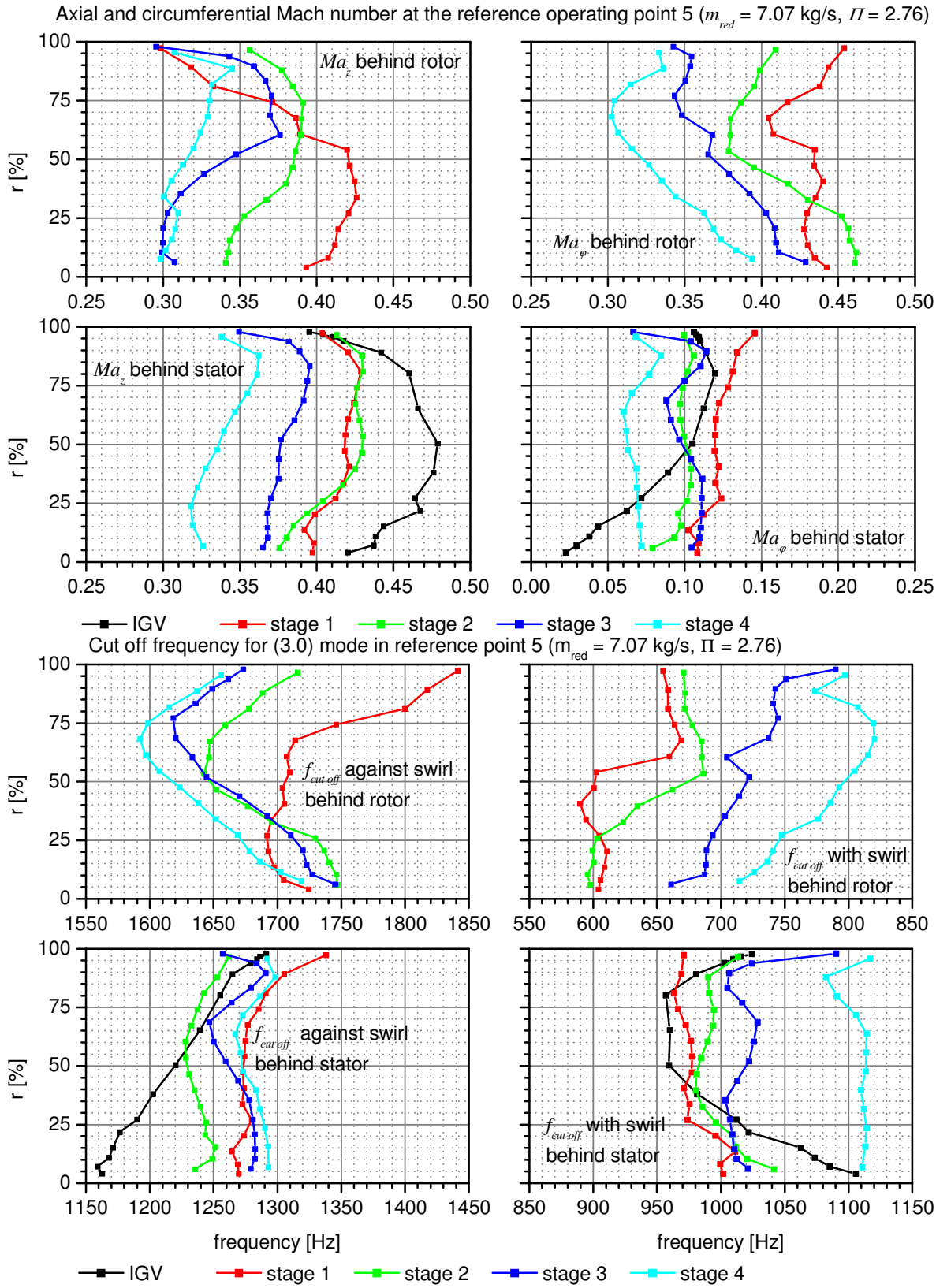

FIG. 25 CIRCUMFERENTIAL AND AXIAL MACH NUMBERS IN REFERENCE POINT 5 WITH CUT OFF FREQUENCIES FOR MODE (3,0)

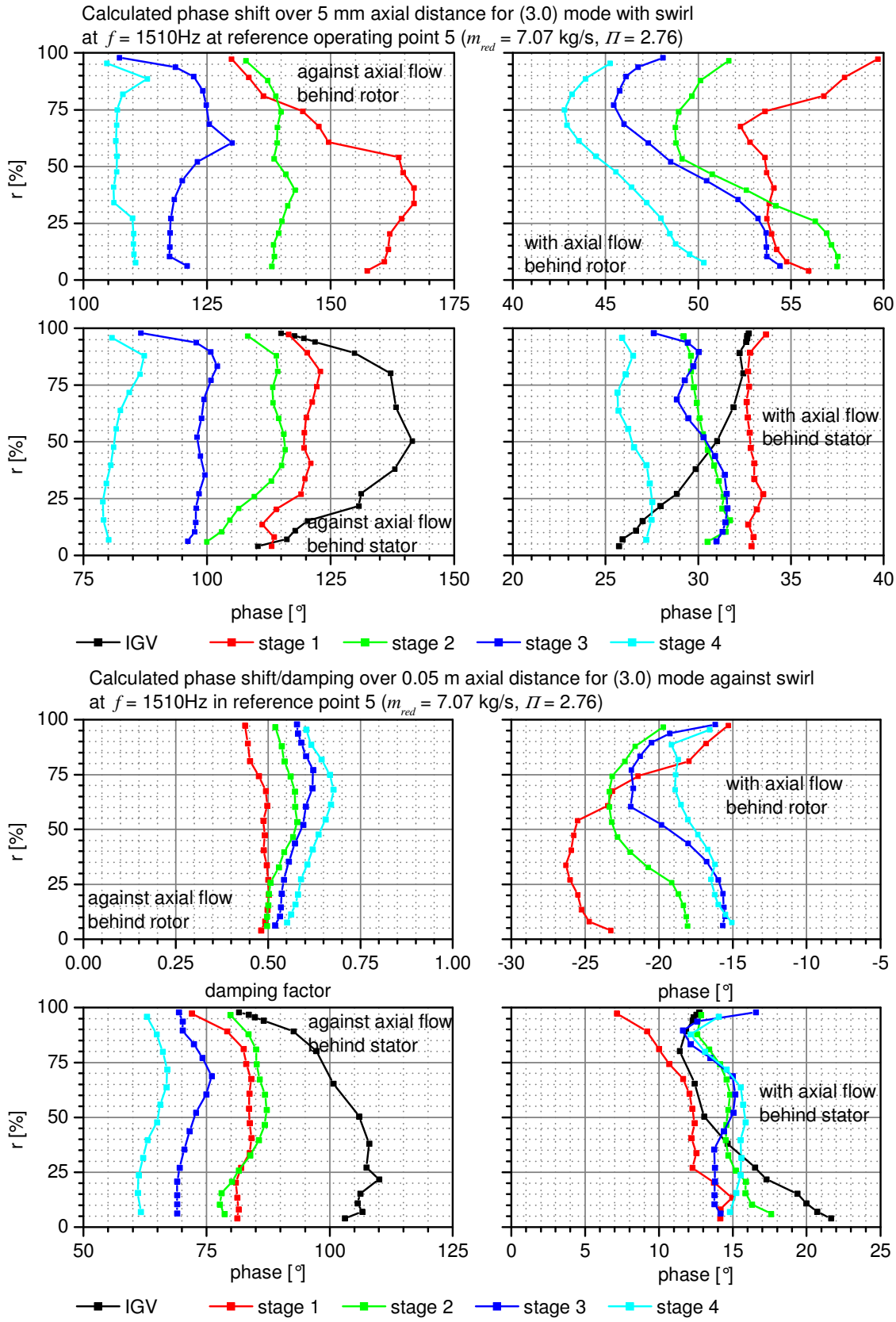

FIG. 26 AXIAL PHASE SHIFT AND DAMPING OF ACOUSTIC RESONANCE

Together with this frequency f, the axial wave number k_z can be calculated from the model for all sub modes of the (3,0) mode. The results are shown in Fig. 26 as resulting phase shift over a distance of 50 mm. This is the axial distance between the pressure transducers in the compressor casing and half the axial extent of a stage. Where the modes are cut off, the axial wave number with and against the axial flow has the same amount, only the polarity is opposite. Therefore it is shown in Fig. 26 for the direction with the axial flow only. Because the mode is cut-off, it is damped. The damping factor D

$$D = \exp\left(-\frac{\sqrt{-\left(k \pm Ma_\varphi k_{r,m.n}\right)^2 + \left(1 - Ma_z^2\right)k_{r,m,n}^2}}{1 - Ma_z^2} \right) \tag{54}$$

is shown in Fig. 26 instead of the axial wave number against the axial flow.

From the circumferential phase shift of the pressure signals at the frequency of the acoustic resonance, we suggested that the acoustic resonance contains only those sub modes traveling with the swirl. This fits the fact that modes traveling against the swirl are cut off behind the stator rows. If we further assume that the remaining two sub modes have the same amplitude, their sum is given by equation (47) on Page 42. The phase shift $\Delta\alpha$ from one pressure signal to another on the same circumferential but different axial position is given by equation (49) on Page 43. The resulting phase shift over a stage is given by the sum of the phase shift over the rotor and stator row. This is approximately the sum of half of the phase shift behind the stator in front of the stage, the phase shift behind the rotor and half of the phase shift behind the stator in the stage. The result of the summation is shown in the left diagram of Fig. 27. The calculated phase shift is around -80°, depending on the stage a little bit more or less.

As shown in equation (46) the sum of two harmonic functions with the same amplitude is again a harmonic function with a modulation in amplitude.

$$\begin{aligned} p(z,t) &= B\exp\left(i\left(k_{+z}z - \omega t\right)\right) + B\exp\left(i\left(-k_{-z}z - \omega t\right)\right) \\ &= B\cos\left(\frac{k_{+z} + k_{-z}}{2}z\right)\exp\left(i\frac{k_{+z} - k_{-z}}{2}z\right)\exp\left(-i\omega t\right) \end{aligned} \tag{55}$$

As long as the cosine function in equation (55) is not changing its polarity the phase shift $\Delta\alpha$ between two pressure signals taken from different axial positions z_1 and z_2 is given by:

$$\Delta\alpha = \frac{k_{+z} - k_{-z}}{2}\left(z_2 - z_1\right) \tag{56}$$

If there is a change in the polarity, the phase shift between the two pressure signals is 180° more or less depending on the interval that is used for the presentation of the phase shift because $-1 = \exp(i\pi)$ and π is equivalent to 180°. For sure this is the case when the argument of the cosine function is shifted by 180°. In the right diagram in Fig.

27, the calculated phase shift in the pressure signal between two points along the compressor axis with a distance of 100mm is shown. In the left diagram the argument of the harmonic function and in the right diagram the argument of the cosine function is shown. It is less than or approximately 180°.

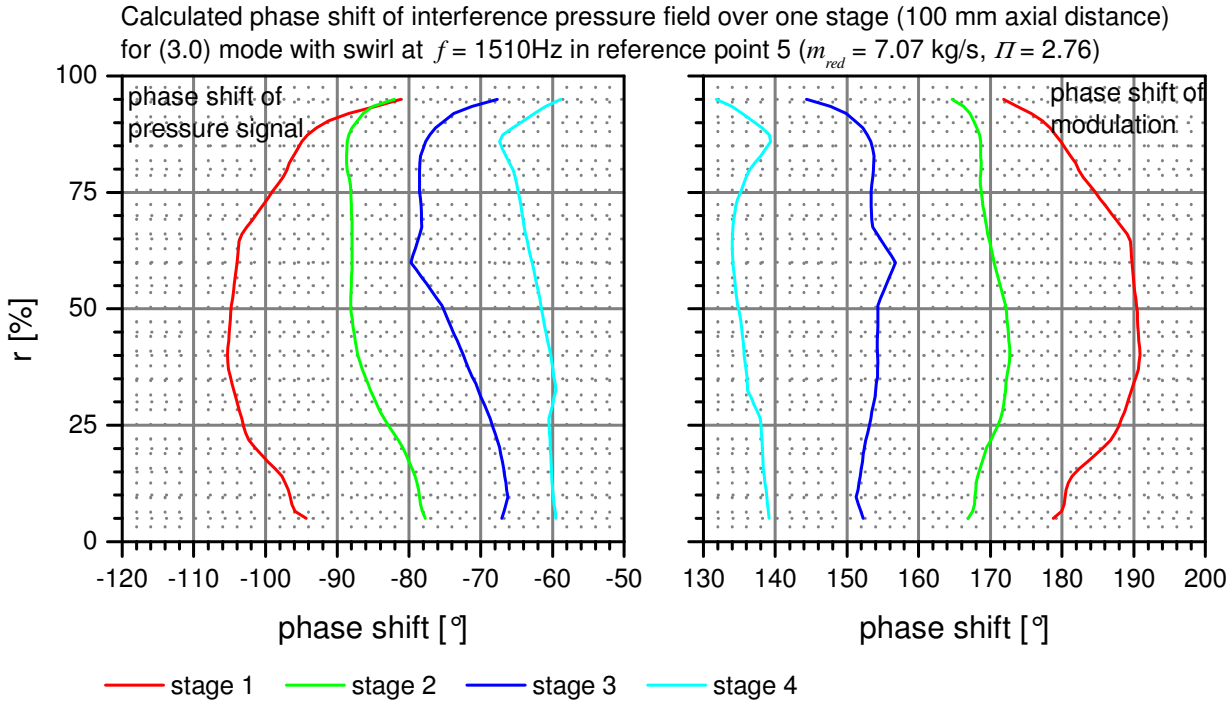

FIG. 27 PHASE SHIFT OF INTERFERENCE WAVE

The position of the nodal points of the modulation function is unknown so far and accordingly, it is not possible to know if there is a change in polarity or not. Still, because the phase shift is around 180°, a change in polarity is very likely. The calculated phase shift is between -105°+180°=75° (stage 1) and -60°+180°=120° (stage 4). This is in contradiction to the measured values between -165° and -185° in Fig. 22. But for all stages the measured values are nearly exactly 120° more then the calculated values from the model and static flow measurements. Because the deviation of the model and the measurements is nearly the same in every stage, it is assumed that the model is qualitatively correct but incomplete. There must be a mechanism that shifts the phase of the acoustic waves and that is unaccounted in the model so far.
The model already considers the deflection of the flow caused by the blades, but not the transmission and reflection of acoustic waves through blade rows. It is known that the phase of an acoustic wave is shifted when it passes through a blade row (see section 9.1 and Kaji and Okazake (1970)) and for a resonance reflection must take place to trap the modes in the compressor. This leads to the discussion of the reflection and transmission of acoustic waves through blade rows in the next section as

a possible reason for the 120° difference between model and measurement in the phase shift.

IGV	r_{LE} [mm]	$\alpha_{m.LE}$[°]	r_{TE} [mm]	$\alpha_{m.TE}$ [°]	α_s[°]	l [mm]	*l/s [-]*	*D/l* [-]
	71.81	90	75.27	90	90	27	1.54	0.1
	105.46	88	107.02	81.3	85.7	29.81	1.16	0.1
	130.55	88.3	131.25	77	83.6	31.91	1.01	0.1
	151.55	88.7	151.82	75.2	82.8	33.68	0.92	0.1
	170	89	170	74.8	82.7	35.24	0.86	0.1
Rotor 1	r_{LE} [mm]	$\alpha_{m.LE}$[°]	r_{TE} [mm]	$\alpha_{m.TE}$ [°]	α_s [°]	l [mm]	*l/s [-]*	*D/l* [-]
	76.72	128	83.39	96	99	42	1.99	0.115
	107.82	136	110.67	75	115.2	43.5	1.47	0.082
	131.69	141	132.87	60.4	127	44.12	1.22	0.066
	152.01	145	152.35	49.8	135.2	44.5	1.07	0.054
	170	148.4	170	42.2	141.9	44.8	0.96	0.045
Stator 1	r_{LE} [mm]	$\alpha_{m.LE}$[°]	r_{TE} [mm]	$\alpha_{m.TE}$ [°]	α_s [°]	l [mm]	*l/s [-]*	*D/l* [-]
	85.93	51	88.9	89.5	74.3	32.5	1.79	0.064
	112.3	48	117	85	70.4	33.4	1.41	0.073
	133.94	46.3	136.84	82.8	68.5	34.15	1.21	0.078
	152.85	45.5	154.24	82.2	68.4	34.8	1.09	0.082
	170	45	170	82	68.7	35.4	0.99	0.084
Rotor 2	r_{LE} [mm]	$\alpha_{m.LE}$[°]	r_{TE} [mm]	$\alpha_{m.TE}$ [°]	α_s [°]	l [mm]	*l/s [-]*	*D/l* [-]
	95.98	138	102.05	85.2	110	39.5	1.75	0.091
	119.12	139.9	122.34	69	121.2	40.6	1.46	0.074
	138.13	143.8	139.7	56.9	130	41.45	1.29	0.058
	154.84	147	155.37	48.3	137	42.15	1.17	0.049
	170	150	170	41.3	142.9	42.75	1.08	0.041
Stator 2	r_{LE} [mm]	$\alpha_{m.LE}$[°]	r_{TE} [mm]	$\alpha_{m.TE}$ [°]	α_s [°]	l [mm]	*l/s [-]*	*D/l* [-]
	104.61	45.5	109.66	88	72.3	32	1.55	0.064
	124.04	47	127.76	85.6	70.9	32.91	1.35	0.072
	140.79	47.5	143.21	84	70.1	33.68	1.22	0.079
	155.9	47	157.12	84	69.8	34.37	1.12	0.085
	170	46.4	170	83.7	69.7	35	1.05	0.090
Rotor 3	r_{LE} [mm]	$\alpha_{m.LE}$[°]	r_{TE} [mm]	$\alpha_{m.TE}$ [°]	α_s [°]	l [mm]	*l/s [-]*	*D/l* [-]
	112.23	140	114.16	85.5	118	40.22	1.64	0.090
	129.41	141.4	131.58	63.5	126	42.19	1.50	0.074
	144.21	143.3	145.27	54.2	132.8	43.6	1.39	0.063
	157.59	145.4	157.78	47.5	138.2	44.7	1.31	0.055
	170	147.9	170	42.2	142.4	45.6	1.24	0.047
Stator 3	r_{LE} [mm]	$\alpha_{m.LE}$[°]	r_{TE} [mm]	$\alpha_{m.TE}$ [°]	α_s [°]	l [mm]	*l/s [-]*	*D/l* [-]
	117.92	44	121.06	87.8	71.1	35	1.60	0.064
	132.72	45.5	135.06	85.9	70	35	1.42	0.071
	146.03	46.3	147.59	85	69.5	35	1.29	0.077
	158.34	46	159.16	85.6	69.7	35	1.20	0.082
	170	45.5	170	85.6	69.6	35	1.11	0.086
Rotor 4	r_{LE} [mm]	$\alpha_{m.LE}$[°]	r_{TE} [mm]	$\alpha_{m.TE}$ [°]	α_s [°]	l [mm]	*l/s [-]*	*D/l* [-]
	122.44	144	124.04	67.5	125	37.79	1.52	0.085
	135.96	144.7	136.62	57.5	131.5	39.22	1.42	0.062
	148.13	146	148.27	50	137	40.3	1.34	0.052
	159.41	148	159.43	44.5	141.2	40.7	1.26	0.046
	170	150	170	40.5	144.7	40.8	1.18	0.042
Stator 4	r_{LE} [mm]	$\alpha_{m.LE}$[°]	r_{TE} [mm]	$\alpha_{m.TE}$ [°]	α_s [°]	l [mm]	*l/s [-]*	*D/l* [-]
	124.59	43	125.01	90	72	36.41	1.67	0.070
	137.03	43	137.67	90	72	36.41	1.52	0.070
	148.61	43	149.16	90	72	36.41	1.40	0.070
	159.55	43	159.89	90	72	36.41	1.31	0.070
	170	43	170	90	72	36.41	1.23	0.070

TABLE 5 BLADE GEOMETRY OF REFERENCE SETUP

10.4. Reflection and transmission of acoustic waves through blade rows

In Section 9.1, a model of Koch (1971) and Kaji and Okazaki (1970) was introduced. The blades in the model are plane plates in a plane cascade. For the application of the model, we will calculate the incidence angle of the acoustic wave depending on the radius and compare it with the stagger angle of the cascade at that radius. The blade geometry of the reference setup is summarized in Table 5. For the stagger angle α_s we used the same convention as in Fig. 17 on page 34. The incidence angle θ_I of the sound wave in Fig. 17 is given relative to the stagger angle. The incidence angle $\beta_\pm$ in equation (45) on page 41 is given relative to the compressor axis in a fixed frame. For a comparison of the incidence angles calculated from our model and static flow measurements with the results of Koch, Kaji and Okazaki models in Fig. 18 we have to transform the angles $\beta_\pm$ into the angles θ_I-α_s. In an intermediate step, the angles $\beta_\pm$ must be converted in the angles $\beta_\pm^{flow}$ which is the angle $\beta_\pm$ in the frame of the flow. This transformation is done by the following equations

$$\beta_{+,\pm}^{flow} = \arctan\left(\frac{\sin\beta_{+,\pm} \mp Ma_\varphi}{\cos\beta_{+,\pm} - Ma_z}\right)$$
$$\beta_{-,\pm}^{flow} = \arctan\left(\frac{\sin\beta_{-,\pm} \mp Ma_\varphi}{\cos\beta_{-,\pm} + Ma_z}\right) \qquad (57)$$

The second sign in the subscript index is positive for waves traveling with the swirl and negative for those traveling against the swirl. All angles $\beta_\pm$ in Fig. 28 are already converted. Because all angles are converted, the superscript ^{flow} is not shown explicitly. The thin black arrows are used to show the incidence angles $\beta_\pm$ but their length does not represent the speed of the wave. In contrast, the length of the other vectors is proportional to the speed of flow, rotation, and sound in the machine. The profiles shown are the profiles of the first and second stage of the present compressor.
Due to the rotation of the rotor, the incidence angle must be known in the rotating frame of the rotor for reflection and transmission at the rotor rows. This is also shown in Fig. 28. A superscript "*fix*" means that the angle is given in the fixed frame and "*rotor*" means that it is given in the rotating frame. Using equation (45) the incidence angle $\beta_\pm^{rotor}$ can be calculated directly by the following equation.

$$\beta_\pm^{rotor} = \arctan\left(\frac{rk_{\pm z}\left(f - mf_r\right)}{mf}\right) \qquad (58)$$

With f_r as rotor speed and f as frequency of the acoustic wave or from a incidence angle in the fixed frame:

$$\beta_{z,\pm}^{rotor} = \arctan\left(\frac{\sin\beta_{z,\pm} \mp \frac{2\pi r f_r}{a}}{\cos\beta_{z,\pm}}\right) \tag{59}$$

The sign is positive for propagation in direction of rotation/swirl and negative against. The conversion into the convention used by Koch is given by the following equations:

$$\begin{aligned}
\theta'_{I,S+} - \alpha'_{s,R} &= 270° - \beta_{S+}^{rotor,flow} \\
\theta_{I,S-} - \alpha_{s,S} &= 90° - \beta_{S-}^{flow} \\
\theta_{I,R+} - \alpha_{s,S} &= -90° + \beta_{R+}^{flow} \\
\theta'_{I,R-} - \alpha'_{s,R} &= 90° + \beta_{R-}^{rotor,flow}
\end{aligned} \tag{60}$$

The significant incidence angles at which the reflection or transmission becomes zero could be calculated for the stator rows directly from equation (35) and (36). For the rotor blades, the stagger angle is above 90°, so the sketch in Fig. 17 must be mirror imaged with respect to the machine axis. The stagger angle in the mirrored sketch is shown as α_s' and the incidence angle as θ_I' in Fig. 28. An R in an index of an angle in Fig. 28 means that the acoustic wave hits a rotor, an S means that it hits a stator. A plus means that the wave travels with the flow, a minus that it travels against the flow in axial direction.

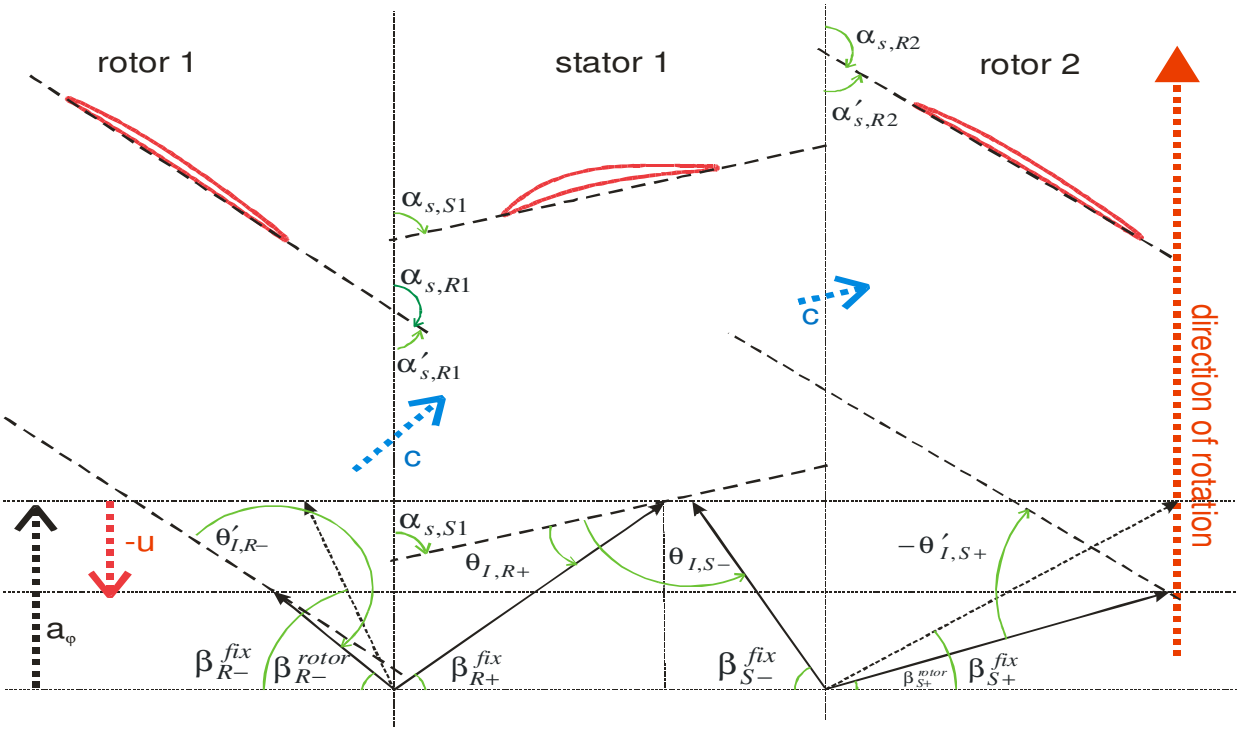

FIG. 28 SCHEMA OF FLOW AND INCIDENCE ANGLES OF ACOUSTIC WAVES IN THE PRESENT COMPRESSOR

The angles shown in Fig. 28 are close to the real incidence angles in the machine for the operating point where the acoustic resonance and the flow field has been measured. So, from the sketch it is already seen that behind the rotor and in front of the stator the transmission is high and nearly no reflection occurs. Behind the stator rows and in front of the rotor, the situation is not as obvious, but nevertheless it shows that here reflection will take place.

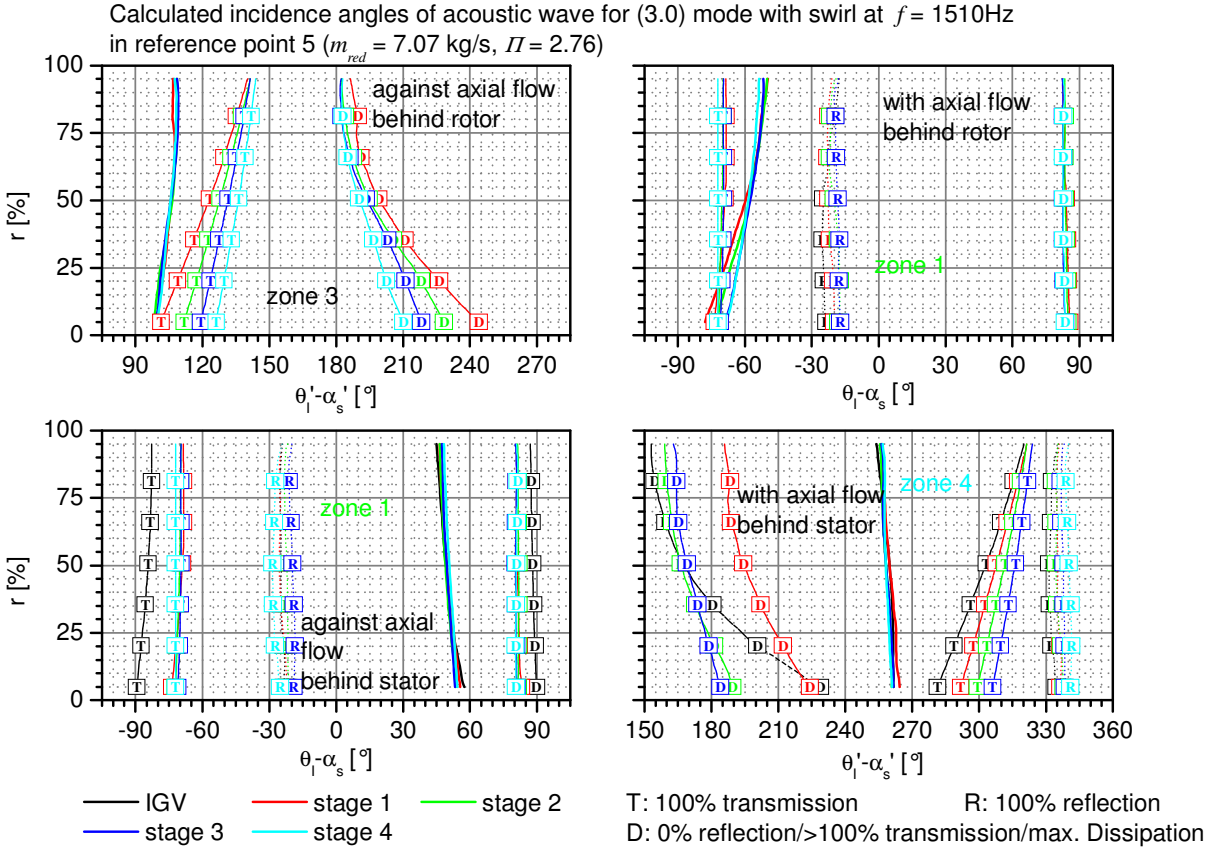

FIG. 29 INCIDENCE ANGLES OF ACOUSTIC WAVE AT BLADE ROWS

Fig. 29 shows the calculated incidence angles for the reference point 5 in the operating map over the normalized radius of the annulus. In addition, the characteristic incidence angles at which the transmission or reflection coefficient becomes zero based on the Koch-Kaji-Okazi model are shown. They have been calculated with equation (35) and (36) on page 35. For reflection and transmission at the rotor rows, the Mach number Ma^{rotor} of the mean flow has been calculated in the rotating frame of the rotor with the following formula.

$$Ma^{rotor} = \sqrt{Ma_z^2 + \left(Ma_\varphi - 2\pi r f_r\right)^2} \tag{61}$$

The results in Fig. 29 show very clearly that the waves of the considered mode traveling with the flow are nearly totally transmitted when they enter a stator rotor row

(upper right diagram). In contrast, those traveling against the flow are nearly totally transmitted when they enter a rotor row (upper left diagram). This means that in the area behind the rotor and in front of a stator the blades are not a resistance for the propagation of the acoustic mode.
Behind a stator and in front of a rotor the situation is different. For those waves traveling with the axial flow, the incidence angle lies between the point D and T in the zone 4 in Fig. 18 on page 36. In zone 4, the reflection coefficient increases with the Mach number and is maximal approximately in the middle between the points D and T. The Mach number in the rotating frame of the rotor used for the calculation here is about 0.8, so it can be assumed that the reflection coefficient is close to its local maximum and will be around 70-90%.
For waves traveling against the flow, the incidence angle lies between point R and D close to point D in zone 1. This is an area where the dissipation in the model used is high. As explained in section 9.1, the reason is a destructive interference of the incidence and reflected wave. This means for point D that a total reflection of the sound wave occurs, but the reflected waves cancel with the incoming waves, so that the acoustic field in front of the blade row vanishes. The model is using a single blade row in an open space. In a multistage machine with multiple modes the interference is more complex. Nevertheless, it could be assumed that the waves traveling against the flow are mainly reflected by the upstream stator rows. How these waves interfere with the other modes in detail could not be explained with this simple model.

The above may be such summarized that behind the rotor in front of a stator row the up- and down stream waves can pass the rows with low resistance and that behind the stator row in front of the rotor row, both up- and down stream waves are mainly reflected by the blade rows.
This means that in each stage there is a turning point. The resulting acoustic field of up- and down-stream waves measured in the compressor has a half wavelength that is between 97 and 109mm. This is close to the axial length of a stage in the compressor with 100mm.
Because the incidence angle of the acoustic field with respect to the blade rows depends on the mean flow velocity (especially the axial Mach number) and the rotor speed, it is self-evident that the acoustic resonance exists only in a certain speed range and with a certain axial flow velocity; in the unthrottled compressor at high rotor speed, the axial Mach number is too high while at low speed, the incidence angle with respect to the rotor blades probably does not fit anymore.
Based on the experimental data used for the present work, this latter reason could not be proven conclusively. Here a new systematic study based on the results of this work is necessary where more than one speed line and more than one operating point on the speed line will be examined. However, two cases will be discussed in the next subsections: The first case is throttling at constant rotor speed and the second is a speed variation at constant throttle position.

Apart from this, the question of the driving force of the resonance remains unanswered. Within the present work no final answer will be given, but it is most probable that the broad band background noise is driving the resonance. This is assumed for two reasons. Firstly, no other mechanism providing a noise source with a discrete

frequency spectrum in the frequency range of the acoustic resonance was found. Secondly, the resonance occurs close to the stability limit where the incident flow of the blades is not optimal. This causes shear layers in the flow which are acting as noise sources. For the same reason a rotating instability or tip clearance noise might work as noise source, too. The dominant frequency of the tip clearance vortices depend mainly on the shroud length l and mean flow velocity c. According to Bae et al. (2004) and Mailach et al. (2001) the value for the reduced frequency $f_R = lf / c$ is between 0.35 and 1.0. This means for the present compressor at design speed that the dominant frequency of the tip clearance vortices is between 1200 – 3500 Hz. The frequency of the acoustic resonance is in between this frequency range.
In the case of a flow separation as driving force its frequency is coupled to the frequency of the acoustic resonance so that they could not be separated in the spectra of the pressure signals anymore. It is known from tests in wind tunnels that the separation frequency of flow separations, like Von Karman vortex streets, are coupling into the frequency of external periodic pressure fields like the acoustic modes of the wind tunnel for example (see Ahuja and Burrin (1984), Parker et al. (1966-1984)). If flow separations or noise induced by shear layers are driving the acoustic resonance, the driving force as well depends on the operating point of the compressor. Beside the improved measurements mentioned in the latter paragraph a valid model of the driving force is necessary to predict the inception of the acoustic resonance.

10.5. Transient flow measurements at constant rotor speed

For the calculation of axial and circumferential phase shifts shown in Fig. 22 and for the contour plot in Fig. 10, data from a transient measurement were processed. The measurement procedure was described in the beginning of this chapter. The result showed that the properties of the acoustic resonance, like frequency and phase, are changing with the throttle position of the compressor. Nevertheless, throttle position and frequency for example are not linked directly but by the flow.
The model that was used described the relationship of acoustic resonance and flow parameters. The application of steady flow measurements demonstrated that the measured acoustic mode is not cut off in the annulus of the compressor under the measured flow conditions. The findings also showed that the blades in the space between the rotor and stator are not a high resistance for the propagation of the acoustic waves at a rotor speed of 0.95.
In contrast, it could not be shown why the acoustic resonance is not excited all over the operating map of the compressor at any rotor speed. Because of the limited data base, it is not possible to answer this question conclusively. However, the rotor speed has a high influence on the incidence angles of the acoustic waves to the rotor blades, which is an explanation why the resonance exists only at high rotor speeds, i.e. because at other speeds the reflection conditions are not satisfied.
Beside the rotor speed, the acoustic resonance is only excited at operating points close to the stability limit where the circumferential Mach numbers are high and the axial Mach numbers comparable low. So, the change of the acoustic resonance with the circumferential and axial Mach number should give an answer to the question why the resonance is excited only at high rotor speeds with relatively low mass flow rates.

However, steady flow measurements under resonant conditions in the whole compressor are available only for one specific flow rate. Nevertheless, we can use the data provided by the pneumatic probe that was already used for the measurement of the radial pressure distribution in Fig. 24 on page 51. This probe was inserted in the first stage of the compressor behind the rotor 1 at mid span when the compressor was throttled slowly to the stability limit. With the data measured at this single location, the properties of the acoustic resonance will be compared between directly measured values and calculated values based on measured mean flow data.

10.5.1. Frequency shift and mean flow parameters

In an earlier work (Hellmich and Seume (2006)), it was assumed that the frequency of the acoustic resonance follows the cut off frequency of those sub modes spinning against the swirl. According to Rienstra (1999) this is because at the position in the duct where the cut off frequency is reached, a “turning point” for the mode is created. This means that the mode is totally reflected in axial direction. The actual analysis shows that the acoustic resonance is mainly formed by those sub modes that are spinning with the flow. Nevertheless, it is still true that the frequency of the acoustic resonance f_{res} is increasing approximately proportional to the cut off frequency of the modes spinning against the flow. Formulated as an equation this means:

$$f_{res} \propto \sqrt{1-Ma_z^2} + Ma_\varphi \tag{62}$$

Unfortunately the circumferential Mach number is in the area of the operational map where the acoustic resonance exists nearly proportional to f_{res}, too. A correlation analysis of different expressions derived from the mean flow velocity with the f_{res} in Fig. 30 has the result that the best correlation is given for:

$$f_{res} \propto \sqrt{1-Ma_z^2} \tag{63}$$

For this expression, the deviation from f_{res} is the smallest. This means that the frequency of the acoustic resonance depends only on the axial and not on the circumferential Mach number of the mean flow.

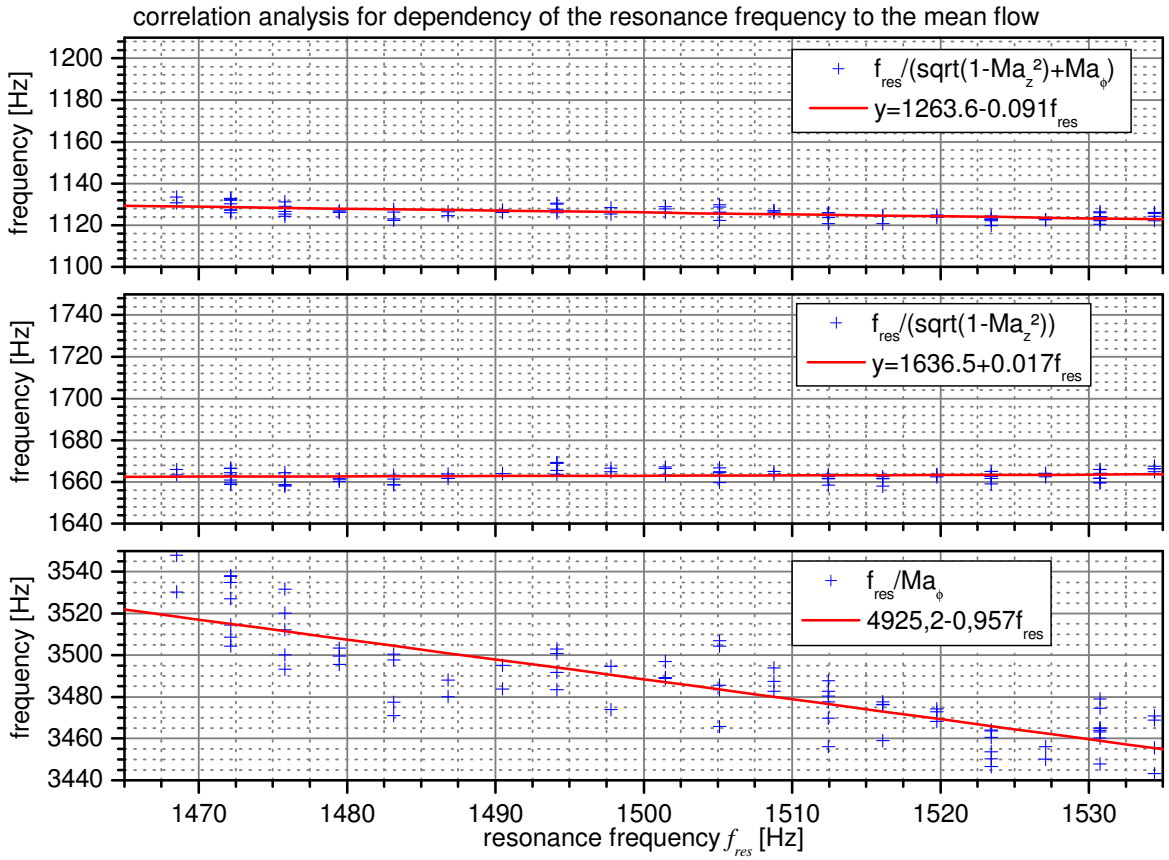

FIG. 30 CORRELATION ANALYSIS OF MEAN FLOW VELOCITY AND RESONANCE FREQUENCY

10.5.2. Axial phase shift and mean flow parameters

In Fig. 22 on page 46, the axial phase shift of the acoustic resonance for each stage was shown vs. the throttle position. The subsequent analysis demonstrated that the calculated phase shift from the static flow measurements in reference point 5 did not fit the measured phase shift. The measurement deviates from the calculation by a constant factor of 120°.

With the data of the pneumatic probe, it is now possible to measure the axial phase shift of the acoustic resonance over the rotor 1 and stator 1 separately. The results are shown in Fig. 32. As supposed from the different reflection conditions behind rotor and stator rows and from the difference in the circumferential flow velocity, the phase shift across the rotor is different from the phase shift across the stator.

However, it is a surprising outcome that the phase shift across the rotor is nearly constant at 90° independent from the change of the mean flow, while the phase shift over the stator is changing with the flow. Therefore the measured phase shift over the stator was compared with the calculated phase shift from our model. The axial and circumferential Mach numbers and the frequency of the acoustic resonance used for the calculation were measured with the pneumatic probe behind the rotor 1 at mid span. It was assumed that the measured acoustic resonance was an interference of the up- and downstream (3,0) mode spinning with the flow. The amplitude of both sub

modes was assumed to be equal. The agreement between the directly measured and the calculated values was very good. This is the proof for the thesis that each stage of the compressor works as resonator. In the rotor rows the waves are reflected. This causes a constant phase shift of 90° between the acoustic field in front of the rotor and behind the rotor. In the space between the rotors, the acoustic field can be described by the simple model of an acoustic field in an annulus with axial and circumferential flow. So in contradiction to the model used for the explanation of the reflection and transmission of the acoustic waves the upstream waves must be transmitted at the stator rows and reflected at the rotor rows. The transmission at the stator rows might be explained by the fact, that the interference wave of up- and downstream waves has a nodal point in the middle between the reflection points. Because the waves are reflected at the rotor rows and the stator row is in the middle between the rotor rows, the dissipation of energy is low due to the low pressure amplitude of the interference wave in the stator rows. This is illustrated by a simulation of the acoustic pressure field in fig. 31. Here the pressure field of the interference wave between two rotor rows is shown as contour plot. The shown data are taken from a simulation of the acoustic field based on the simplified model. The mean flow velocity and geometry of the annulus used in the simulation is comparable to the real machine. The mode is a (3,0) mode with a frequency of 1510Hz.

As shown in Fig. 22 the pressure magnitude of the acoustic resonance frequency is continuously rising while closing the throttle and thereby decreasing the mass flow in the compressor respectively. At the same time the axial phase shift of the acoustic resonance over the stator row is heading towards 90°. 90° is equivalent to a wavelength of the interference wave of $\lambda/4$. As shown in Fig. 32 the wave length of the interference wave over the stator row is 0.14mm when the resonance starts and 0.18mm when the compressor stalls. 0.14mm is the distance between the trailing edge of a rotor to the leading edge of the next rotor. Because of this, it is more likely than not that the necessary resonance condition is the matching of the axial wave length with the axial spacing of the compressor stages. To put it in other words: the distance between

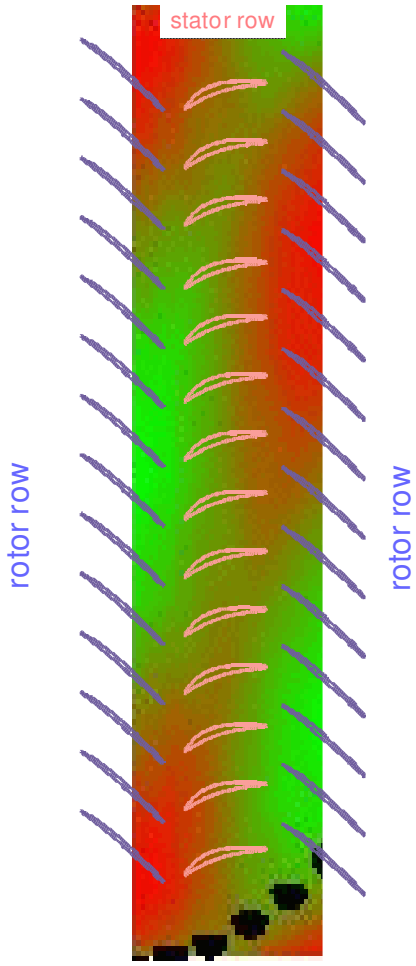

FIG. 31 PRESSURE FIELD OF INTERFERENCE WAVE BETWEEN TWO ROTOR ROWS

the reflecting rotor rows must fit to the wave length of the acoustic field formed by the superposition of the up- and downstream sub modes.

Based on these results an acoustic resonance in the compressor can be avoided if the axial spacing of the rows is extended. The resonance starts at a wave length of -14mm. At the stability limit, the wave length is -18 mm. So, if the axial distance of one rotor row to the other is extended by a factor of 18/14=1.29, the resonance will be suppressed. The actual distance is 20 mm. An extension by 30% would mean that the distance must be 26 mm. So the axial gap between each blade rows has to be extended by 30mm.

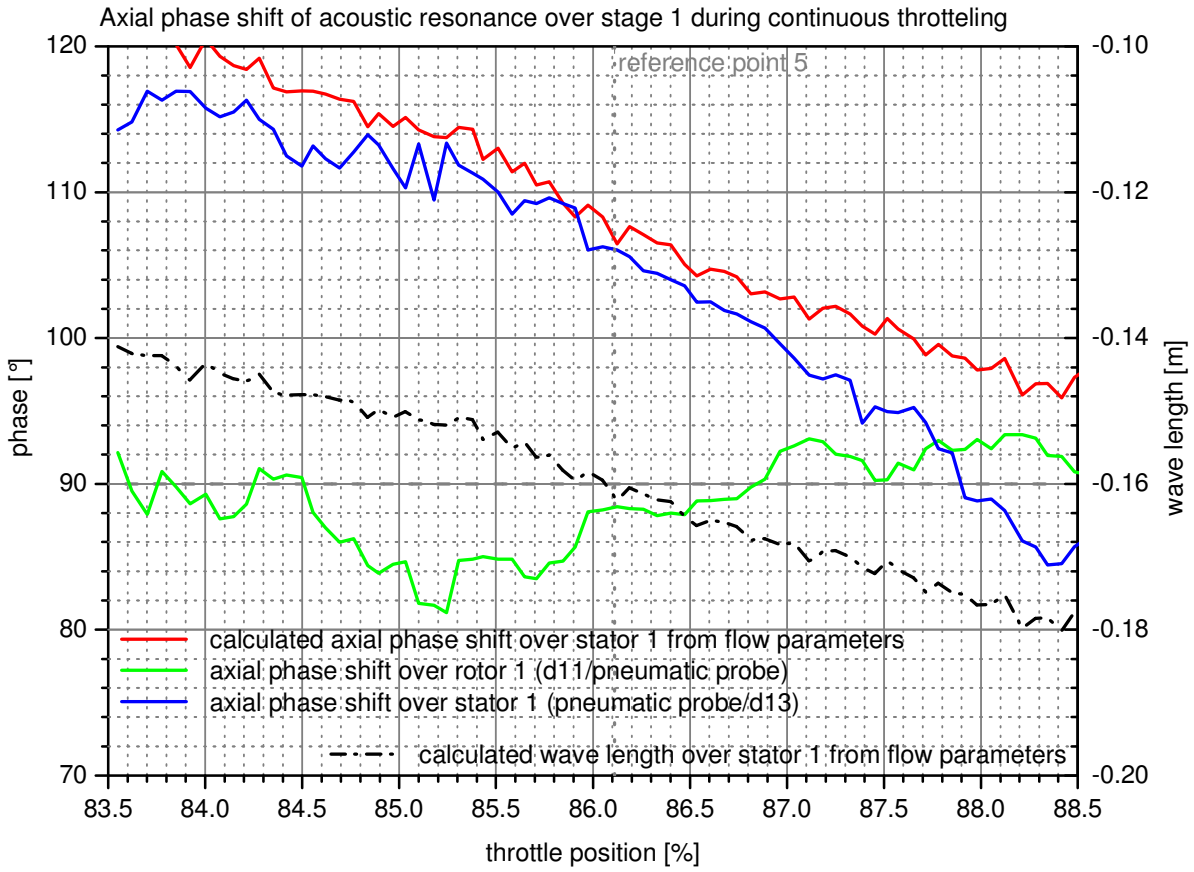

FIG. 32 MEASURED AND CALCULATED AXIAL PHASE SHIFT DURING CONTINIOUS CLOSING OF THE THROTTLE

10.6. Acoustic resonance and rotor speed

For a systematic analysis of the relation between the acoustic resonance and the rotor speed, detailed measurements of the mean flow at off-design rotor speeds under resonant conditions would be necessary. This is an important task for further investigations. Within the scope of this work, a few measurements at rotor speeds other than 0.95 were done. The results will be discussed in this section. Due to the excitation of natural modes of rotor and casing of the compressor in the speed range between 180 Hz (0.6) and 210 Hz (0.7), it is not possible to run the compressor here for a time that is sufficiently long for proper measurements. At rotor speeds below 0.6, no acoustic resonances could be detected in the compressor so far. In the speed range between 0.7 and 0.95, a second acoustic resonance with low amplitudes exists at a frequency that is again between five and six times the rotor speed (marked as AR2 in Fig. 33). In absolute values, the resonance frequency spreads from 1100 to 1300 Hz. The main acoustic resonance around 1500 Hz is excited at rotor speeds above 0.85 (marked as AR1 in Fig. 33). The phase shift around the circumference of AR2 is different to the main acoustic resonance AR1. Due to the comparatively low amplitudes of AR2, no further investigations are done in this subject.

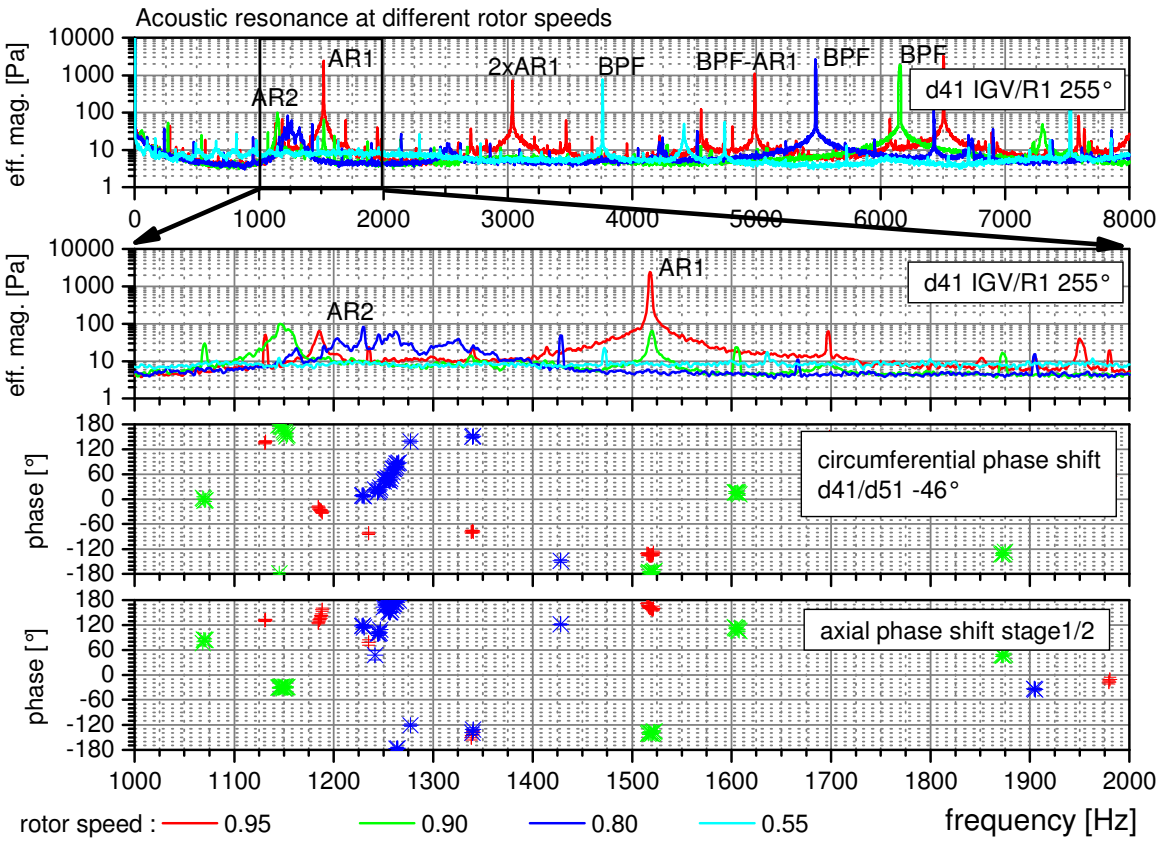

FIG. 33 SPECTRA OF ACOUSTIC RESONANCE AT DIFFERENT ROTOR SPEEDS

To investigate the dependence of the main acoustic resonance on the rotor speed systematically, a test with constant axial Mach number and variable rotor speed or a test with constant circumferential Mach number and variable rotor speed would be necessary. To realize such a test a control circuit is needed that automatically throttles the compressor dependent upon those Mach numbers that should be kept fixed. So far, such a control circuit has not been developed for and installed in the compressor.

As a more easily implemented alternative, a test at constant acceleration was performed at constant throttle position. During this test, the signal of dynamic pressure sensors in each stage of the compressor was recorded. From the mean value of the sensor signal d11 (between IGV and rotor 1) and d49 (behind stator 4 at the outlet), a static pressure ratio was calculated. The frequency spectra over the time of the dynamic pressure sensor signal d11 at 0° in front of rotor 1 is shown in Fig. 34 as contour plot. On top of the contour plot in the middle of Fig. 34, the frequency and amplitude of the acoustic resonance is diagrammed over the time. On top of that, the static pressure ratio and rotor speed is shown. At a rotor speed of about 15500 rpm (0.85) the acoustic resonance was excited at a frequency of ca. 1480 Hz. The amplitude increased with the rotor speed up to 3000 Pa at 16200 rpm (0.90) and remained in the front stages more or less constant when the rotor speed was further increased.

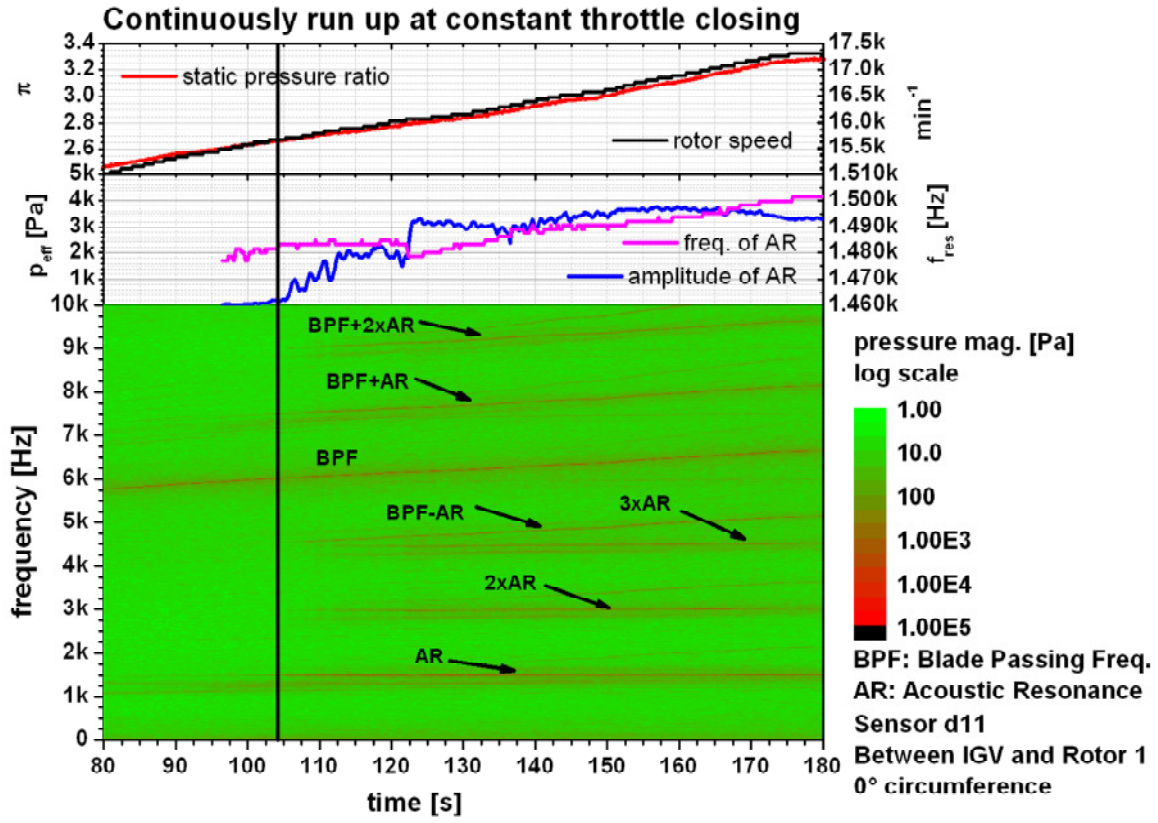

FIG. 34 INCEPTION OF ACOUSTIC RESONANCE DURING RUN UP

In the rear stages it increased further with the rotor speed (see Fig. 35). The behavior of the frequency was different. While the rotor speed increased, the frequency of the

acoustic resonance remained constant up to a rotor speed of 16200 rpm. When speed was increasing further, the frequency of the acoustic resonance also increased.

In Fig. 35 the frequency is plotted as black dashed line over the rotor speed in every diagram. Since the line is not a straight line, the frequency of the acoustic resonance is not increasing proportional to the rotor speed.

With the run up test the speed range for the excitation of the acoustic resonance was determined. From theory this speed range is limited by the incidence angles of the acoustic waves to the blade rows. If those angles do not fit, the dissipation is too high and the reflection is not high enough. To show the change of the incidence angle with the increasing rotor speed, continuous flow measurements during the run up are necessary. However, with the static pressure measurements performed here, the dependence of the incidence angles on the rotor speed could not be calculated. Because of this, the important question about the limiting incidence angles for the avoidance of acoustic resonances during the design of a compressor must remain unanswered here.

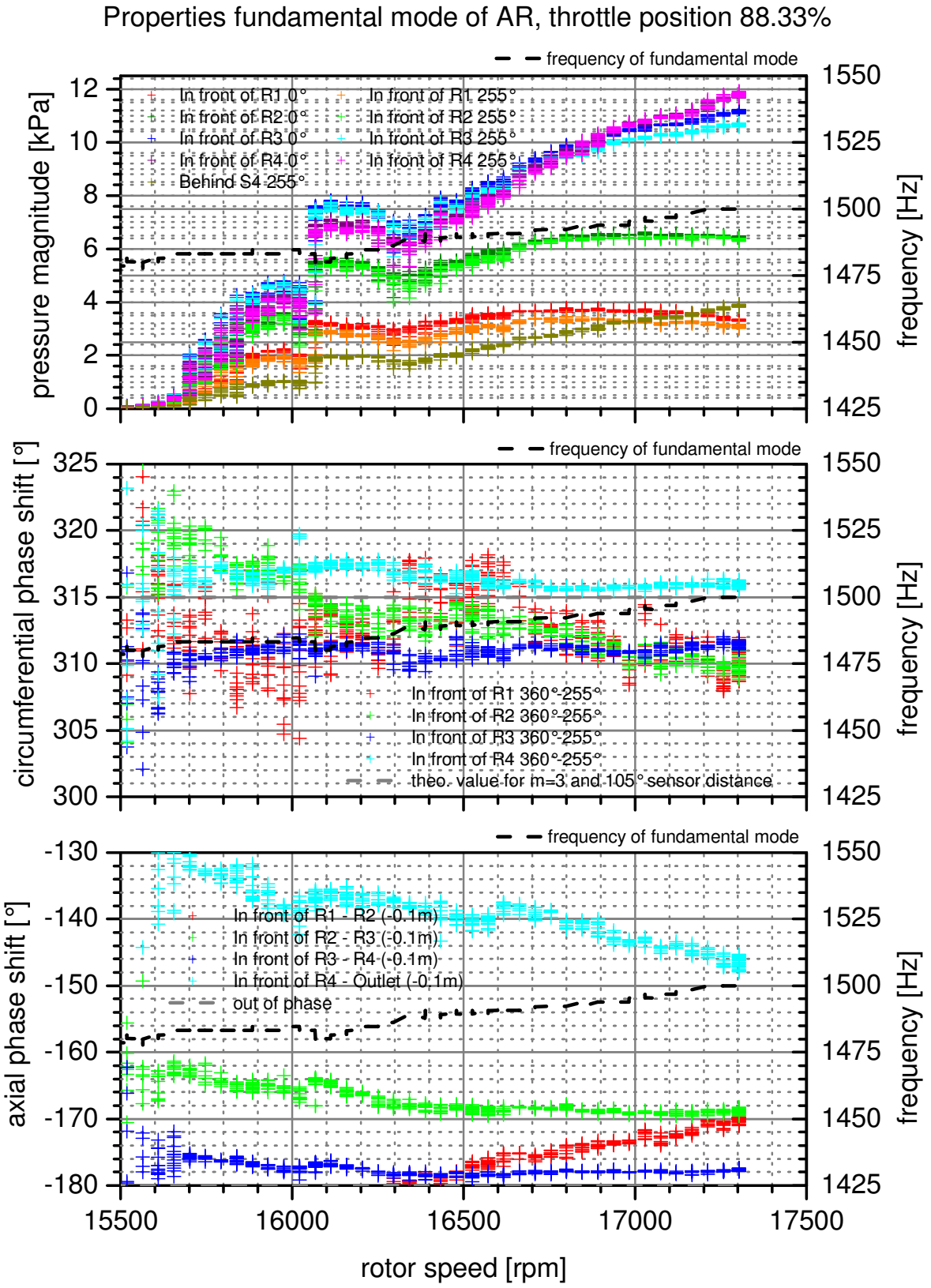

FIG. 35 PROPERTIES OF ACOUSTIC RESONANCE DURING RUN UP

10.7. Summary and conclusions of data analysis

In summary, the compressor works as resonator if the following conditions are satisfied:

1.) The incidence angle of the resonant modes relative to the blade rows must be close to their stagger angles. In the stator rows, the wave fronts must be approximately perpendicular to the blade chord. At the leading edge of the rotor rows the waves must be reflected. Because the incidence angle depends on the rotor speed, the excitation of the acoustic resonance is restricted to a certain rotor speed of the compressor. For the present compressor the measurements show that this speed range is about 0.9 to 1.0 times maximum speed. In the theory provided here, the reflection and transmission process is described qualitatively. Data of the mean flow are available for single points at design speed only. So a verification of the theory from the measured speed range is not possible within the present work. To do this, a quantitative model is necessary.

2.) The estimated values of the axial wave length from the model and the measurements coincide if only those areas between the reflection points created by the leading and trailing edge of the rotors are considered. The distance between the reflecting rotor rows must fit the wave length of the acoustic field formed by the superposition of the up- and downstream sub modes. The wave length of this acoustic field depends on the flow in the compressor, in particular on the axial Mach number of the flow. In our case, the flow rate has to be as low as possible at a high rotor speed. These are operating points close to the stability limit of the compressor.

11. Rotating Stall inception

11.1. Compressor stability

Niazi (2000) concisely summarizes compressor stability as follows:

“Stability in a compressor is the ability of a compressor to recover from disturbances that alter the compressor operation about an operational equilibrium point. Disturbances may be considered as transient or deliberate changes to the operating point. In the case of transient disturbances, the system is stable if it returns to its original operating point. If the disturbances drive the compressor away from the original point, the system is unstable. The steady state match between a compressor and its drive turbine or jet nozzle, which is perturbed by a transient change of mass-flow, is a good example of this case. When there are deliberate changes to the operating point, the performance is considered stable if a new operational equilibrium point can be achieved, e.g., shifting the operating point by changing the compressor shaft speed. If steady state operation at a new operating point is not possible, the system is unstable.
Stability in compressors may be studied from two different perspectives. The first is called operational stability, which deals with the matching of compressor performance with a downstream flow device such as a turbine or throttle. The second is aerodynamic stability, which deals with deteriorations in the operation due to flow separation, stall, or surge.
The operational stability of a compression system depends on the characteristic of both the compressor and the downstream flow device. Mathematically, if the slope of compressor performance map is less than the slope of characteristic map of the throttle the system is stable, otherwise it is not stable. Compressors, by design, usually operate on [the] rising edge of a speed line in the performance map. Operations at lower mass flow ratios can trigger instabilities as discussed later.
The stable range of operation of axial and centrifugal compressors is limited at both very high and very low mass flow rates, as shown in [Fig. 36]. If the mass flow rate is too high, shocks will form and the flow through the compressor will be choked (sonic condition). On the other hand, as the mass flow rate through the compressor decreases, flow instabilities will occur. These instabilities include rotating stall and surge. If they are allowed to persist or grow, catastrophic damage to the compressor and the engine will occur. Surge, in particular, is to be avoided at all costs.
[…] Rotating stall and surge usually occur at low flow rates, but may still occur on the right side of the surge line if the flow becomes unstable as a result of the instability. Therefore, a second line parallel to the surge line is usually introduced as a surge avoidance line. Another reason for introducing the surge avoidance line is that the compressor characteristic, and consequently the surge line, may be poorly known. Operating at the surge avoidance line provides a safety margin for the compressor operation and prevents the compressor from operating in a region where stall or surge may occur. The closer the operating point is to the surge line, the greater the pressure ratio achieved by the compressor, but the greater the risk of stall or surge.” (Modifications by the present author in [ ])

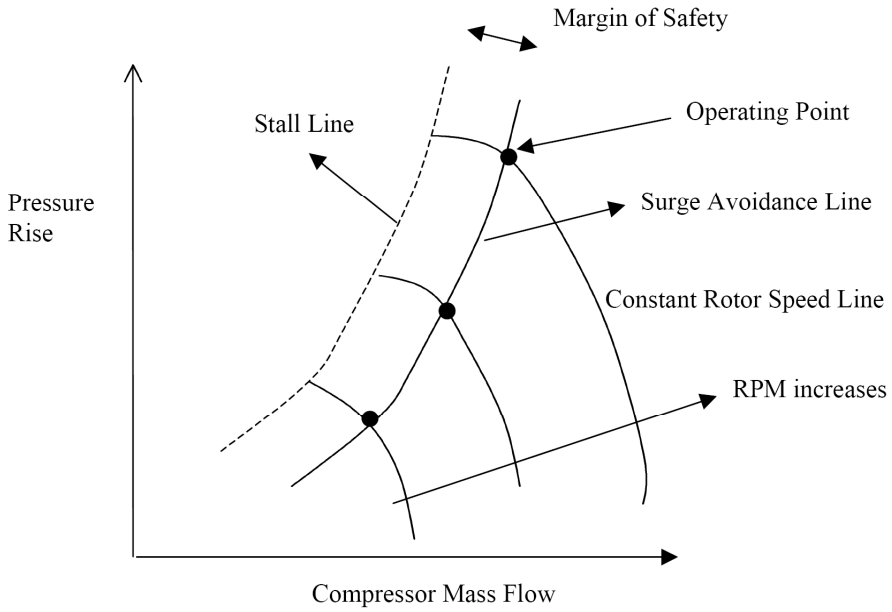

FIG. 36 EFFECTS OF ROTOR RPM ON COMPRESSOR PERFORMANCE AND STABILITY (NIAZI (2000))

11.2. Fundamentals of rotating stall

During the normal operation of a compressor, the airflow through the compressor is essentially steady and axisymmetric in a rotating coordinate system. If a flow instability is somehow introduced into the system (say, due to a change in the rotor speed, flow separation at the inlet, or other type of flow distortion), instabilities may develop and the compressor performance may deteriorate. The instability manifests itself as either a rotating stall or surge. Rotating stall is inherently a 2-D unsteady local phenomenon in which the flow is no longer uniform in the azimuthal direction. It often takes only a few seconds for rotating stall to build up, sometimes even less than a second, and the compressor can operate under rotating stall for several minutes before damage develops. In some radial compressors and some test facilities operation under rotating conditions is possible for hours. This depends mainly on the mechanical design of the compressor.

Rotating stall can occur in both compressible and incompressible flow. It is not known for certain why all blades do not stall at the same time. Dimensional tolerances are one possible explanation. In manufacturing and assembly, a few blades could be produced with slightly different profiles or with higher stagger angles or assembled such that the flow cross-section of the passages varies. Another possibility could be that the inlet flow is non uniform e.g. due to supporting struts in the compressor inlet. Besides, even in a perfect compressor with totally uniform inlet flow, the flow in the compressor is from an unsteady point of view always non uniform in circumferential direction due to the rotation of the rotor. So this non uniform flow causes the inlet air to see blades at

slightly different angles of attack as compared to the other blades. When one of the blades stalls, the angle of the flow increases relative to the shaft as a consequence of some instability as shown in fig. 37. In addition to the blockage caused by the stall, this increase in flow angle causes part of the oncoming flow to be diverted towards the neighboring blades, thus causing an increase in their angles of attack and leading them to stall. As the blade rotates away from the disturbances, the angle of attack decreases restoring normal flow over that blade. The region of the stalled flow, known as a stall cell, continues moving from blade to blade and propagates around the annulus. In a coordinate system attached to the blades, rotating stall moves in a direction opposite to the blade motion at a fraction of the rotor speed. However, in the inertial coordinate system, the stall region propagates in the same direction as the wheel motion. The reported rotational speed of rotating stall around the annulus of compressor varies from 20 to 75 percent of the rotor speed in the direction of the rotor motion. It has also been reported that the incipient rotating stall cells move faster, although never faster than rotor speed. This is due to the fact that in the relative frame of the blades, the stall has to move against the direction of rotor rotation.

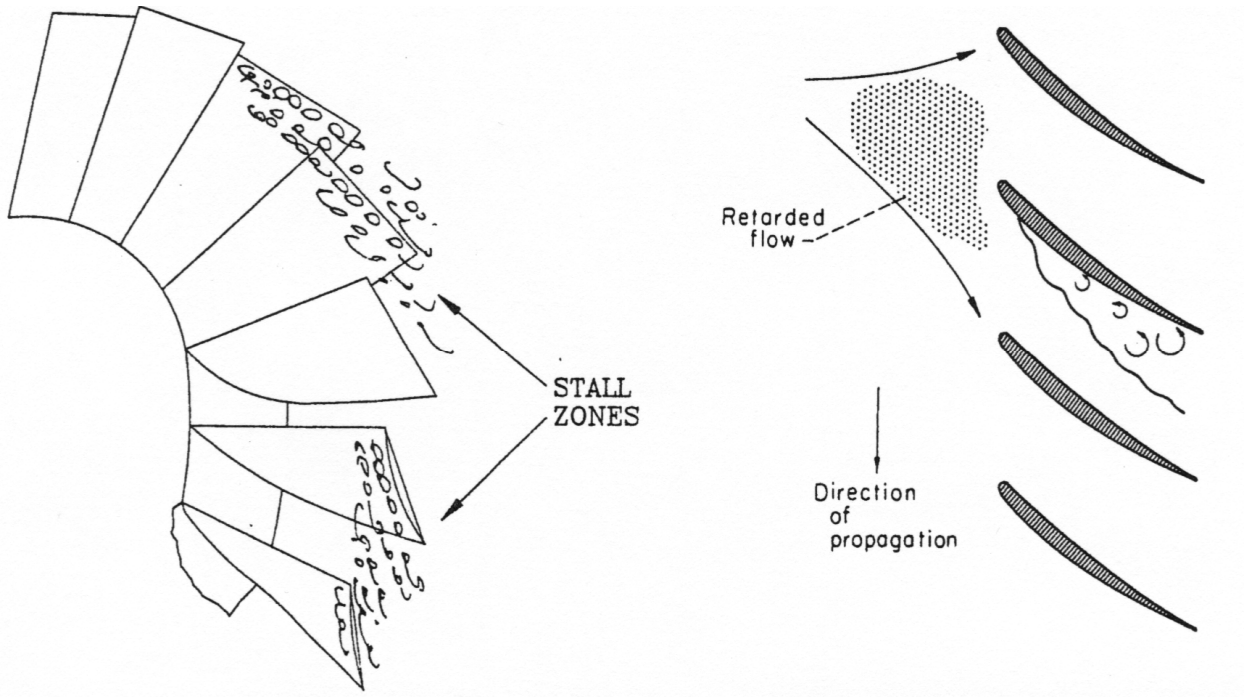

FIG. 37 ILLUSTRATION OF ROTATING STALL ON AN AXIAL COMPRESSOR ROTOR (LEFT) AND PROPAGATING STALL IN A CASCADE (RIGHT) TAKEN FROM PAMPREEN (1993)

The number of stall cells depends on the compressor at hand; one to nine stalled cells have been reported. Two types of stall associated with the number of stalled cells exist, progressive and abrupt. In progressive stall, a phenomenon involving multiple stalled cells, the pressure ratio after stall reduces gradually. Abrupt stall results in a sudden drop in total-to-total pressure rise, and appears to always involve a single stalled cell. One of the characteristics of pure rotating stall is that the average flow is steady with respect to time, but the flow has a circumferentially non-uniform mass deficit. During rotating stall, the cyclical variation of the pressures on the blades can cause them to fatigue and eventually break. Due to uneven shaft work bearings might be overloaded and shaft vibration increases. The flow temperature may also increase for this reason and reduces blade life.

Several types of rotating stall exist:

- **Part-Span**: As illustrated in the upper sketches in Fig. 38, only a restricted region of the blade passage, usually the tip, is stalled. Stall near the root, called corner stall, has also been reported.

- **Full-Span**: The entire height of the annulus is stalled. The lower sketches in Fig. 38 show the full-span rotating stall with various stalled cells.

- **Small/Large scale**: In this case, a small/large part of annular flow path is blocked.

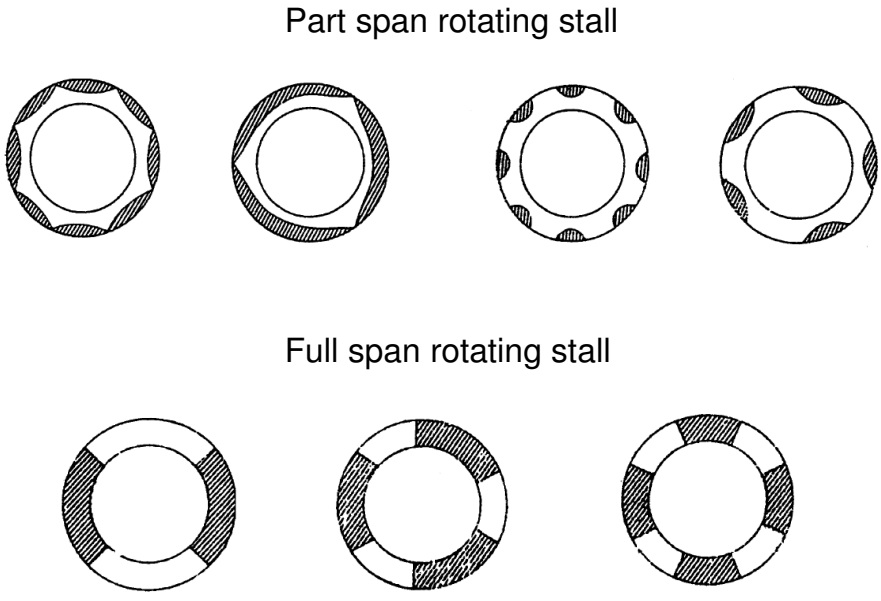

FIG. 38 TYPES OF ROTATING STALL (PAMPREEN (1993)).

(shaded areas are stalled)

When rotating stall occurs at a point on the unstalled branch of a speed line, the operating point proceeds to the so-called stalled characteristic. This characteristic is characterized by a lower pressure ratio at the same mass flow and rotor speed. Sometimes the deterioration in the performance of an axial compressor with rotating stall is small and may not be easily detected, except as an increase in the compressor noise or by some dynamic pressure or vibration sensors. Recovery from rotating stall is often more difficult than surge, because the mass flow needed for recovery from stall is higher than the mass flow where the stall occurs. Rotating stall can also serve as the precursor to the more severe and dangerous surge.

Surge is a global 1-D instability that can affect the whole compression system. Surge is characterized by large amplitude limit cycle oscillations in mass flow rate and pressure rise. Even a complete reversal of the flow is possible. The behaviour of surge depends on both, the compressor characteristic and the characteristics of the diffuser. In contrast to rotating stall, the average flow through the compressor is unsteady. In theory the flow is circumferentially uniform but in practice this is probably not the case. Anywhere this is not a point of great interest because surge is to be avoided at all costs.

Due to the low volume between the compressor outlet and the throttle in the test rig in the present work, surge cannot occur. When the compressor stalls and so the outlet pressure decreases, the amount of pressurised fluid between the compressor outlet and throttle is too small to initiate a reverse flow in the compressor annulus. This special design feature allows investigations in rotating stall without the risk of damaging the compressor by surge.

11.3. Stall inception in the TFD compressor

11.3.1. Diffusion coefficient

To get an idea of the aerodynamic loading of the compressor, the local diffusion coefficients have been calculated based on steady flow measurements by Reißner and Seume (2004). They are shown as function of the radius of the annulus in Fig. 39. Following Cumpsty (1989) the diffusion coefficient DC is defined as:

$$DC = 1 - \frac{c_{\text{out}}}{c_{\max}} \tag{64}$$

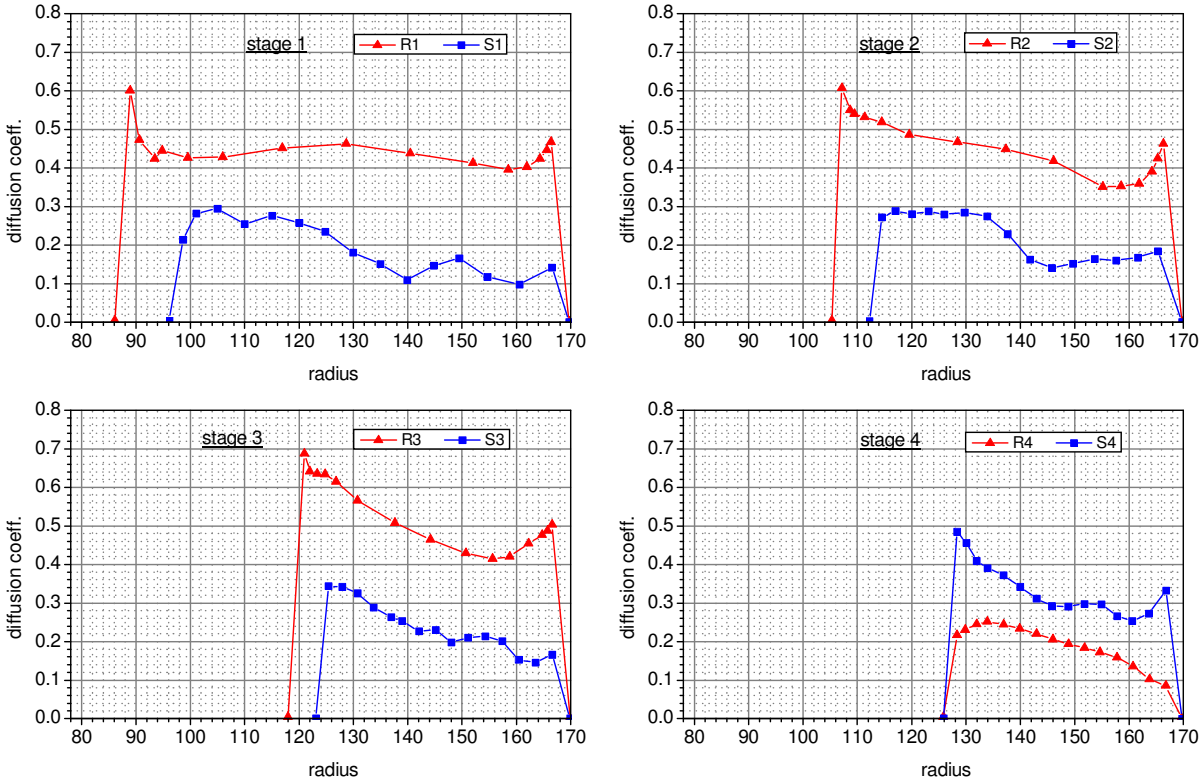

FIG. 39 DIFFUSION COEFFICIENT OVER COMPRESSOR ANNULUS RADIUS (REISSNER AND SEUME (2004))

The diffusion factor increases with the deceleration of the fluid. So if the diffusion coefficient is high the loading is high as well. The Fig. 39 shows that the coefficients for the rotors are typically higher than those for the stators and that they have higher loading at the hub and tip than at mid span. The loading in the first three stages is quite similar but the highest loading is in the hub region of the third stage. From this analysis the compressor should stall in this region first, however the results of unsteady measurements in the next subsections show different results.

11.3.2. Axial detection of the rotating stall origin

As already mentioned in Chapter 8, the TFD compressor is changing from stable operation to stall condition in less than half a second. It is possible to run the compressor close to the stability limit for hours and not withstanding, closing the throttle only half a percent drops the compressor immediately into rotating stall. With a simultaneous measurement of dynamic pressure transducers it is possible to localize the origin of rotating stall. Fig. 40 is a zoom into the time series data near the time where the instability occurs. The compressor was operating close to the stability limit when the throttle was closed by another 0.3%. This caused a rotating stall within 0.26s. The data shown are the AC part of the signal normalized by the standard deviation of the signal during normal operation in the point of best efficiency. The sensors for these signals were mounted in a straight axial line on the top of the compressor. There was nearly no time shift between the signals in the onset of the stall. When the stall was established also no time shift between the signals was noticeable. The minimal time shift in the onset of stall between the signals from the first and second stage to the last stage was about 0.2 ms. This means that, in the ideal case, a stall cell growing from the first stage to the last stage, which is 400 mm further down, has to expand with a speed of about 2000 m/s. This is physically impossible. So, when the compressor stalls, the stall cells occur in every stage at the same time with one stall cell around the circumference rotating in a nearly straight axial line around the compressor. This type of stall inception has been observed several times in a similar way on this compressor.

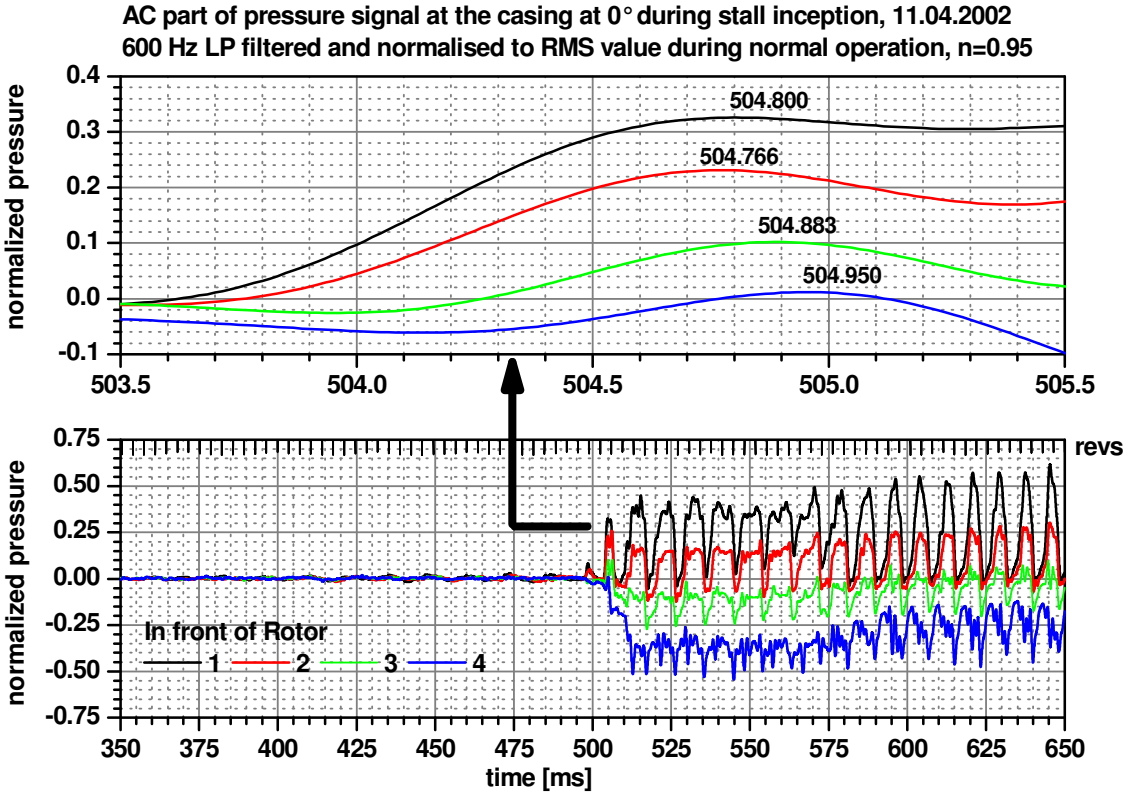

FIG. 40 ROTATING STALL INCEPTION AT DIFFERENT AXIAL POSITIONS CASE 1

There is also another type of inception at the same rotor speed shown in Fig. 41. Here the stall is shifted from stage to stage by almost 180°. This means that the stall in the first and third stage occur nearly at the same time while in the second stage it is measured with an delay of approximately half of the cycle duration of the established stall. This does not necessarily mean that the inception in this stage is delayed. It is also possible that stall inception in this stage occurs at the same time but on the opposite side on the circumference relative to the neighboring stages. Unfortunately no circumferentially distributed sensors in all stages have been installed in this measuring campaign. The main difference between these measurements and those in Fig. 40 are the stator blades in the rear stages. In the first case, the compressor was equipped with its reference blades and in the second cases with bow blades. However, whether this is the reason for the different behavior has not been examined so far.

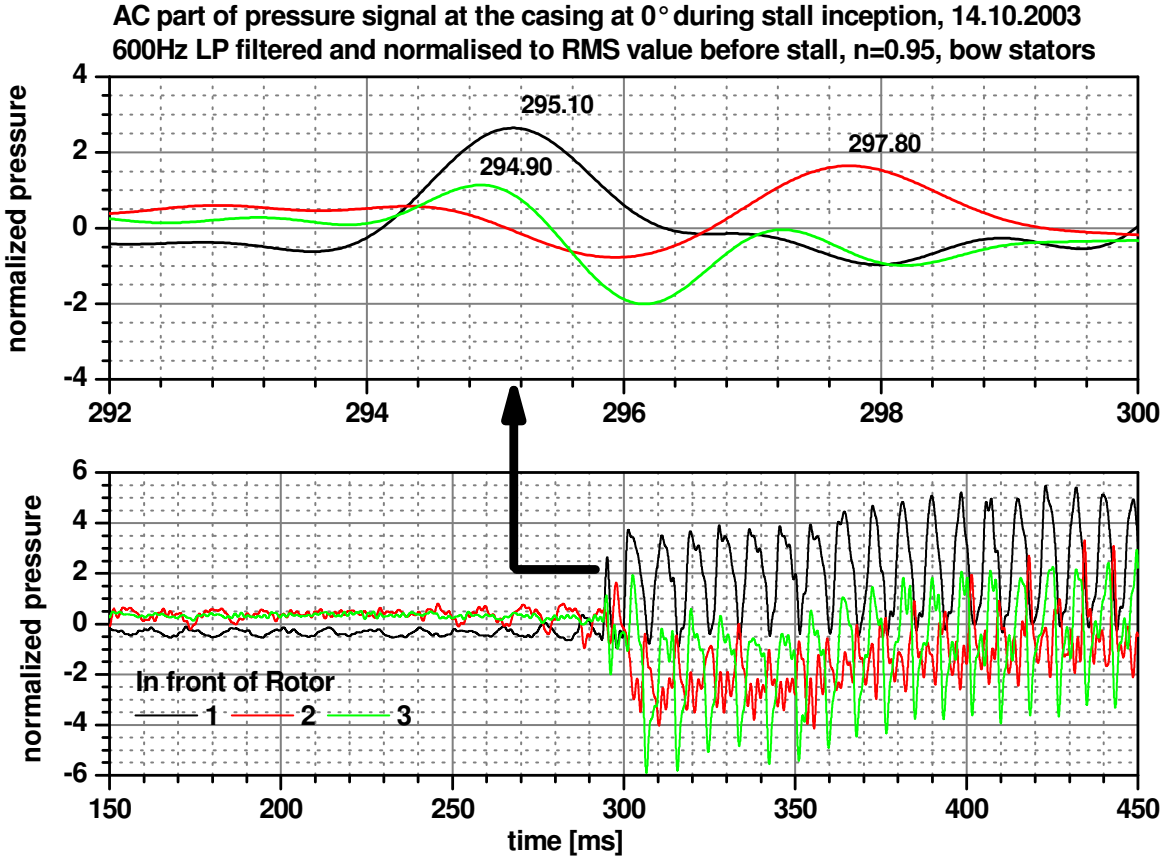

FIG. 41 ROTATING STALL INCEPTION AT DIFFERENT AXIAL POSITIONS CASE 2

The third case of stall inception appears at low rotor speeds where the behavior is very different. As will be discussed later, here the compressor has a spike type stall inception. As shown in Fig. 42 the spikes are seen first in the front stage. The point where the stall starts is not so clear anymore, yet, after the onset of stall, the axial shift of the stall cells is similar to case two.

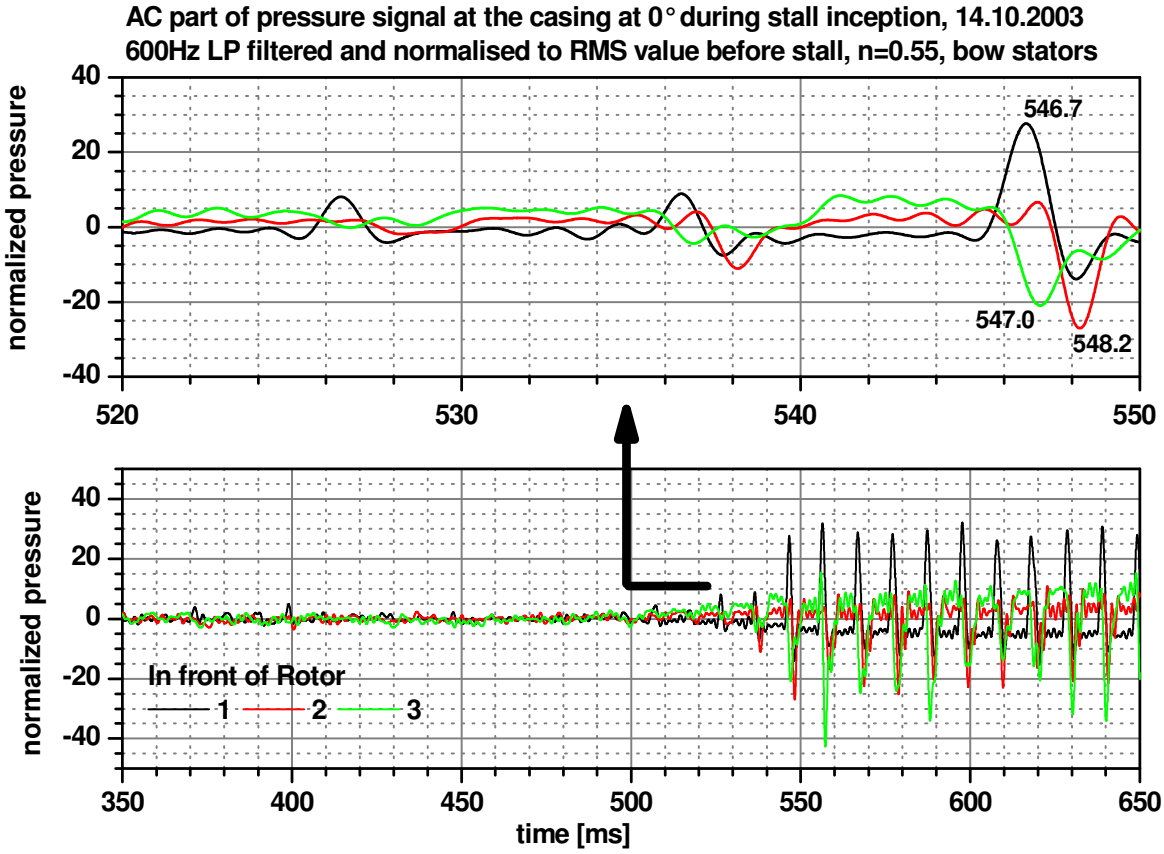

FIG. 42 ROTATING STALL INCEPTION AT DIFFERENT AXIAL POSITIONS CASE 3

The inception of the stall close to the stability limit in the time data is shown in Fig. 43. About 50 revolutions before the stall occurs, a pressure fluctuation of about 78 Hz becomes visible in the data of the sensors in the first stage and later in those of the second stage as well. The red dashed lines are indicating intervals of 12.8 ms corresponding to a cycle duration of a 78 Hz oscillation. The physical origin of the 78 Hz stall precursor is not precisely known. In Hellmich et al (2002) a connection to the matching of rotor and stator blades during one revolution is discussed as reason for the 78 Hz pressure fluctuation. In any case, the time lag from the first noticeable cycle of this fluctuation to the onset of stall is too short to use it as a reliable stall precursor.
More important is the fact, that this fluctuation is seen mainly in the first and second stage and that the stall occurs in phase with the fluctuation in the first stage. This indicates that the first or the first two stages are playing an important role in stall inception.

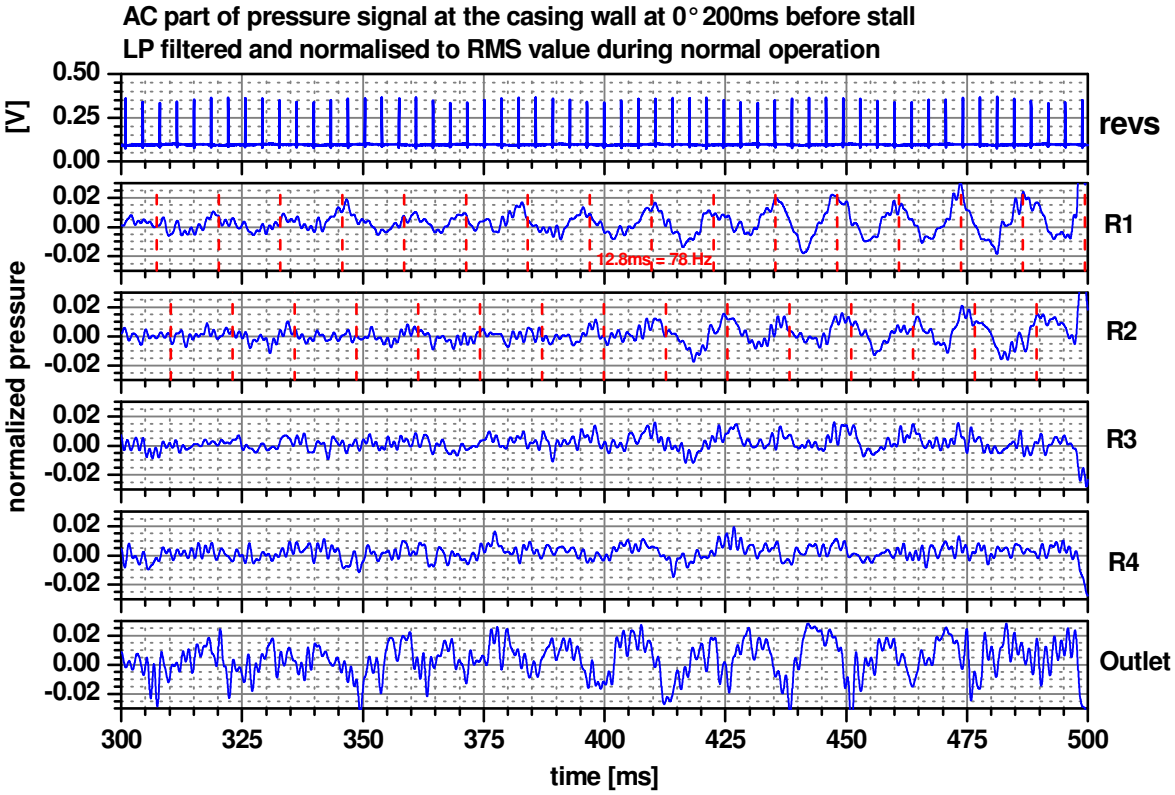

FIG. 43 TIME SIGNAL CLOSE TO THE ROTATING STALL

11.3.3. Radial detection of the rotating stall origin

For the detection of the radial position of the stall origin, the dynamic four-hole pneumatic probe was inserted in the compressor between Rotor 1 and Stator 1 and between Rotor 2 and Stator 2. The measurements were carried out at five positions in each channel. In each position, the throttle of the compressor was closed in five steps of about 25 s length from the design point to the stability limit. To compare the different measurements, the time data of each measurement has been shifted in time, such that the first stall-related step of the wall pressure at sensor d11 (0°, in front of Rotor 1) occurs at the same time in each data set. Each data set is taken with the throttle at its maximally closed position. Fig. 44 shows that the rotating stall occurs - within the accuracy of this method – at all radial measurement positions at the same time. Thus, no statement about the origin of the stall could be deduced from the time shift of the stall. However, the data at 86.8% channel height behind rotor 1 and at 66.2% behind rotor 2 show that precursor pressure fluctuations occur (Boxes in Fig. 44). This indicates that the stall occurs in the upper part of the channel near the blade tips.

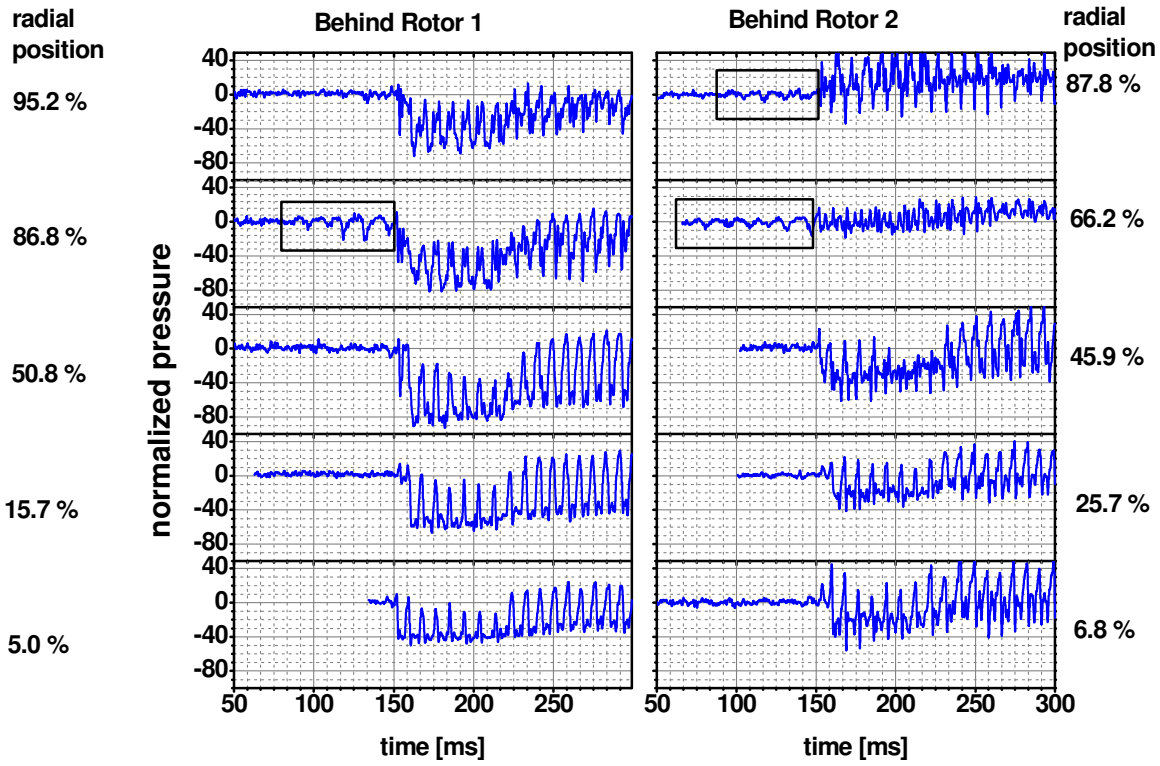

FIG. 44 TOTAL PRESSURE SIGNAL OF STALL IN DIFFERENT RADIAL POSITIONS

11.3.4. Circumferential detection of the rotating stall origin

In circumferential direction, the onset of rotating stall has not been investigated intensively. Nevertheless, in the over thirty measurements a rotating stall was never measured with the onset of stall between sensor d41 and d11. In all cases the stall was first detected at position d41. Sensor d11 is on the twelve o'clock position (0°) on the top of the compressor and sensor d11 is on the eight thirty position (255°) looking in the direction of the axial flow. One measurement was performed with a sensor at position d21 on the two thirty position (70°) in front of the first rotor. The onset of stall in this measurement is shown in Fig. 45. Again the stall was detected at sensor d41 first. So it is assumed that the stall in the TFD compressor starts in the lower half of the compressor between 70° and 255°.
There are several effects causing small circumferential asymmetries in a compressor. For example, one explanation could be that the shaft runs in a journal bearing which is not in the centerline. This causes slightly different gaps between the blade tips and the casing. Also the casing itself might lack a perfect circular shape. Last but not least there are three supporting struts for the front bearing in the lower half of the compressor causing flow distortions.
One or even more of these effects might trigger the stall so that it started in the lower half of the compressor.

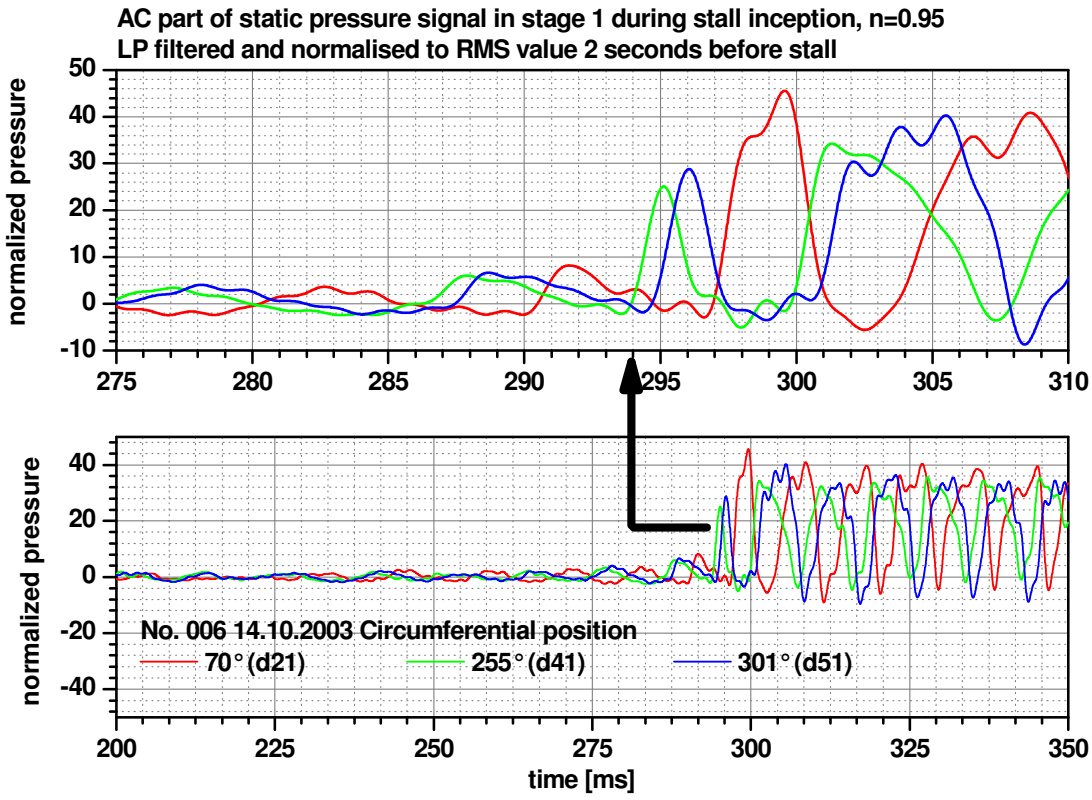

FIG. 45 ROTATING STALL INCEPTION AT DIFFERENT CIRCUMFERENTIAL POSITIONS

11.3.5. Stall inception at different rotor speeds

So far the data of rotating stall measurements shown here are taken at a rotor speed of 0.95. For other rotor speeds close to 0.95, the behaviour of the compressor is quite similar while it becomes different at a speed of 0.55. This will be discussed in the frequency analysis in the next chapter more in detail. But even in the time series analysis one can see the differences. Low frequency pressure fluctuations around 70 Hz were found at high rotor speeds between 0.8 and 1.0 just before the compressor stalls and a spike type stall inception was found at a low rotor speed of 0.55 (Fig. 46). Relative to rotor speed the low frequency pressure fluctuations have a frequency of 0.25 times rotor speed (see Fig. 47).
A spike type stall inception is typical for compressors with a local aerodynamic overloading. In contrast, a modal wave type stall inception is typical for compressors with an overloading of the whole compressor (or at least an overloading of a complete stage). So, if a high speed compressor runs far away from its design speed the stage matching is not optimal anymore. This causes an overloading in the first stage and small stall cells are running through the compressor seen as spikes in the pressure signals.

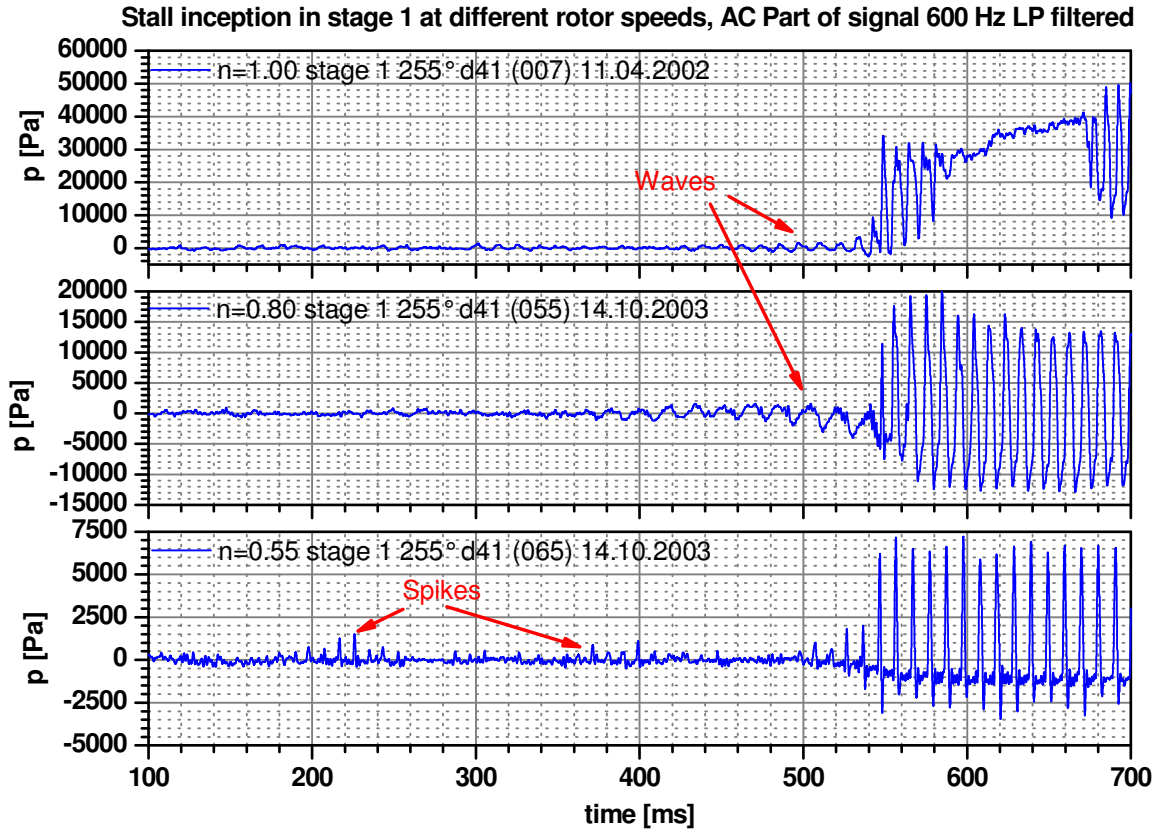

FIG. 46 STALL INCEPTION AT DIFFERENT ROTOR SPEEDS

11.4. Frequency analysis of rotating stall measurements

To answer the question how many stall cells are rotating around the circumference, a cross correlation function in the time domain or coherence and phase functions in the frequency domain could be used. Because a rotating stall is a periodic phenomenon, a frequency analysis is useful for the analysis of an established stall. It delivers rotation frequency and phase shifts between multiple sensors directly and more importantly, it is useful for the detection of modal waves as stall precursors that are hidden in the signal background.

11.4.1. Magnitudes at different rotor speeds

The frequency spectra of static pressure signals taken from sensor d41 in the first stage of the compressor are shown in Fig. 47. On the left hand side are spectra of signals measured 1.5 s before stall and on the right hand are spectra of the same sensor signal during stall. Each line shows data taken at different rotor speeds. While for the speeds 1.0, 0.95, and 0.8 the behaviour of the compressor is quite similar, it is different at a low speed 0.55. At high speeds, the stall always has the same rotation frequency relative to the rotor speed. So the propagation velocity of the stall cells on the rotor is in all three cases the same. In Hellmich et al. (2003), a clocking effect of the rotor and stator blades is discussed as a reason for this behaviour.

The spectra taken from the signals before stall show the results we already found in the time domain. There is a wide peak around 70 Hz in the spectra caused by the fluctuation we found in the time series of the signals just before stall. Even if this fluctuation has a frequency that is slightly different for different rotor speeds, again the behaviour at high speeds is quite similar compared to those at the lower speed of 0.55.

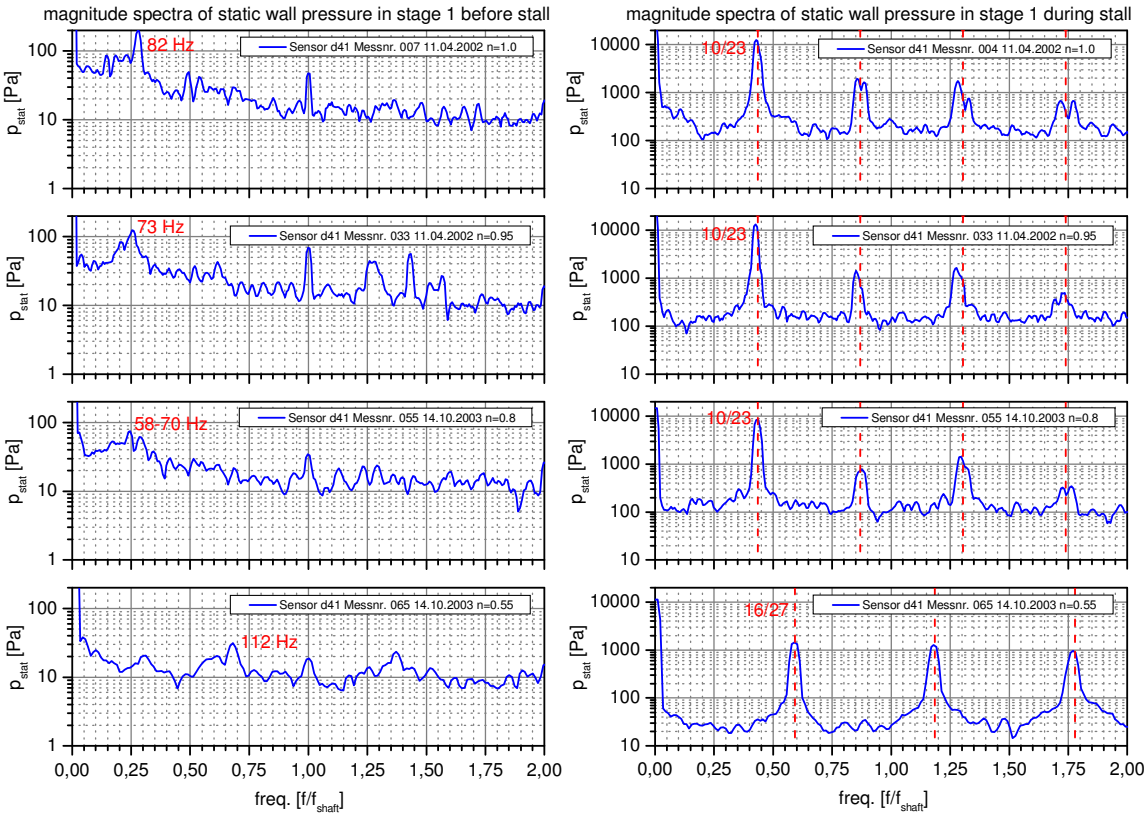

FIG. 47 FREQUENCY SPECTRA OF STATIC PRESSURE SIGNAL IN STAGE 1 1.5 SECOND BEFORE STALL AND DURING STALL

11.4.2. Phase and Coherence at different rotor speeds

The number of stall cells around the circumference can be estimated with a phase and coherence analysis. The signal caused by a stall cell passing two sensors distributed around the circumference of the compressor has a high coherence at the rotation frequency of the stall. So the phase shift between the signals at this frequency can be estimated with a low statistical error. For a stall with just one cell around the circumference, the phase shift is the same as the distance of the sensors around the circumference of the compressor. The preceding sign of the phase indicates the direction of rotation. With regard to this, for two sensors mounted at 255° and 360° on a scale counting in direction of rotation of the shaft, the distance is 255°-360° = -105°. The phase shift at the rotation frequency of the stall has the same value, i.e. it is a one cell rotating stall. If the preceding sign of phase would be opposite it would not be a rotating stall or it would be a multi-cell rotating stall. In the first case, this is because the propagation of the pressure fluctuation is against the rotation of the shaft and in the second case, because the phase shift in the pressure signal of a multi-cell rotating stall is the distance of the sensors around the circumference multiplied with the number of stall cells. In our example, a two cell rotating stall would cause a phase shift of -105°·2=-210°. If the phase is calculated in a range from -180° to 180° a value -210°

corresponds 360°-210°= 150°. This has to be taken into account when the phase function is used for the detection of stall cell numbers.

In Fig. 48, the magnitude phase and coherence functions over the frequency are shown for rotating stall at different rotor speeds. The upper diagrams show the speeds of 1.0 and 0.95 calculated with the sensors d11 and d41 which are -105° apart (cf. Fig. 5 and table 2, page 11). The lower ones show the speeds of 0.8 and 0.55 with the sensors d51 and d41 which are -46° apart (cf. Fig. 5 and table 2, page 11). All signals are taken from the first stage of the compressor. Because the pressure profile of a stall cell has more a rectangular than a sinusoidal shape, the stall has several higher harmonics in the spectra at multiples of its rotation frequency. The phase shift of the higher harmonics is also a multiple of the phase shift at the fundamental frequency.
In table 6, the rotation frequency and estimated phase shifts at the peak values of the measured magnitudes in Fig. 48 are summarized. The rotation frequency of the stall f is given as an absolute value in Hz and as a fraction of the rotor speed. The pressure values p_x and p_y are the peak values of the magnitude. h is the index of the harmonic order and δ is the circumferential distance of sensor x and y. θ_{xy} and γ^2 are the values of the phase and coherence function for the frequency f, respectively.

f [Hz]	f [n]	p_x [Pa]	p_y [Pa]	$\gamma^2(f)$	$\theta_{xy}(f)$ [°]	$\sigma(\theta_{xy}(f))$ [°]	h	$\delta \cdot h$ [°]	$(\theta_{xy} - \delta \cdot h)/h$ [°]
n=1.0 (304 Hz)									
132	0.434	13498	19160	0.996	-117.99	0.44	1	-105	-13.0
264	0.867	2835	5090	0.939	109.97	1.80	2	150	-20.0
396	1.301	1957	2167	0.883	52.14	2.57	3	45	2.4
535	1.759	1082	1427	0.866	-74.36	2.78	4	-60	-3.6
n=0.95 (288.05 Hz)									
125	0.432	13327	19134	0.998	-118.09	0.26	1	-105	-13.1
249	0.865	2099	4275	0.938	98.49	1.52	2	150	-25.8
374	1.297	2155	2231	0.897	43.58	2.00	3	45	-0.5
505	1.754	994	1170	0.779	-101.48	3.15	4	-60	-10.4
n=0.8 (242.95 Hz)									
103	0.422	3232	3748	1.000	-50.67	0.19	1	-46	-4.7
212	0.874	434	480	0.898	-131.90	2.91	2	-92	-20.0
315	1.296	614	794	0.968	-129.38	1.58	3	-138	2.9
425	1.749	205	219	0.484	165.32	8.92	4	176	-2.7
n=0.5 (164 Hz)									
95	0.581	520	486	0.996	-38.03	0.61	1	-46	8.0
190	1.161	473	536	0.997	-87.48	0.56	2	-92	2.3
293	1.786	378	427	0.995	-138.58	0.70	3	-138	-0.2
388	2.367	234	256	0.978	174.98	1.43	4	176	-0.3

TABLE 6 ROTATION FREQUENCY AND PHASE SHIFTS OF ROTATING STALL

The measured values show that in all cases estimated phase shifts fit a single cell rotating stall. The differences between the measured values and the expected values $\delta \cdot h$ is caused by a non-uniform rotation speed around the circumference and changes with form and size of the stall cell during the time the stall cell passes from one sensor to the other.

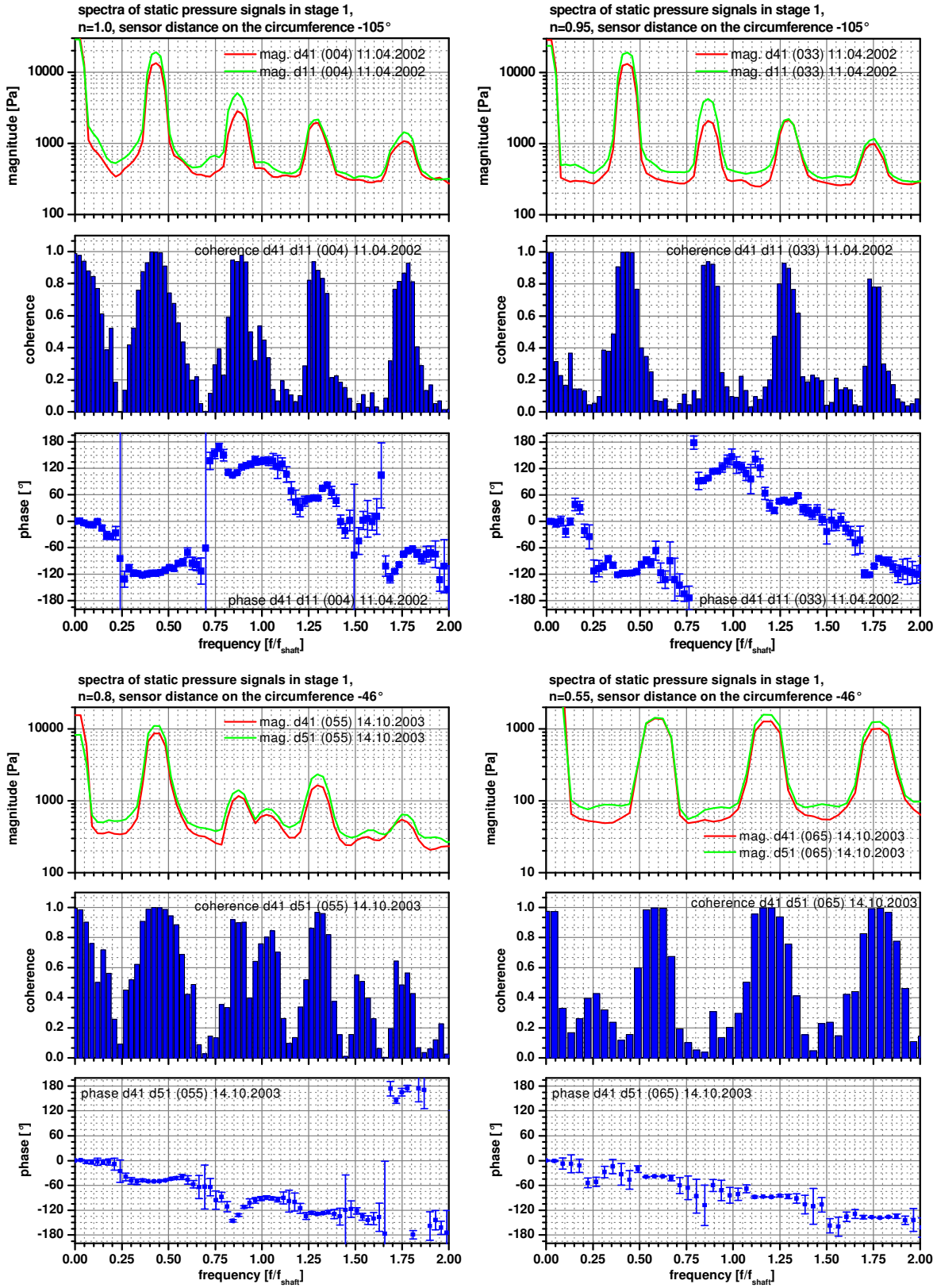

FIG. 48 SPECTRA OF STATIC PRESSURE SIGNALS IN STAGE 1 DURING STALL

As the TFD compressor stalls at constant rotor speed very precisely at the same mass flow rate, it is possible to run the compressor very close to this limit for at least a couple of minutes. This makes it possible to perform in this operating point long term measurements that can be used for frequency analysis with high frequency and amplitude resolution. This way, even small periodic fluctuations in the signal background were found. For example, such a fluctuation was found between 70 and 80 Hz just before the compressor stalled in the time series of the dynamic pressure signals. However, it could also be found earlier in the spectra of the same signals. Fig. 49 show spectra similar to those of the rotating stall in Fig. 48, but now for the same signals in the last stable point on the performance map before the compressor stalls. Due to the long measuring time, the frequency resolution in Fig. 49 is higher than in Fig. 48 and Fig. 47. The 70-80 Hz fluctuation causes a wide peak in the magnitude and coherence spectra at 1.0 and 0.95 rotor speed. The phase shift in this frequency range is the same as the phase shift of the stall. So, the measured fluctuations have the same behavior as a rotating stall except that the measured pressure fluctuations are lower in magnitude by a factor of about 100. Because the measured frequency is lower than that of the following deep stall, the relative speed of the fluctuation in the rotor frame is higher. This leads to the conclusion that this pre-stall phenomenon is a mild single-cell part span rotating stall.

For a rotor speed of 0.8 the results are not as obvious. At the last stable point that was measured (shown in Fig. 49), there is no noticeable peak around 70 Hz. The reason might be that this point was too far away from the real stability limit. In the spectra in Fig. 47, which was taken from data just before the compressor stalled, a pressure fluctuation around 60 Hz was detected. The phase spectra for these data are not shown here but the phase shift between the sensors d41 and d51 at 58 Hz is close to zero. So, for a speed of 0.8, the pre-stall behavior is similar to the rotor speed of 0.55. At this speed, there are coherent pressure fluctuations with frequencies lower than the rotor speed, but they are all in phase around the circumference. This means that they do not belong to a mild rotating stall.

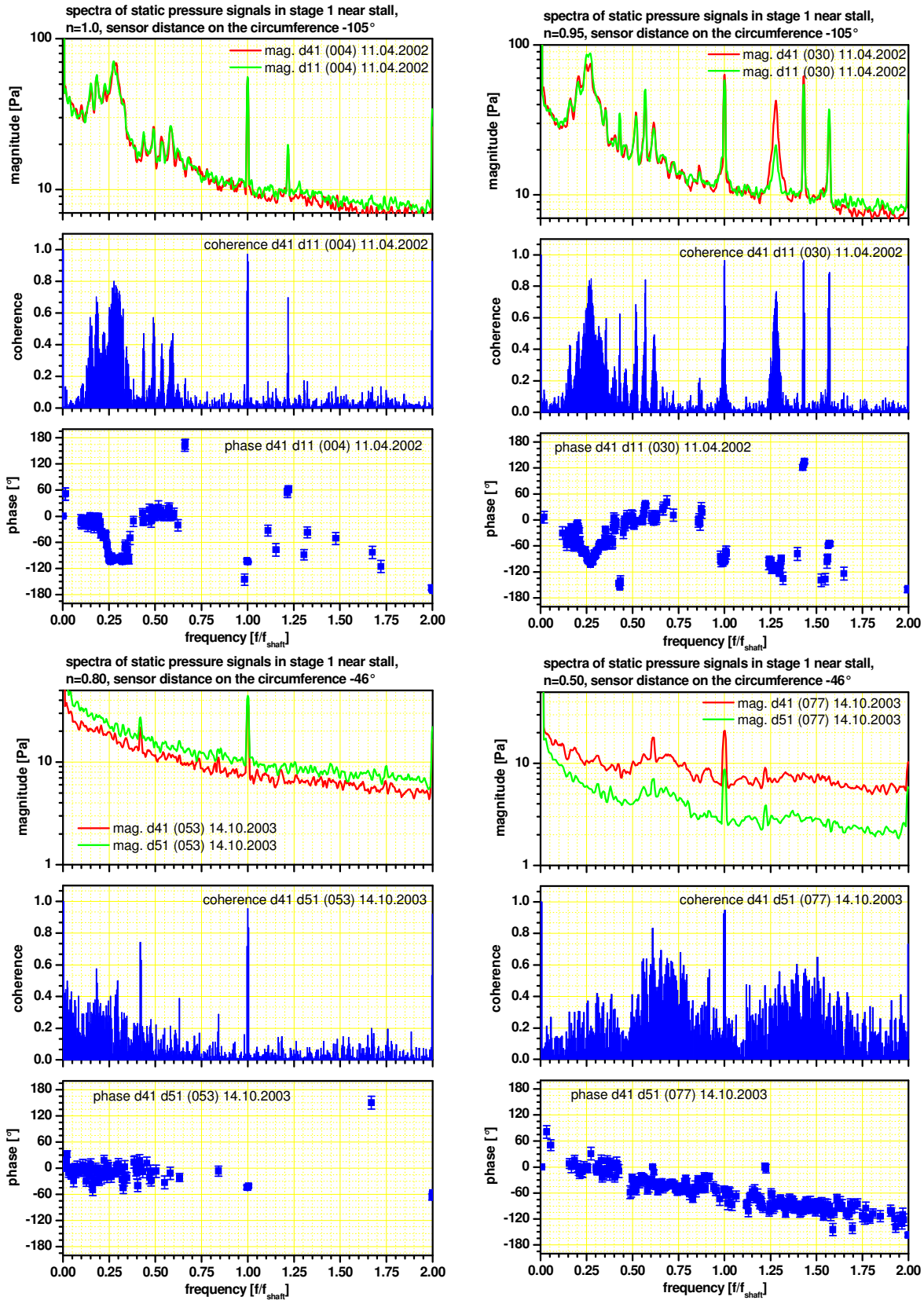

FIG. 49 SPECTRA OF STATIC PRESSURE SIGNALS IN STAGE 1 CLOSE TO STALL

11.5. Summary of rotating stall inception

The results of the rotating stall measurements are summarized as follows:

1. The stall margin in the performance map of the compressor and the pre-stall behavior of the compressor are highly reproducible.
2. The onset of stall in axial and radial direction starts in all stages nearly at the same time.
3. In circumferential direction the onset of the stall is not precisely known. But in most cases the stall was detected in the lower half of the compressor between three o'clock (90°) and nine o'clock (270°) position.
4. At high rotor speeds, the stall in all stages is nearly in phase (0°) or 180° out of phase. At a rotor speed of 0.55, it has a phase shift from stage to stage of between 0° and 180°.
5. At rotor speeds close to the design speed (n_{norm} = 0.8 … 1.0), the compressor shows a modal wave type stall inception while at low speeds (n_{norm} = 0.55) there is a spike type stall inception.
6. For high normalized rotor speeds of 1.0, 0.95, and 0.8, the rotation frequency of the stall in the rotor frame is the same while it is different at a normalized rotor speed of 0.55.
7. In all cases, the measured stall is a single cell full span rotating stall.
8. For a rotor speed of 1.0 and 0.95, modal waves were detected in the last stable operating point on the performance map of the compressor. These modal waves behave like a mild single cell part span rotating stall.

11.6. Interaction of acoustic resonance and rotating stall

Acoustic resonance and rotating stall are phenomena existing in the TFD compressor in certain areas of the compressor performance map. From their physical origin they are different phenomena only linked to each other by the flow condition they need for their establishment. Now the question is if there is a direct link between them and if the acoustic resonance affects the rotating stall. To put it in other words:

- Is the stall triggered by the acoustic resonance in a point of the performance map where the compressor would remain stable without acoustic resonance?

- Or does the acoustic resonance stabilise the compressor so that the stability limit is shifted to lower mass flows by the acoustic resonance?

- Or has the acoustic resonance no or just a weak effect on the inception of rotating stall?

The fact that neither dihedral blades nor an air injection shift the stability limit in the compressor at rotor speeds where the acoustic resonance exists is a strong argument for an interaction of acoustic resonance and rotating stall. The pressure fluctuations of the acoustic resonance are comparatively high. The pressure waves of the acoustic resonance travel against the mean flow in axial direction and with the mean flow in circumferential direction. Thus they are running across the mean flow. As a consequence, the high pressure regions of the acoustic field behind the rotor might cause an additional incidence on the highly loaded blades, because the flow tries to avoid the high pressure regions. Due to the oscillation of the acoustic pressure field, this extra incidence occurs just for a short moment in time. In the next moment, the high pressure region is followed by low pressure regions and the mean flow is stabilized and the incidence decreases. If the inertia of the mean flow is too high, the stall inception is not significantly affected by the high frequency oscillations of the acoustic resonance. However, if the effect is significant, the short moment where the extra incidence occurs might cause the boundary layer separation that leads to the rotating stall.

It is also possible that instead of the alteration of the incidence, the stabilisation of the boundary layers is the dominant effect of the acoustic resonance on the aerodynamic stability of the compressor. It is known from the literature (Ahuja (1984), Zaman (1992), Hsiao et al. (1994), and Li (2004)) that sound waves have a positive effect on the vertical (perpendicular to the wall) energy transport in the boundary layer and therefore may suppress flow separations. This has been tested mainly for airfoils but Li (2004) found a positive effect on the compressor stability in a low speed axial compressor as well.

A final answer to the open questions formulated here will not be given within this work because the coupling of the effects is too complex to be integrated in a simple model. In view of this, an analytic or numerical solution would be a topic for a project of its own. The measurements also deliver no conclusive answer to the questions. Nevertheless, a few results of the data analysis will be discussed in this section to promote the matter as far as possible.

11.6.1. Time series analysis of measurements

To compare the circumferential velocity of the spinning mode with the rotor speed, the pressure signal of the sensor d13 (between first stator and second rotor) was low-pass filtered and re-sampled synchronous with the rotor. The filtering eliminates the BPF.

Fig. 50 shows the processed signal from a time window of the last second before the stall occurs as a contour plot. Within this time window, the throttle was closed from 89% to 89.9%.

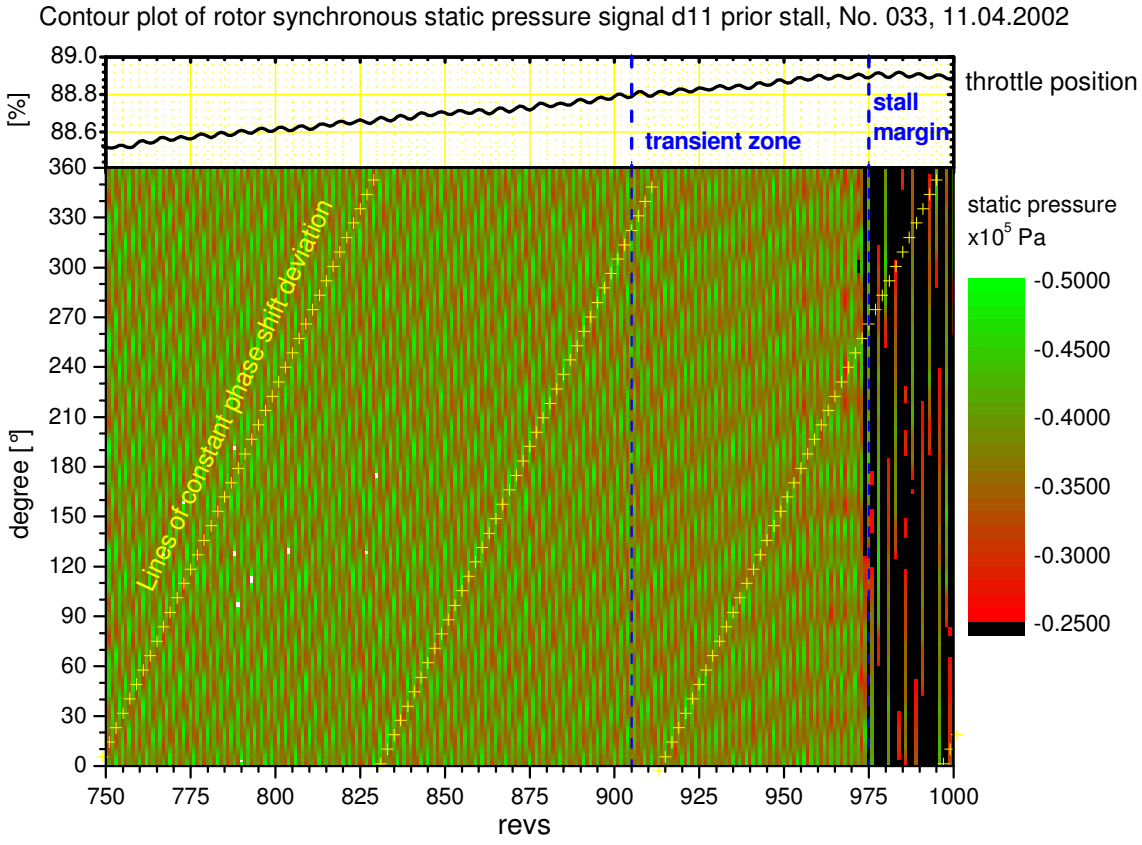

FIG. 50 CONTOUR PLOT OF STATIC PRESSURE SIGNAL PRIOR STALL

Each column in the plot represents one revolution. The red areas are indicating high pressure, the green areas low pressure. The inclined lines in the left part show that here the AR has a non rotor-synchronous circumferential phase velocity. But closer to the stability limit, which is indicated by the dark line on the right side, the slope of the lines representing the AR are turning toward a horizontal line which is a quasi rotor-synchronous phase velocity. This is done by a shift in frequency of the acoustic resonance. In the example in Fig. 50, the fundamental frequency of the acoustic resonance is increasing towards a value of 5.5 times the rotor speed. At this frequency, the high pressure areas occurs every second revolution at the same position. The second harmonic of the acoustic resonance has a frequency of 11 times the rotor

speed. Its high pressure areas occur during each revolution at the same position. At a rotor speed of 1.0, the situation is similar. Here the compressor stalls when the frequency of the fundamental modes is 5.33 times the rotor speed. These results have been repeated in several measurements. So, it seems that the acoustic resonance is triggering the stall when its frequency is hitting an integer fraction of an integer multiple of the rotor speed, presupposing its amplitude is high enough and the mean blade loading is high, too.

On the other hand, it is also possible that the growing boundary layers are causing a reduction in mass flow and so the axial Mach numbers in the compressor are decreasing just before the stall occurs. Then the decreasing Mach numbers are causing the increasing frequency of the acoustic resonance and the acoustic resonance is affected by the stall inception but not the other way round. In this case, the frequency of the acoustic resonance accidentally becomes an integer fraction of the rotor speed.

11.6.2. Modulation of acoustic resonance

Another argument for the interaction of acoustic resonance and rotating stall is the modulation of the amplitudes of the acoustic resonance and the stall pre-cursor modal wave. In subsection 11.4.2 it was shown that prior to stall a modal wave type pressure fluctuation occurs at approximately 0.27 times the rotor speed. This modal wave occurs only in the speed range where the acoustic resonance is excited as well.

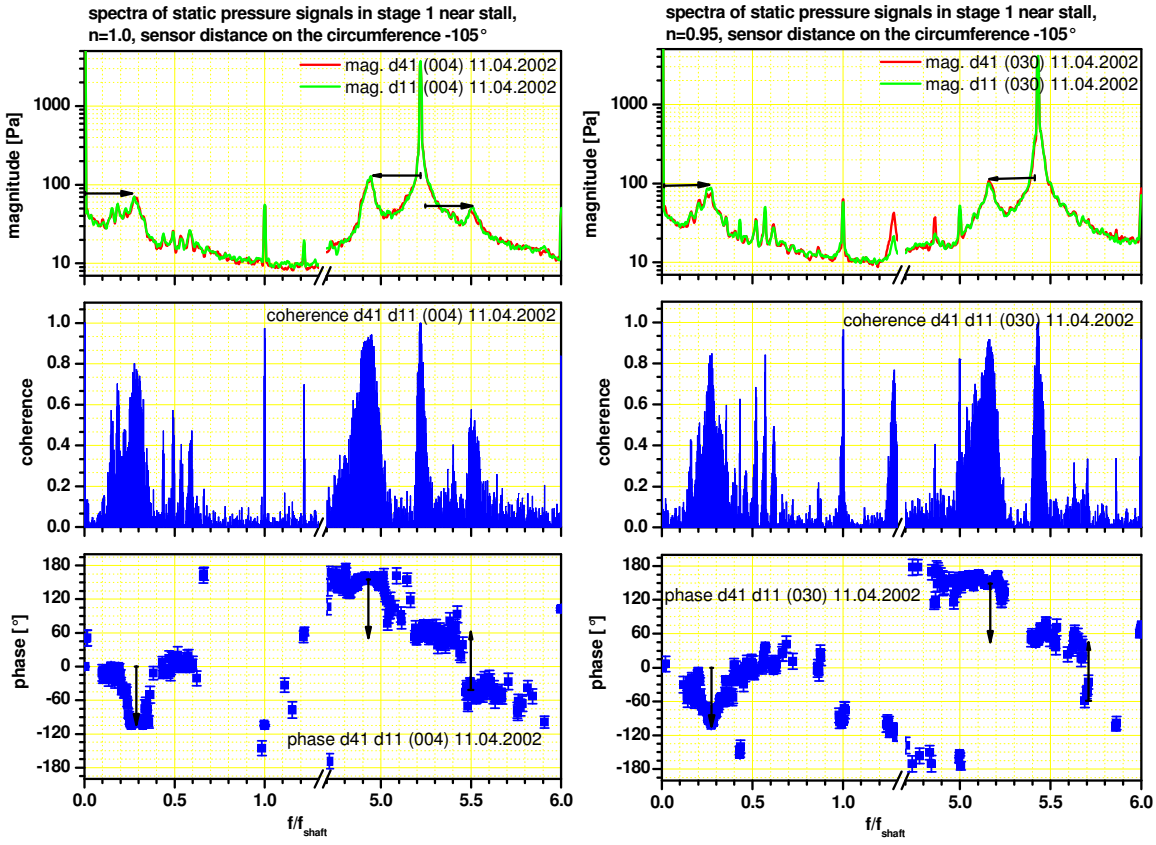

FIG. 51 MODULATION OF AR WITH MODAL WAVE

In Fig. 51, the spectra shown in Fig. 46 on page 84 are extended to the frequency range of the fundamental mode of the acoustic resonance between five and six times of the rotor speed. The small peaks left and right to the peak of the acoustic resonance are in a distance to this main peak that is equivalent to the frequency of the modal wave of 0.27 times the rotor speed. The phase shift around the circumference of these side frequencies is also shifted to the phase of the acoustic resonance by 105°. This is the phase shift of the modal wave around the circumference between the two measuring positions. Such a pattern in a frequency spectrum with side peaks is caused by a modulation of the amplitude of the central frequency with a harmonic function that has a frequency equal to the distance in frequency of the central peak to the side peaks.

In a similar way the BPF is modulated by the acoustic resonance (see Section 8). Such a modulation can be caused by a modulation of the driving force of the acoustic resonance or by a modulation of the axial flow velocity, because the amplitude depends on the axial wave number and the axial wave number depends on the axial flow velocity. So here it seems to be that the modal wave is affecting the acoustic resonance and not vice versa.

Surprisingly, the frequencies of the acoustic resonance at both rotor speeds shown in Fig. 51 are a multiple of the frequency of the modal wave. At a speed of 0.95 it is 20 times the frequency of the modal wave and at a speed of 1.00 it is 19 times the frequency of the modal wave. This suggests that the acoustic resonance is causing the modal wave.

11.6.3. Magnitude and incidence angle of acoustic waves prior stall

The main parameters of the acoustic resonance will be examined with focus on the stall inception now. One is the magnitude of the oscillation because the higher the magnitude the higher incidence it might cause. The other is the incidence angle of the acoustic pressure waves to the rotor rows.

From Section 8 we know that the acoustic resonance is increasing in frequency and amplitude when the circumferential Mach number increases. However, as shown in the lower diagram of Fig. 52, in the last 50 revolutions before the compressor stalls, the magnitudes are slightly decreasing. During these 50 revolutions the throttle was closed, slowly but continuously. Still, the situation is similar when the throttle is kept in its position. In the upper diagram, the magnitudes are shown for one of the rare measurements where the compressor remained stable for more than 2s after the throttle had been closed to a position where the compressor stalls. Again the magnitudes of the acoustic resonance remain on a constant level and drop slightly before the compressor stalls. For this reason, an increase of the pressure magnitude over a certain threshold could be excluded as a trigger for the rotating stall. Another argument is the amplitude of the AR in stage two and three. Here the amplitudes are

significantly higher than in the first stage, although it turned out that the stall starts in all stages nearly at the same time. If the pressure amplitude would be the key parameter, the compressor must stall in the rear stages first.

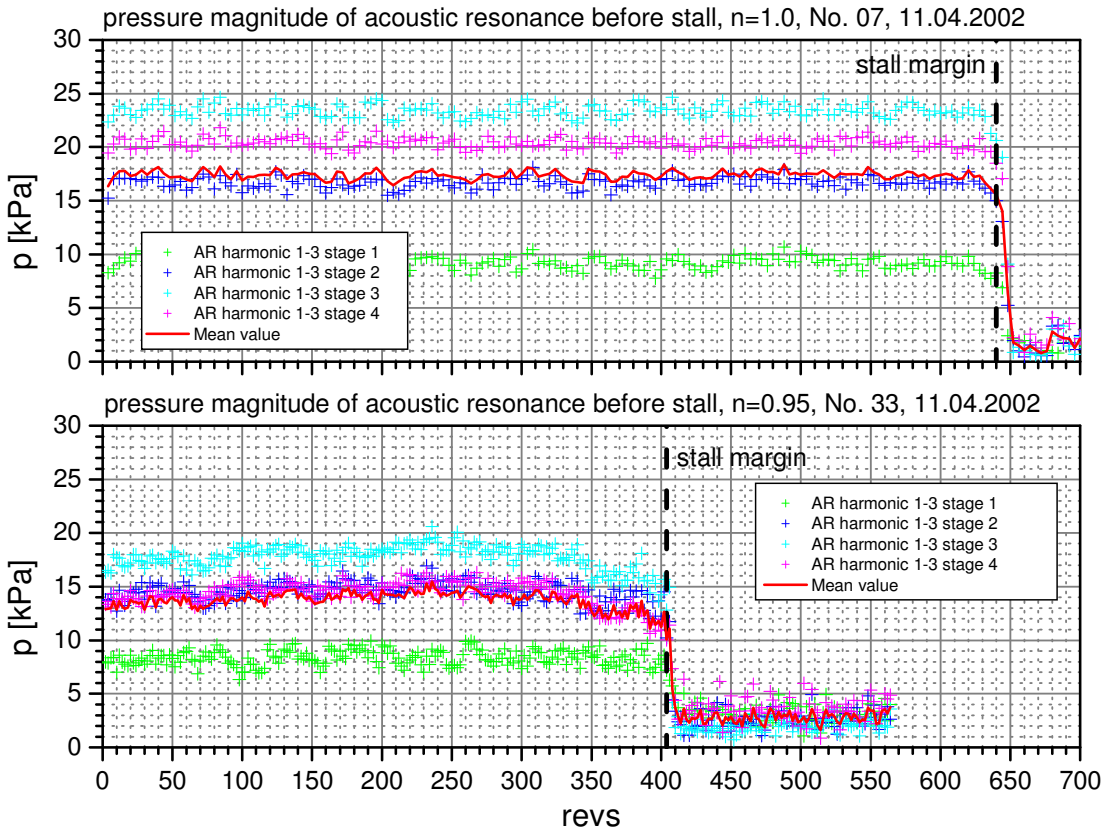

FIG. 52 AMPLITUDES OF ACOUSTIC RESONANCE BEFORE STALL

Unlike the discussion of the incidence angle of the up- and downstream sub-mode in section 10.4, now the focus will be on the measured incidence angle of the interfering field to the rotor. Corresponding to the mass flow through the compressor, the axial flow velocity decreases. The circumferential Mach number remains on its level or even increases at the same time. This causes a decreasing flow angle behind the rotor rows α as shown in Fig. 53. The angle is measured with the dynamic four-hole probe at mid span behind rotor 1 for a normalized rotor speed of 0.95. At the same time, the axial wave length of the acoustic resonance increases while the circumferential wave length remains constant. Also this causes a decreasing incidence angle δ of the acoustic wave to the blade rows. The angles α and δ are defined by the sketch in Fig. 53. If both angles have the same value, the wave fronts are running perpendicular to the mean flow. From the plot of the difference between α and δ shown as a green line in Fig. 53, the difference is approx.13°. So, both angles are close together which means that the direction of propagation of the wave fronts is nearly perpendicular to the mean flow. While frequency and amplitude of the acoustic resonance are increasing, the incidence angle of the acoustic resonance remains more or less constant relative to the mean flow angle. Hence, there is no extra incidence caused by the acoustic resonance due to a change of the incidence angle of the acoustic resonance.

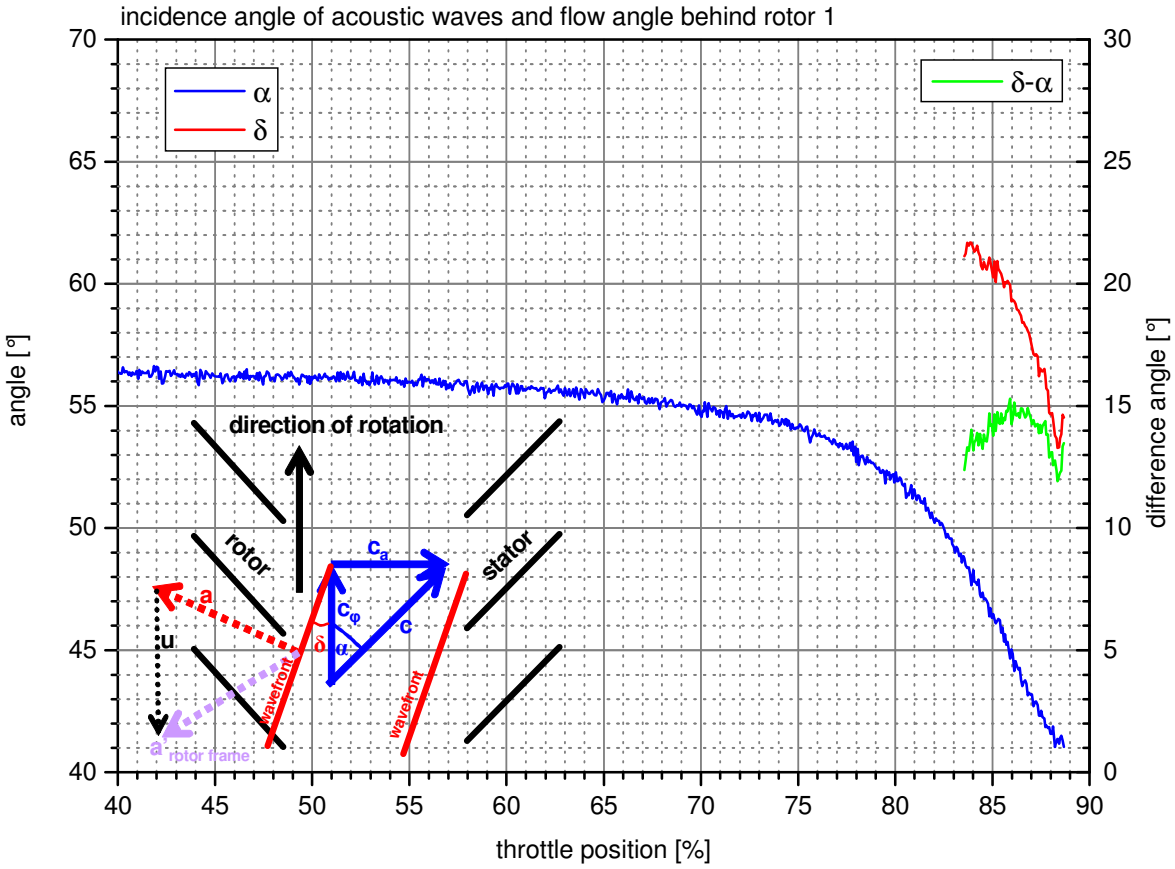

FIG. 53 FLOW ANGLE AND INCIDENCE ANGLE OF ACOUSTIC RESONANCE

11.7. Conclusions of acoustic resonance and rotating stall interaction

In conclusion, based on that the measurements performed so far, an interaction of acoustic resonance and rotating stall could be demonstrated but it is not clear if the oncoming rotating stall reacts to the acoustic resonance or vice versa. The modal waves found as rotating stall pre-cursors are probably linked to the acoustic resonance because they only occur if the compressor is running under resonant conditions. The frequency of the acoustic resonance prior to stall is also a multiple of that of the modal wave.

Improved measurements with an array of pressure sensors in the compressor casing above the rotors would be useful here to examine the development from acoustic resonance to rotating stall in the rotor rows. As things are now, it is still possible that the acoustic resonance has a positive impact on the boundary layers so that the compressor is more stable with acoustic resonance than without.

12. Summary and Conclusions

An acoustic resonance in an axial four-stage high-speed compressor has been explained with a simplified model for helical acoustic modes. It has been shown that for this concrete case, mode scattering, vortex waves, and mode trapping within the blade pitch did not need to be considered. The accordingly simplified mathematical model considers the flow field behind the rotor rows and in the stator as rigid body. The swirl is considered for the calculation of cut-off conditions and axial wave numbers of the acoustic modes. Based on measurements of the resonance frequency, Mach number of the mean flow, and the axial and circumferential phase shift of the pressure signal during resonance, it is shown that the acoustic resonance is an axial standing wave of a spinning acoustic mode with three periods around the circumference of the compressor. The standing wave is formed by two sub modes. One is propagating with the mean flow in axial direction and one propagates against it. Both sub modes are propagating with the swirl in axial direction. The modes propagating against the swirl are cut-off behind the rotor rows where the circumferential flow velocity is high. Due to the reflection of the acoustic waves in front of the rotor rows and high transmission behind the rotor and in the stator rows, the modes become resonant when the axial wave length of the interference wave fits the axial spacing of the rotor blade rows. The axial wave length depends on the axial Mach number of the mean flow, such that it fits the spacing of blade rows only when the mass flow is low. For the present compressor it was calculated that an extension of the axial spacing of the blade rows by 30% will suppress the acoustic resonance. On the other hand a high rotor speed above 15.500 rpm is needed to satisfy the reflection condition in the rotor rows. Therefore, the acoustic resonance is excited at high rotor speed with comparably low mass flow only. In this area of the operating map the compressor is close to its stability limit and the aerodynamic load is high.

As driving force of the acoustic resonance, the background noise in the compressor caused by shear layers in the flow at off design flow conditions is assumed. No other reasonable driving forces were found although a final proof that the resonance is driven by the background noise can not be provided. Due to the fact that the acoustic resonance occurs during operation under high aerodynamic load, flow instabilities with a similar frequency range, like rotating instabilities or tip clearance noise, might be a driving force of the acoustic resonance as well.

Due to the fact that neither air injection at the rotor tips nor dihedral nor bowed blades could shift the stability limit of the compressor to lower mass flows when it is running under resonant conditions, the influence of the acoustic resonance on the rotating stall inception was investigated. For this, rotating stall measurements at different rotor speeds were analyzed in the time and frequency domain. It turned out that the stall margin in the performance map of the compressor and the pre-stall behavior of the compressor were highly reproducible. The onset of stall in axial and radial direction started in all stages nearly at the same time. At rotor speeds close to the design speed, the compressor showed a modal wave type stall inception while at low speeds there

was a spike type stall inception. For high rotor speeds of 1.0, 0.95, and 0.8, the rotation frequency of the stall relatively to the rotor speed was the same while it was different at a rotor speed of 0.55. In all cases, the measured stall was a single cell full span rotating stall. For a rotor speed of 1.0 and 0.95, modal waves were detected in the last stable point on the performance map of the compressor. These modal waves behaved like a mild single-cell rotating stall.

Indeed an interaction of acoustic resonance and rotating stall was demonstrated but it is not clear if the oncoming rotating stall reacts to the acoustic resonance or vice versa. The modal waves found as rotating stall precursors are probably linked to the acoustic resonance since they only occur if the compressor is running under resonant condition. Also the frequency of the acoustic resonance prior stall is a multiple of that of the modal wave. Based on the results of this work it is likely that acoustic resonance and rotating stall inception are linked. However, it is not clear if the acoustic resonance is causing an extra incidence which leads to the inception of rotating stall or if the positive impact on the boundary layers due to the acoustic field stabilizes the compressor so that its stability limit is shifted to lower mass flow rates by the acoustic resonance. This important question could be answered by further investigations only. A concept for this is proposed in the following outlook.

13. Outlook

The following questions are left open in this work:

What is the driving force of the acoustic resonance?

How could the exact values of transmission and reflections coefficients of the blade rows be calculated, so that it could be integrated in an analytical model for the prediction of acoustic resonances at design time?

How is the interaction of acoustic resonance and rotating stall working in detail?

To answer these questions further measurements and simulations are necessary. The measurements could be divided in measurements with improved instrumentation on the existing compressor and measurement with a modified compressor. Ideally the modification should not change the aerodynamic properties of the compressor and suppress the acoustic resonance.

An improvement in instrumentation would be an array of dynamic pressure transducers with at least six equally spaced sensors around the circumference in each stage. A configuration with equally spaced sensors allows the application of common modal analysis methods and spatial Fourier transformation. To fulfil the Shannon theorem the number of sensors has to be twice the number of the highest circumferential mode that should be observed. In axial direction, a pressure transducer in front and above each blade row is necessary for a better localization of the reflection zone in the compressor. A fully equipped axial sensor row is only necessary in one circumferential position. As to this, there are nine sensors needed per stage. The four-hole pneumatic probe should be enabled for higher fluid temperatures allowing for measurements also in the rear stages. So far, static flow measurements at design speed in a single point on the operation map were used for the analysis. These measurements should be extended to for example one or two more rotor speeds (0.9 and 1.0). At each rotor speed and under resonant conditions, two measurements at different mass flow rates would be useful. In addition a measurement of the mean flow in the operating point where the resonance starts is necessary to estimate the limiting incidence angle of the acoustic waves to the blade rows for resonance conditions.

To improve the quality of transient measurements, the implementation of a control circuit would be useful to keep the mass flow rate constant, for example while rotor speed and pressure ratio are varying. In the actual measuring procedure a certain operating point is adjusted and the measurements are triggered manually when steady conditions are reached. This procedure is necessary to achieve data with a high precision to find even small effects of treatments on the efficiency or pressure ratio of the compressor for example. For transient measurements a continuously measurement of at least the mass flow is necessary even if this is linked to a loss in precision. Better the flow angle of the mean flow in each stage is recorded, too.

Even if it has been shown that the acoustic resonance arises inside the compressor the role of the ring throttle should be examined, too. A test that was not done so far is the change of the operating point without moving the throttle. There is a gate valve in the piping system behind the ring throttle, but it is too dangerous to throttle the compressor with this valve. The plenum between the valve and the compressor outlet is too large and a surge in the compressor is possible. But there is also a gate valve in the inlet of the compressor to reduce the pressure at the compressor inlet. This is necessary to run the compressor in the present configuration with the limited drive capacity of the engine. So it might be possible to change the operating point of the compressor without changing the position of the ring throttle by increasing the inlet pressure with the gate valve in the intake piping system of the compressor without venturing a surge. It also should be proved, if a microphone array in the compressor inlet for the application of beamforming methods could be useful to show the acoustic field at the compressor inlet.

The measurement of reflection and transmission coefficients of the blade rows inside the compressor is difficult. A measurement with plane waves in a linear cascade wind tunnel might be an alternative. It also should be evaluated, if a separate test rig with plane waves, zero mean flow and variable stagger angle of the blades could be used to measure the coefficients without mean flow. With the models of Koch, Kaji, and Okazaki, it should be possible to calculate the coefficients for conditions of non-zero mean-flow. Beside the application of this analytical model to experimental data, it should be proven whether the coefficients might be calculated directly with a 3D numerical acoustic solver. If the problem can be treated numerical by a 3D acoustic solver, the mean flow in the whole compressor could be modelled by a CFD calculation and the results can be used as input data for the 3D numerical acoustic solver.
It should also be proved if the more sophisticated mathematical models used by Peake and co-workers, Duan and McIver, Atassi et al., Rienstra and Ovenden could be applied to the present compressor.

All improvements mentioned so far have the aim to verify the results of this work and to achieve more detailed information about the reflection and transmission process in the compressor. To answer the most important question how the acoustic resonance is affecting the performance and stability of the compressor, a modification of the compressor must be found that has preferably no impact on the aerodynamic behaviour of the compressor but suppresses the acoustic resonance.

In a similar problem in a wind blower (Von Heesen (1997)), the problem was solved with the extension of some stator blades in axial direction to suppress the spinning of the modes in the axial gap between rotor and stator row. It is worth to try this in the present compressor, too, because the effort to do this is comparatively low. To minimize the aerodynamic effect of such extended stator blades, only a few blades per row must be extended. In doing so, the extra mechanical excitation of the rotor blades when they pass the extended stator blades should be considered. The main argument against this treatment is the fact that the acoustic resonance is not suppressed by current stator rows because it was shown that, at least for downstream modes, the wave fronts are perpendicular to the stator blades and so they are propagating parallel to the stator

blades. Due to the results of this work, the treatment will come off best when the stator blades are extended at the leading edge towards the upstream rotor row. An extension of the rotor blades at the trailing edge would do the same job but it is more complicated in the realisation by reason of rebalancing the rotor.

From the results of this work the measure with the best prospects would be the extension of the axial gaps so that the distance of the rotors is increased by 30% to 0.26m. Because the compressor used to be a six stage compressor in a former configuration, such an extension might be possible without losing a stage.
If this modification is successful, the aerodynamic behavior of both configurations could be compared and the question whether the acoustic resonance is affecting the stability and performance of the compressor may be answered directly.

14. Acknowledgement

I would like to thank Prof. Dr.-Ing. Jörg R. Seume, my dissertation advisor, for his support throughout the research period. He taught me as physicist with patience and kindness how compressors are working and played a key role in the development of this work.

I would like to thank Prof. Dr.-Ing. Wolfgang Neise of the DLR (Deutsches Zentrum für Luft- und Raumfahrt) in Berlin for his efforts as reviewer and member of the examination board together with Prof. Seume and the chairman Prof. Dr.-Ing. Peter Nyhuis from the Leibniz University of Hannover.

I would also like to thank Prof. Dr.-Ing. Dieter Stegemann, my former advisor at the Institute of Nuclear Technology and Non-destructive Testing at the University of Hannover (IKPH) for his helpful suggestions and support in the beginning of this dissertation procedure.

Thanks to Dr.-Ing. Joachim Runkel, the former senior engineer of the Institute of Turbomachinery and Fluid Dynamics, who suggested me for the job there and also thanks to Dipl.-Ing. Roman Pietrasch, his successor.

Many thanks to all my colleagues at the Institute of Turbomachinery and Fluid Dynamics, especially to the workshop staff and to Dr.-Ing. Axel Fischer, who operated the compressor and supported me in the experimental work. Dr.-Ing. Michael Braun I would like to thank for the steady flow measurements that are an essential part of this work.

For his technical expertise in the area of acoustic transmission through blade rows I would like to thank Dr. Werner Koch from the DLR in Göttingen.

A special thank to my friend and companion Dr.-Ing. Jürgen Fiedler who backed me up at the Kerntech GmbH when I was preparing this work. At this point I would also like to thank the whole staff of the Kerntech Company for their support and backup.

Many thanks to the staff of the Costa Linda Hotel on Isla Margaritha for the peaceful place I needed to finish this work and for the delicious breakfast they prepared every morning.

With all my heart I would like to thank Dr. Bettina Wilts who loved me even without the doctoral level just as I am.

And finally I would like to thank my parents who allowed and supported me to attend the university even if they had preferred me to become a farmer as all my forefathers.

Bernd Hellmich, Hannover, Dec. 2007

15. References

/1/ Ahuja, K. K., Burrin, R.H., 1984, “Control of flow separation by sound”, AIAA paper (84-2298), Williamsburg, Virginia, USA, Oct. 15-17

/2/ Atassi, H.M., Ali A.A., Atassi, O.V., Vinogradov, I.V., 2004, “Scattering of incident disturbances by an annular cascade in a swirling flow” Journal of Fluid Mech., Vol. **499**, pp.111-138

/3/ Bae, J., Breuer, K. S., 2004, “Periodic unsteadiness of compressor tip clearance vortex”, ASME Turbo Expo 2004, GT2004-53015, Vienna, Austria

/4/ Baumgartner, M., Kameier, F., Hourmouziadis, J., 1995, “Non-Engine Order Blade Vibration in a High Pressure Compressor”, ISABE, 12th International Symposium on Airbreathing Engines, Melbourne, Australia

/5/ Bendat, J. S., Piersol, A. G., 2000, “Random Data Analysis and Measurement Procedures”, 3rd Edition, Wiley-Interscience Publication, CIP 99-29982

/6/ Braun, M., Seume, J., 2005, „Experimentelle Untersuchung einer vorwärtsgepfeilten Beschaufelung in einem mehrstufigen Axialverdichter“, FVV (Forschungsvereinigung Verbrennungskraftmaschinen e.V., Frankfurt), Abschlussbericht, Heft **800**, Frankfurt, Germany

/7/ Braun M., Seume, J., 2006, “Forward sweep in a four-stage high-speed axial compressor”, ASME Turbo Expo 2006, GT2006-90218, Barcelona, Spain

/8/ Braun M., Riess, W., 2003, “Stationäres und instationäres Verhalten verschiedener Typen von Strömungs-Messsonden in instationärer Strömung”, Abschlussbericht DFG-Normalverfahren Ri 375/13-1, Hannover, Germany

/9/ Camp, T. R., 1999, “A study of acoustic resonance in a low-speed multistage compressor”, Journal of Turbomachinery, Transactions of the ASME, **121,** pp. 36-43

/10/ Cooper, A. J., Peake, N., 2000, “Trapped acoustic modes in aero-engine intakes with swirling flow”, Journal of Fluid Mech. **419**, pp. 151-175

/11/ Cumpsty, N. A., 1989, “Compressor aerodynamics”, Longman Scientific & Technical, London, pp. 359, UK

/12/ Cumpsty, N. A., Whitehead, D. S., 1971, “The Excitation of acoustic resonances by vortex sheeding”, Journal of Sound and Vibration, **18**, 3, pp.353-369

/13/ Cyrus, V., Rehak, K., Polansky, J., 2005, “Aerodynamic causes of stator vanes damage of the Alstom gas turbine compressor in the gasification combined

cycle using brown coal", OPE – 094_03 / 15, ETC 6, 6th Conference on Turbomachinery, Fluid Dynamics and Thermodynamics, Lille, France

/14/ Duan, Y., McIver, M., 2004, "Rotational acoustic resonances in cylindrical waveguides", Wave Motion, **39**, pp. 261-274

/15/ Evans, D.V., Levitin, M., Vassiliev, D.V., 1994, "Existence theorems for trapped modes", Journal of Fluid Mechanics, Vol. **261**, pp. 21-31, Cambridge, UK

/16/ Fischer, A., 2005, "Numerische und experimentelle Untersuchung von Bow-Statoren in einem hochbelasteten Axialverdichter", Dissertation, Verlag Dr. Hut, München.

/17/ Fischer, A., Reiss, W., Seume, J., 2004, „Performance of strongly bowed stators in a 4-stage high speed compressor", Journal of Technology, Vol. **126**, p. 333-338

/18/ Ghiladi A., 1981, „Drehklangentstehung in axialen Turbomaschinen und Ausbreitung in angeschlossenen Rohrleitungen", Dissertation, RWTH Aachen, Germany

/19/ Gravdahl, J. T., Egeland, O., 1999, "Compressor Surge and Rotating Stall Modeling and Control", Springer Verlag London Limited, 1999

/20/ Heinig, K. E., 1983, "Sound Propagation in Multistage Axial Flow Turbomachines", AIAA Journal **21**, 1, pp. 98-105

/21/ Hellmich B., Braun M.; Fischer A.; Seume, J., 2003, "Observations on the causal relationship between blade count and developing rotating stall in a four stage axial compressor", 5th European Conference on Turbomachinery, Prag, Czech Republic

/22/ Hellmich, B., Seume, J. R., 2004, „Acoustic resonance in a four-stage high-speed axial compressor", ISROMAC10-2004-004, Honolulu US

/23/ Hellmich, B., Seume, J. R., 2006, „Causes of acoustic resonance in a high-speed axial compressor", ASME Turbo Expo 2006, GT2006-90947, Barcelona, Spain

/24/ Horlock, J. H., 1958, "Axial Flow Compressors", Butterworths Scientific Publications, London

/25/ Hsiao, F.-B., Shyu, R.-N., Chang, R. C., 1994, "*High Angle-of-Attack Airfoil Performance Improvement by Internal Acoustic Excitation",* AIAA Journal, Vol. **32**, No.3, March 1994

/26/ Japikse, D., Baines, N. C., 1994, “Introduction to Turbomachinery”, Concepts ETI, Inc. and Oxford University Press

/27/ Kaji, S., Okazaki, T., 1970, “Propagation of sound waves through a blade row: I. Analysis based on semi actuator disk theory”, Journal of Sound and Vibration, **11**,3, pp.339-353

/28/ Kaji, S., Okazaki, T., 1970, “Propagation of sound waves through a blade row: II. Analysis based on the acceleration potential method”, Journal of Sound and Vibration, **11**, 3, pp.355-375

/29/ Kameier, F., 2001, “Experimentelle Untersuchungen Strömungserregter Schaufelschwingungen bei Axialverdichtern”, Abschlussbericht AiF FKZ 1700599, Arbeitskreis Industrielle Forschung, Germany

/30/ Kameier, F., Neise, W., 1997, “Experimental Study of Tip Clearance Losses and Noise in Axial Turbomachines and Their Reduction”, Journal of Turbomachinery, **119**, pp. 460-471

/31/ Kerrebrock, J.L., 1977, “Small Disturbances in Turbo-machine Annuli with Swirl”, AIAA Journal **15**, 6, pp. 794-803

/32/ Kielb, R. E., 2003, “Blade Excitation by aerodynamic instabilities - a compressor blade study”, ASME Turbo Expo 2003, GT2003-38634

/33/ Koch, W., 1971, “On Transmission of Sound Waves through a Blade Row”, Journal of Sound and Vibration, **18**,1, pp. 111-128

/34/ Leinhos, D., Scheidler, C., Step. G., 2002 “Experiments in active stall control of a twin-spool turbofan engine”, ASME Turbo Expo 2002, GT-2003-30002, Amsterdam, Netherlands

/35/ Levy, Y., Pismenny, J., 2005, „High-Frequency Pressure Oscillations of Rotating Stall Type.”, Int. Journal of Turbo and Jet Engines, **22**, pp. 59-87

/36/ Li, Zhi-ping, 2004, “The experiment research on the performance of low speed axial-compressor by external acoustic excitation”, ASME Turbo Expo 2004, GT2004-53183, Vienna, Austria, June 2004

/37/ Lighthill, M. J., 1997, “Collected papers of Sir James Lighthill”, Vol. III, Proceedings of the Royal Society, Oxford Univ. Press, New York, US

/38/ Lohmann D., 1978, „Zur Schallausbreitung in Zylinderkanälen mit helikalen Einbauten“, DFVLR-FB 78-30, Germany

/39/ März, J., Hah, C., Neise, W., 2002, “An experimental and numerical investigation into the mechanisms of rotating instability”, Journal of Turbomachinery, 2002, **124**, p. 367 – 374

/40/ Mailach, R., Lehmann, I., Vogeler K., 2001, “Rotating Instability in an Axial Compressor Originating From the Fluctuating Blade Tip Vortex.” ASME Journal of Turbomachinery, **123**, p. 453 – 460

/41/ Mani, R., Horvay, G., 1970, “Sound transmission through blade rows”, Journal of Sound and Vibration, **12**, 1, pp.59-83

/42/ Methling, F.-O.; Stoff, H., 2002, “Aktive Stabilitätsverbesserung am - Verdichteranalyseverfahren”, Abschlussbericht zum Vorhaben 1.1.5 der Arbeitsgemeinschaft Hochtemperaturgasturbine, Ruhr-Universität Bochum, Germany
http://edok01.tib.uni-hannover.de/edoks/e01fb02/36042368X.pdf

/43/ Niazi, S., 2000, „Numerical Simulation on of rotating stall and surge alleviation in axial compressors“, Ph.D. Thesis, Georgia Institute of Technology, USA

/44/ Ovenden, N. C., Eversman, W., Rienstra, S. W., 2004, „Cut-on cut-off transition in flow ducts: comparing multiple-scales and finite-element solutions”, AIAA Paper 2004 (2945) pp. 1-18

/45/ Pampreen, R. C., 1993, „Compressor Surge and Stall“, Concepts ETI, Inc., Norwich, Vermont, USA

/46/ Parker, R., 1966, “Resonance Effects in Wake Shedding from Parallel Plates: Some experimental observations”, Journal of Sound and Vibration, **4**, 1, pp. 62-72

/47/ Parker, R., 1967, “Resonance Effects in Wake Shedding from Parallel Plates: Calculation of Resonant Frequencies”, Journal of Sound and Vibration, **5**, 2, pp. 330-343

/48/ Parker, R., 1984, “Acoustic resonances and blade vibration in axial flow compressors”, Journal of Sound and Vibration **92**, 4, pp. 529-539

/49/ Parker, R., Stoneman, S.A.T., 1987, “An experimental investigation of the generation and consequences of acoustic waves in an axial-flow compressor: The effect of variations in the axial spacing between blade rows”, Journal of Sound and Vibration, **116**, 3 , pp. 509-525

/**50**/ Parker, R., Stoneman, S. A. T., 1989, „The excitation and consequences of acoustic resonances in enclosed fluid flow around solid bodies”, Proceedings of the Institution of Mechanical Engineers, **203**

/51/ Reissner, A., Seume, J., 2004, “Untersuchung der Systemaspekte stabilitätsverbessernder Maßnahmen in Gasturbinen – grundlegende Untersuchungen“, Abschlussbericht zum Vorhaben 4.3.7C der Arbeitsgemeinschaft Turbo II, http://edok01.tib.uni-hannover.de/edoks/e01fb05/502318155.pdf

/52/ Rienstra, S.W., 1999, “Sound transmission in slowly varying circular and annular lined ducts with flow”, Journal of Fluid Mech. **380,** pp. 279-296

/53/ Rieß, W., Braun, M., 2003, „Stationäres und instationäres Verhalten verschiedener Typen von Strömungs-Messsonden in instationärer Strömung“, Abschlußbericht zum Vorhaben Ri 375/13-1, Deutsche Forschungsgemeinschaft, Hannover

/54/ Rizk, W., Seymour, D.F., 1964, “Investigations into the failure of gas circulators and circuit components at Hinkley Point Nuclear Power Station”, Proc. Institution of Mech. Eng. **179**, 1 No 21, pp. 627-703

/55/ Siewert, C., 2007, “Results of numerical and experimental modal analysis of IGV blades”, internal correspondence, Institut für Dynamik und Schwingungen, Leibniz Universität Hannover

/56/ Sunder, K. L., Hathaway, M. D., Thorp, S. A., Strazisar, A. J., Bright, M. B., 2001, “Compressor stability enhancement using discrete tip injection”, ASME Journal of Turbomachinery, **123**, pp. 14-23

/57/ Tam, C.K.W., 1971, “Transmission of spinning acoustic modes in a slightly non-uniform duct”, Journal of Sound and Vibration, **18**, 3, pp. 339-351

/58/ Tyler, J. M., Sofrin, T. G., 1962, “Axial Flow Compressor Noise Studies”, SAE 1962 pp.309-332

/59/ Ulbricht, I., 2001, „Stabilität des stehenden Ringgitters“, Dissertation, TU Berlin, http://edocs.tu-berlin.de/diss/2001/ulbricht_iris.pdf

/60/ Vignau-Tuquet, F., Girardeau, D., 2005, “Aerodynamic rotating vortex instability in a multi-stage axial compressor”, 17th ISABE, Munich, Germany

/61/ Von Heesen, W., 1997, „Experimentelle Untersuchungen nicht-drehklangbezogener tonaler und breitbandig-rauschartiger Störgeräusche bei Radial- und Axialventilatoren“, Abschlußbericht zum Forschungsvorhaben AiF 10047, Arbeitskreis Industrielle Forschung, Germany

/62/ Walkenhorst, J., Riess, W., 2000, “Experimentelle Untersuchung von Wandkonurierung in einem vierstufigen Axialverdichter”, Abschlußbericht zum Vorhaben 1.121 der Arbeitsgemeinschaft Hochtemperatur Gasturbine, Germany http://edok01.tib.uni-hannover.de/edoks/e001/313061823.pdf

/63/ Weidenfeller J., Lawerenz M., 2002, “Time resolved measurements in an annular compressor cascade with high aerodynamic loading”, ASME Turbo Expo 2002, GT2002-30439, Amsterdam, The Netherlands

/64/ Zaman, K. B. M. Q., 1992, “Effect of Acoustic Excitation on Stalled Flows over an Airfoil”, AIAA Journal, Vol. **30**, No. 6, June 1992, NASA Lewis Research Center, Ohio, US

/65/ Ziada, S., Oengören, A., Vogel, A., 2002, „Acoustic resonance in the inlet scroll of a turbo-compressor”, Journal of Fluids and Structures **16**, 3, pp. 361-373

Lebenslauf

Name, Vorname: Hellmich, Bernd
Geburtsdatum /-ort: 23.11.1970 in Rahden/Westfalen, Deutschland

Schulausbildung

1975 - 1979	Grundschule Rahden
1981 - 1987	Freiherr v. Stein Realschule Rahden
1987 - 1990	Söderblom Gymnasium Espelkamp Abschluß: Abitur

Akademische Ausbildung

1991 - 1997	Physikstudium an der Universität Hannover Abschluß: Diplom

Praktika

1993 - 1994	Dreimonatiges Praktikum bei der Bundesanstalt für Geowissenschaften und Rohstoffe

Berufstätigkeit

1997 - 2000	Mitarbeiter am Institut für Kerntechnik und zerstörungsfreie Prüfverfahren der Universität Hannover, Wissenschaftlicher Mitarbeiter
2000 - 2004	Mitarbeiter am Institut für Strömungsmaschinen der Universität Hannover (heute Institut für Turbomaschinen und Fluiddynamik der Leibniz Universität Hannover), Wissenschaftlicher Mitarbeiter
seit 2000	Miteigentümer und freier Mitarbeiter der Kerntechnik und Anlagendiagnostik Hannover GmbH (heute Kerntech GmbH)

ERRATA Hannover, 6th of march 2017

Supplements and corrections in my dissertation:
„ACOUSTIC RESONANCE IN A HIGH-SPEED AXIAL COMPRESSOR“
Leibniz Universität Hannover 2008

I want to thank all people who gave me hints and I want to apologize for any mistakes in my references, especially to Mr. Niazi.

p. 1 – 3: Missing markers for citations taken from Niazi, S., 2000, „Numerical Simulation of rotating stall and surge alleviation in axial compressors“, Ph.D. Thesis, Georgia Institute of Technology, USA

Correct:
“In 1853 the basic fundamentals of the operations of a multistage axial compressor were first presented to the French Academy of Sciences. Parsons built and patented the first axial flow compressor in 1901 (Horlock (1958)). Since then, compressors have significantly evolved. For example, continuous improvements have enabled increases in efficiency, the pressure ratio per stage, and a decrease in weight. Compressors have a wide variety of applications. They are a primary component in turbojet engines used in aerospace propulsion, in industrial gas turbines that generate power, and in processors in the chemical industry to pressurize gas or fluids. The size ranges from a few centimetres in turbochargers to several meters in diameter in heavy-duty industrial gas turbines. In turbomachinery applications, safe and efficient operation of the compression system is imperative. To ensure this and to prevent damage, flow instabilities must be avoided or dealt with soon after their inception. Considerable interest exists in the jet propulsion community in understanding and controlling flow instabilities.” (Niazi (2000)) …

“The basic purpose of a compressor is to increase the total pressure of the working fluid using shaft work. Depending on their type, compressors increase the pressure in different ways. They can be divided into four general groups: rotary, reciprocating, centrifugal and axial. In reciprocating compressors, shaft work is used to reduce the volume of gas and increase the gas pressure.” (Niazi (2000)) …
“In axial and centrifugal compressors, also known as turbo-compressors, the fluid is first accelerated through moving blades. In the next step, the high kinetic energy of the fluid is converted into pressure by decelerating the gas in stator blade passages or in a diffuser. In centrifugal compressors, the flow leaves the compressor in a direction perpendicular to the rotation axis. In axial compressors, flow enters and leaves the compressor in the axial direction. Because an axial compressor does not benefit from the increase in radius that occurs in a centrifugal compressor, the pressure rise obtained from a single axial stage is lower. However, compared to centrifugal compressors, axial compressors can handle a higher mass flow rate for the same frontal area. This is one of the reasons why axial compressors have been used more in aircraft jet engines, where the frontal area plays an important role. Another advantage of axial compressors is that multistaging is much easier and does not need the complex return channels required in multiple centrifugal stages. A variety of turbo-machines and positive displacement machines as well as their ranges of utilization in terms of basic non-dimensional parameters are shown in Fig. 2. The horizontal axis represents the flow coefficient, which is a non-dimensional volume flow rate. The

vertical axis shows the head coefficient, which is a dimensionless measure of the total enthalpy change through the stage, and roughly equals the work input per unit mass flow." (Niazi (2000))

… "The working fluid passes through these blades without any significant change in radius. Energy is transferred to the fluid by changing its swirl, or tangential velocity, through the stage. A schematic diagram of the changes in velocity and fluid properties through an axial compressor stage is shown in the lower diagram of Fig. 1 taken from references Gravdahl (1999) and Japikse and Baines (1994). It shows how pressure rises through the rotor and stator passages.
Early axial compressors had entirely subsonic flow. Since modern applications require compression systems with higher pressure ratios and mass flow rates, designers have permitted supersonic flow, particularly near the leading edge tip where the highest total velocity occurs. Today, most high performance compression stages are transonic, where regions of subsonic and supersonic flow both exist in the blade passages. The steady state performance of a compressor is usually described by a plot of the mass flow rate versus the total pressure ratio. This plot is called the characteristic or performance map of the compressor." (Niazi (2000))…

p 17: Missing markers for citations taken from Bendat, J. S., Piersol, A. G., 2000, "Random Data Analysis and Measurement Procedures", 3rd Edition, Wiley-Interscience Publication, CIP 99-29982

Correct:
…"A system has constant parameters if all fundamental properties of the system are invariant with respect to time. A system is linear if the response characteristics are additive and homogeneous." Bendat and Piersol (2000)…

p. 74 – 76: Missing markers for citations taken from Niazi, S., 2000, „Numerical Simulation of rotating stall and surge alleviation in axial compressors", Ph.D. Thesis, Georgia Institute of Technology, USA

Correct:
"During the normal operation of a compressor, the airflow through the compressor is essentially steady and axisymmetric in a rotating coordinate system. If a flow instability is somehow introduced into the system (say, due to a change in the rotor speed, flow separation at the inlet, or other type of flow distortion), instabilities may develop and the compressor performance may deteriorate. The instability manifests itself as either a rotating stall or surge. Rotating stall is inherently a 2-D unsteady local phenomenon in which the flow is no longer uniform in the azimuthal direction. It often takes only a few seconds for rotating stall to build up, [sometimes even less than a second,] and the compressor can operate under rotating stall for several minutes before damage develops." (Niazi (2000)) …
"Rotating stall can occur in both compressible and incompressible flow. It is not known for certain why all blades do not stall at the same time. [Dimensional tolerances are one possible explanation.] In manufacturing and assembly, a few blades could be produced with slightly different profiles or with higher stagger angles [or assembled such that the flow cross-section of the passages varies]." (Niazi (2000)) …
"[In addition to the blockage caused by the stall, this increase in flow angle] causes part of

the oncoming flow to be diverted towards the neighboring blades, thus causing an increase in their angles of attack and leading them to stall. As the blade rotates away from the disturbances, the angle of attack decreases restoring normal flow over that blade. The region of the stalled flow, known as a stall cell, continues moving from blade to blade and propagates around the annulus. In a coordinate system attached to the blades, rotating stall moves in a direction opposite to the blade motion at a fraction of the rotor speed. However, in the inertial coordinate system, the stall region propagates in the same direction as the wheel motion. The reported rotational speed of rotating stall around the annulus of compressor varies from 20 to 75 percent of the rotor speed in the direction of the rotor motion. It has also been reported that the incipient rotating stall cells move faster, [although never faster than rotor speed].” (Niazi (2000))…

“The number of stall cells depends on the compressor at hand; one to nine stalled cells have been reported. Two types of stall associated with the number of stalled cells exist, progressive and abrupt. In progressive stall, a phenomenon involving multiple stalled cells, the pressure ratio after stall reduces gradually. Abrupt stall results in a sudden drop in total-to-total pressure rise, and appears to always involve a single stalled cell. One of the characteristics of pure rotating stall is that the average flow is steady with respect to time, but the flow has a circumferentially non-uniform mass deficit. During rotating stall, the cyclical variation of the pressures on the blades can cause them to fatigue and eventually break. Due to uneven shaft work bearings might be overloaded and shaft vibration increases. The flow temperature may also increase for this reason and reduces blade life.” (Niazi (2000))…

“When rotating stall occurs at a point on the unstalled branch of a speed line, the operating point proceeds to the so-called stalled characteristic. [This characteristic is characterized by a lower pressure ratio at the same mass flow and rotor speed.] Sometimes the deterioration in the performance of an axial compressor with rotating stall is small and may not be easily detected, except as an increase in the compressor noise or by some dynamic pressure or vibration sensors. Recovery from rotating stall is often more difficult than surge, [because the mass flow needed for recovery from stall is higher than the mass flow where the stall occurs]. Rotating stall can also serve as the precursor to the more severe and dangerous surge.” (Niazi (2000))

“Surge is a global 1-D instability that can affect the whole compression system. Surge is characterized by large amplitude limit cycle oscillations in mass flow rate and pressure rise. Even a complete reversal of the flow is possible. The behaviour of surge depends on both, the compressor characteristic and the characteristics of the diffuser. In contrast to rotating stall, the average flow through the compressor is unsteady.” (Niazi (2000))…